PROBABILISTIC DURABILITY ANALYSIS OF CEMENTITIOUS MATERIALS UNDER EXTERNAL SULFATE ATTACK

By

Sohini Sarkar

Dissertation

Submitted to the Faculty of the

Graduate School of Vanderbilt University

in partial fulfillment of the requirements

for the degree of

DOCTOR OF PHILOSOPHY

in

Civil Engineering

August, 2010

Nashville, Tennessee

Approved:

Professor Sankaran Mahadevan

Professor David S. Kosson

Professor Florence Sanchez

Professor Caglar Oskay

Doctor Christine Langton

ACKNOWLEDGEMENTS

This work would not have been possible without help and support of several people. Firstly, I would like to express my gratitude to my advisors Prof. Sankaran Mahadevan and Prof. David S. Kosson for their continual support and advice over the years. I would like to thank my committee members, Prof. Florence Sanchez and Prof. Caglar Oskay, and Dr. Christine Langton (Savannah River National Laboratory), for their inputs and valuable suggestions. I am also grateful to Dr. Hans van der Sloot and Dr. Hans Meeussen (Energy Research Center of the Netherlands) for their help in development of this work. I would also like to thank Dr. Kevin G. Brown, Josh R. Arnold for the excellent discussions. I would also like to acknowledge the helpful discussions and valuable suggestions from Dr. Greg Flach (Savannah River National Laboratory) and Dr. Eric Samson (SIMCO Technologies). Finally, I would like to thank all my friends and family members for their love and years of support.

This dissertation was prepared with the financial support by the U. S. Department of Energy (DOE), under Cooperative Agreement Number DE-FC01-06EW07053 entitled 'The Consortium for Risk Evaluation with Stakeholder Participation III' awarded to Vanderbilt University. This research was also carried out in part as part of the Cementitious Barriers Partnership supported by U.S. DOE Office of Environmental Management. The opinions, findings, conclusions, or recommendations expressed herein are those of mine and do not necessarily represent the views of U.S. DOE or Vanderbilt University.

TABLE OF CONTENTS

PAGE

LIST OF FIGURES

LIST OF TABLES

TABLE PAGE

LIST OF CEMENT CHEMISTRY NOTATIONS

Symbol	Description
A	Al_2O_3
C	CaO
C_3A	Tricalcium aluminate ($3CaO.Al_2O_3$)
C_3AH_6	Hydrogarnet ($3CaO.Al_2O_3.6H_2O$)
$C_4A\bar{S}H_{12}$	Calcium monosulfoaluminate ($4CaO.Al_2O_3.SO_3.12H_2O$)
$C_6A\bar{S}_3H_{32}$	Ettringite ($6CaO.Al_2O_3.3SO_3.32H_2O$)
CH	Calcium hydroxide/Portlandite ($CaO.H_2O$)
CSH	Calcium silicate hydrate ($xCaO.ySiO_2.zH_2O$)
$C\bar{S}H_2$	Gypsum ($CaO.SO_3.2H_2O$)
F	Fe_2O_3
H	H_2O
S	SiO_2 (Chapter II)
$\bar{S}$	SO_3

LIST OF SYMBOLS

Symbol	Description
A' and B'	Temperature dependent parameters
A_r	Concentration factor
$\bar{C}$	Homogenized stiffness tensor (MPa)
C_0	Stiffness tensor of reference phase (MPa) (Chapter III) Initial covariance matrix (MPa) (Chapter V)
C_d	Crack density parameter
C_{dc}	Conduction percolation threshold
C_{dec}	Rigidity percolation threshold
C_r	Stiffness tensor of phase r (MPa)
C_t	Covariance matrix at time t
C_t'	Modified covariance matrix
D	Diffusivity (m^2/s)
D_i^0	Free solution diffusivity of i^{th} ion (m^2/s)
D_p	Additional diffusivity in the percolation regime (m^2/s)
DE_k	Discretization error of mesh k
E	Young's modulus (MPa)
E_0	Initial Young's modulus (MPa)
E_{eff}	Effective Young's modulus (MPa)
$\bar{E}$	Homogenized Young's modulus (MPa)
F_r	Faraday's constant (Coulomb/mol)
$G(\theta, s)$	Numerical model

$H_D(\varphi)$	Change in diffusivity due to change in porosity
I	Ionic strength (mmol/L)
I_k	k dimensional identity matrix
K_{eq}	Equilibrium constant
$L(\theta)$	Likelihood function of θ
R	Universal gas constant (Joule/mol/K)
S	Eshelby's Tensor (Chapter III)
T	Temperature (K)
V	Volume of representative solid volume (m^3)
V_m	Volume of m^{th} solid (m^3)
V_m^{init}	Initial volume of m^{th} solid (m^3)
V_p	Volume of paste (m^3)
ΔV_r	Change in volume (m^3)
V_r	Total volume of the reactants (m^3)
$\Delta \bar{V}_s$	Effective change in solid volume (m^3)
b	Fraction of porosity need to be filled before strain can develop
c_i	Concentration of i^{th} species (mmol/L)
d	Experimental observations
dx	Thickness of cell (m)
d_i	Array of i^{th} parameter
e_0	Electrical charge of one electron (Coulomb)
f_c'	Compressive strength (MPa)
f_{exact}	Exact solution
f_k	Solution with mesh k
f_r	Volume fraction of phase r
f_t'	Peak tensile stress (MPa)
$f(\theta\|d)$	Posterior distribution of θ
$f(\theta)$	Prior distribution
$f(d\|\theta)$	Probability density of d given θ
g_p	p-th order error term coefficient
h_k	Element size of mesh k
k and m	Stress-strain diagram model parameter
k and μ	Bulk and shear moduli (GPa)
$\bar{k}$ and $\bar{\mu}$	Homogenized bulk and shear moduli (GPa)
k_0 and μ_0	Bulk and shear moduli of reference phase (GPa)
n	Number of samples
$q(X)$	Proposal distribution
q_n	n-th stage proposal distribution
$r_{12,23}$	Ratio between element sizes of different mesh
$r_n(x_t, y_1, \ldots y_n)$	n-th stage acceptance probability of y_n, given knowledge of the previous samples x_t,…, y_{n-1}
s	Input parameters
$\bar{s}$	Sample standard deviation
s_d	Scaling parameter
t	Time (s)

$t_{\frac{\alpha}{2},n-1}$	Value from student's t distribution at probability level of $\alpha/2$ for $n-1$ degrees of freedom
w	Post peak deformation (m)
w_0	Deformation corresponding to peak stress (m)
x_0	Initial state
x_t	Current state
$\bar{x}$	Mean
y	Output parameters
	Next sample
z_i	Valence of i^{th} ion
$\mathcal{O}(.)$	Higher order error terms
ε	Uniaxial strain (Chapter II)
	Error (Chapter V)
$\bar{\varepsilon}$	Volumetric strain (Chapter II)
	Macroscopic strain (Chapter III)
ε_0	Permittivity of vacuum (F/m)
ε^0	Externally applied strain
ε_i	Error in i^{th} parameter
ε_k	Permittivity of the medium (F/m)
ε_p	Strain corresponding to peak stress
ε_r	Dielectric constant of water (Chapter II)
	Strain in phase r (Chapter III)
ε^{th}	Threshold strain
$\varepsilon_{21,32}$	Difference in solutions of different mesh sizes
ϵ	Very small positive number
γ	Any positive number less than 1
γ_i	Chemical activity coefficient
$\langle\mu\rangle_{1-\alpha}$	100α % prediction interval
ν	Poisson's ratio
ν_0	Initial Poisson's ratio
ω	Damage parameter
ω_0	Damage parameter corresponding to peak stress
$\pi(X)$	Target distribution
φ	Porosity (m^3/m^3)
φ_0	Initial porosity (m^3/m^3)
σ	Stress (Chapter II) (MPa)
	Standard deviation (Chapter V)
τ	Tortuosity
θ	Model parameter

CHAPTER I

INTRODUCTION

1.1 Goal

The overall goal of this dissertation is to develop a durability and uncertainty assessment framework for cementitious materials exposed to external sulfate solution using probabilistic methods by incorporating various sources of uncertainty. Furthermore, evaluation of sulfate attack on cementitious materials is used to illustrate a general approach to uncertainty analysis when coupling chemical and mechanical processes to evaluate performance of cementitious materials. In this context, contributions of uncertainty from chemical equilibrium, mass transfer and mechanical strength models are considered.

1.2 Overview

Low activity nuclear waste is being disposed by mixing with cementitious materials and then being placed in above ground reinforced concrete vaults which are to be covered with soil and a final cap to achieve a shallow burial scenario for final disposition. One example of this practice is the disposal of “saltstone” at the Department of Energy Savannah River Site near Aiken, SC [1]. A significant amount of sulfate ions (approximately 24000 mg/L [2]) initially are present in the pore solution of the solidified waste form that can potentially leach out of the waste and diffuse into the concrete vault walls. The resulting reaction of sulfate ions with the concrete solid phases, and

subsequent and cracking of the concrete has been identified as one of the potentially important degradation processes for these concrete vaults [3]. Cementitious materials under external sulfate attack expand in volume due to the formation of expansive products, e.g. ettringite [4, 5] and gypsum [6, 7], leading to cracking and lose strength due to calcium leaching and decalcification of the main cement hydration product (i.e. calcium silicate hydrate) [8]. If the structure is cracked, the radioactive materials in the waste form then may migrate (by diffusion or percolation) through the cracks and be transported to the soil or the groundwater. Thus it is important to assess the durability of such structures subjected to aggressive conditions so that (1) engineered systems can be designed to minimize long-term degradation of contaminant retention structures, and (2) contaminant release rates and extents do not exceed acceptable levels.

1.2.1 Numerical model development

When sulfate ions diffuse through a cementitious structure, they react with cement hydration products. Several mineral phases dissolve or precipitate to maintain the equilibrium condition of the pore solution. Some ions (e.g., calcium) also start leaching out of the structure resulting in changes in porosity. As some or all of the pores within the cement are filled with expansive solid phases, precipitated due to the reactions between sulfate ions and the cement hydration products, strain develops which leads to stress and cracking. This in turn accelerates further diffusion of the ions. The mineralogical composition of the microstructure changes with time because of formation and dissolution of several mineral phases, with these chemical changes leading to changes in strength of the specimen. Ettringite and gypsum form as sulfate ions react with the

cement hydration products, while calcium hydroxide and calcium silicate hydrate dissolve to replenish the concentration of calcium ions in the pore solution which eventually leach out of the structure. These phenomena affect the strength of the structure in addition to cracking. Thus the essential components in the degradation of cementitious materials due to the ingress of sulfate and leaching of primary material constituents are diffusion of ions, chemical reaction, structural damage due to cracking, and change of strength due to chemical reactions. Some numerical models available in the literature simulate diffusion using detailed partial differential equations and include a detailed chemical reaction model, but do not include structural damage accumulation [9]. Some models include a continuum damage mechanics based approach to assess the damage of the structure, but do not include detailed diffusion and chemical reaction models [10, 11]. A few numerical models simulate the effects of calcium leaching [12-15]. Very few models are available for simulating the combined effect of calcium leaching and sulfate attack [16]. Among the models available in the literature, some models do not include structural damage due to cracking [9, 17] and/or strength loss due to calcium leaching [6, 9-11, 17-19]. Some models assume that calcium and sulfur are the only two species that diffuse in and out of the structure [10, 11, 16] whereas exchange of various ions between the pore solution and the external environment may also affect the strength of the structure. Furthermore, most models do not explicitly consider the impact of pH and multi-constituent chemical composition of the external solution, as well as the multi-constituent evolution of pH and pore solution composition within the material. Thus it is important to incorporate all the essential components of the degradation mechanism into

a single model framework to accurately simulate the behavior of the structures under sulfate attack.

The most common measure of sulfate resistance of cementitious materials is length change of the specimen [20]. Many researchers have attributed the change in length to the amount of ettringite formation [10, 11, 21-23]. But there may not be any direct relationship between the amount of ettringite formed and the bulk expansion of the specimen [24] as assumed by the previous researchers. Also, the structure fails due to cracking and loss of strength, which may not have any direct relationship to the bulk expansion of the specimen. Thus it is essential to evaluate the mineralogical features of the specimen with time, as well as damage of the specimen due to precipitation/dissolution of the solids.

In this dissertation, a numerical modeling framework is developed to evaluate behavior of the structure as a function of time integrating all the essential components of the degradation process of cementitious materials under external sulfate attack – (1) diffusion of ions, (2) chemical reactions of diffused species with the cement hydration products, (3) structural damage accumulation due to cracking, and (4) change in strength of the structure due to mineralogical changes as a result of chemical reactions. The model uses LeachXS/ORCHESTRA [25] for modeling coupled mass transfer, chemical reactions, and processes that result in change in material strength and cracking, and MATLAB [26] for evaluating changes in strength of the structure due to cracking and chemical reactions. The model is calibrated and validated using experimental results available from the literature. The usefulness of the model to evaluate structural damage progression and mineralogical evolution is also demonstrated.

1.2.2 Identification of influential parameters

Most experimental studies in the literature regarding degradation of cementitious materials under sulfate attack consist of immersing specimens in a sulfate solution under a controlled or uncontrolled environment [27-30]. Variations of some of the environmental conditions affect the response of the structure more than the others. Evaluation of the effects of these factors is important in order to understand the implications of these changes in field conditions. Some experimental studies are available in the literature that evaluate the effects of external and internal factors on the degradation of cementitious materials [27, 30-32]. But very few studies are available that evaluate the effects of these factors using a numerical model [33] that includes robust representation of chemical and physical processes with being both cost and time effective. The numerical model developed in this research is used to study the sensitivity of the damage process to the changes in the environmental conditions and material properties e.g., pH of the external solution, external solution concentration, cement type, porosity or tortuosity of the material. The results are then used to interpret the implications of such changes under field conditions.

1.2.3 Calibration of chemical equilibrium model

One of the most important parts of the probabilistic durability assessment of cementitious materials under chemical attack (e.g., sulfate attack in this dissertation) is uncertainty quantification for the chemical equilibrium speciation, which has not received significant attention in the literature. However, a considerable amount of research has been done on the propagation of uncertainty in the chemical equilibrium models in

geochemistry and geophysics [34, 35]; but the inverse problem (i.e. uncertainty quantification) has not been performed in the past. Numerical simulation of chemical degradation of cementitious materials exposed to an aggressive environment has also been a focus of research interest for a long time [16, 36-40] as mentioned before. The most challenging parts in this regard, are - (1) determining the cement hydration products present in a hardened structure, and (2) selecting potential chemical reactions that may take place when the structure is exposed to aggressive environment. Several numerical models are available in the literature for simulating cement hydration [41-44] that provide useful information on the type of solid phases likely to be present in a matured structure. Some numerical models developed for simulating concrete degradation consider a limited set of chemical reactions that can possibly take place under chemical attack [10, 16, 22]. Very few numerical models include flexible platforms that incorporate thermodynamic information for simulating chemical reactions [9, 45]. The thermodynamic data required for chemical equilibrium modeling is generally obtained from the literature without consideration of the laboratory conditions under which these values are determined and the human error. It is also important to acknowledge the fact that the mineral phases are most likely present as an assemblage rather than pure phases which further introduces uncertainty in the structural response. Variability in the material parameters and experimental errors also add to the overall uncertainty in the model response. Thus treating equilibrium constants deterministically may not represent the system behavior appropriately. Also, various approximations and assumptions during the modeling process contribute to the uncertainty in the model prediction. Therefore, a numerical framework is developed in this research for calibrating the equilibrium constants of a

geochemical speciation model for cementitious materials under uncertainty in the material properties and experimental conditions. The uncertainty quantification in the equilibrium constants are performed using the Bayesian statistical method in conjunction with adaptive Markov Chain Monte Carlo simulation techniques.

1.2.4 Probabilistic durability analysis

The assessment period for the low activity nuclear waste containment structures is generally 10,000 years [46] and is therefore dependent on the long-term durability of such structures. It is not feasible to perform experiments to evaluate performance of these structures at this time scale. Thus the mechanistic model developed in this research can be useful in assessing the durability of these structures. If long term structural response is of interest, it is important to consider the uncertainty due to variability of the system parameters and the fluctuations in the initial and the boundary conditions over time. Several service life assessment models available in the literature include variability of the parameters [47-50], but assess resistance to degradation using empirical relations. In addition to physical variability of the parameters, data uncertainty due to sparse or interval data, and model uncertainty due to various assumptions and approximations, introduce additional uncertainty in the model predictions. Thus a probabilistic framework is developed in this dissertation to assess the durability of such structures under the combined effects of sulfate attack and calcium leaching, incorporating various sources of uncertainty. Finally, the framework is applied on a one dimensional representation of a concrete structure to evaluate the time to complete damage under sulfate attack by

separating and then combining various sources of uncertainty in different parts of the model.

Water saturation is assumed as a conservative simplifying assumption for all cases in this dissertation. Actual field conditions typically are unsaturated which result in slower diffusion and degradation processes than predicted for saturated conditions.

1.3 Research Objectives

The specific objectives of this research are:

1. Develop a numerical methodology for assessing degradation of cementitious materials under external sulfate attack by integrating various stages of the degradation process – diffusion of ions, chemical reactions, and structural damage due to cracking.
2. Extend the model developed in objective 1 to assess the change in strength of the cementitious materials exposed to aggressive environment due to changes in the mineralogical compositions as a result of chemical reactions.
3. Perform sensitivity analysis to study the effects of the changes in the environmental conditions and material properties on the damage progression and interpret the implications of such changes under field conditions.
4. Develop a methodology for quantifying uncertainty in the chemical equilibrium model using experimental results of the leaching behavior of the cementitious materials.
5. Develop a framework for durability assessment of cementitious materials exposed to aggressive environment using probabilistic methods incorporating various sources of

uncertainty and evaluate the effects of uncertainty in different parts of the model on the durability of the structure.

1.3 Dissertation Organization

The dissertation is organized as follows:

Chapter II provides a detailed description of the numerical modeling framework developed for assessing degradation of cementitious materials under external sulfate attack by integrating various stages of the degradation process – diffusion of ions, chemical reactions and structural damage due to cracking. The model is calibrated and validated using experimental results obtained from the literature. The usefulness of the model in evaluating the mineralogical evolution and mechanical deterioration of the structure with time is demonstrated.

Chapter III extends the model described in Chapter II by incorporating a continuum micromechanics based approach for assessing changes in the elastic properties and the strength of the structure due to chemical reactions. Two homogenization schemes combined with Eshelby's equivalent inclusion method are used to estimate the mechanical properties of the structure that change with time due to dissolution and precipitation of the solids. The extended model is then calibrated and validated for (1) calcium leaching only, and (2) combined calcium leaching and external sulfate attack using experimental results obtained from the literature.

Sensitivity analysis is performed in Chapter IV using the numerical model to evaluate the effects of several external and internal factors (e.g., pH and concentration of the

external solution, and porosity and tortuosity of the material) on the degradation of the structure.

Chapter V gives detailed description of a numerical framework for assessing uncertainty in the chemical equilibrium module used in the durability assessment framework using a Bayesian statistical method combined with adaptive Markov Chain Monte Carlo simulation techniques. The method is demonstrated for an example case obtained from a database/expert decision support system.

The ultimate objective of this dissertation is development of a methodology for computing the probability of reaching a particular degradation measure as a function of time. Various approaches for statistical representation of the uncertainties – (1) physical variability due to inherent randomness of physical processes and material parameters, (2) data uncertainty due to sparse or interval data, and (3) model uncertainty due to assumptions and approximations in modeling a physical process are discussed in chapter VI. The methodology for assessing the durability of the structure is implemented using nested and single-loop Monte Carlo Simulation techniques. Different sources of uncertainty in the particular numerical model developed in this dissertation are identified. The effects of these uncertainties on the durability assessment of the structure are also demonstrated in this chapter.

Finally, the dissertation is concluded in Chapter VII by summarizing the contributions of this research and recommending possible future work.

CHAPTER II

NUMERICAL SIMULATION OF CEMENTITIOUS MATERIALS DEGRADATION UNDER EXTERNAL SULFATE ATTACK

2.1 Introduction

Cementitious materials exposed to sulfate rich environment degrade with time due to formation of expansive products leading to cracking and eventually to the failure of the structure. The degradation mechanism due to sulfate ingress through the structure is discussed in this chapter. The numerical approaches developed in the literature for simulating degradation along with their shortcomings are also described. A new methodology is proposed in this chapter by incorporating all the essential components of the degradation mechanism. The numerical model is calibrated and validated using experimental data available from the literature. The usefulness of the model in simulating the damage propagation through the structure is also demonstrated.

2.2 Mechanism of Sulfate Attack

The main components of Portland cement are tricalcium and dicalcium silicates, tricalcium aluminate and tetracalcium aluminoferrite. The cement components react with water and externally added gypsum to form several cement hydration products. In cement chemistry notation, these components are represented as C: $CaO, S: SiO_2, A: Al_2O_3, \bar{S}: SO_3, H: H_2O, F: Fe_2O_3$ etc. [51]. If the hydration is not complete, some of the cement components remain unreacted. Some of the main hydration

products are calcium silicate hydrate (CSH), calcium hydroxide or Portlandite (CH), ettringite ($C_6A\bar{S}_3H_{32}$), calcium monosulfoaluminate ($C_4A\bar{S}H_{12}$), hydrogarnet (C_3AH_6), etc. When sulfate ions penetrate a cement-based structure, a series of reactions take place as shown in Eqs. (1) - (7). The sequential process of reactions is shown in Figure 2.1. Sulfate ions react with Portlandite to form gypsum and some calcium aluminate phases to form ettringite (as shown by the light arrows in Fig. 2.1). Then gypsum reacts with calcium aluminate phases (as shown in the box in Fig. 2.1), if present, to form ettringite (as shown by bold arrows in Fig. 2.1). Initially the calcium ions are supplied by Portlandite. When Portlandite is not available, calcium silicate hydrate dissociates into calcium hydroxide (as shown by the dashed arrow in Fig. 2.1) and silica gel, supplying calcium ions for ettringite formation [24]. This dissolution process is controlled by chemical equilibria between the solid phases and pore solution and solution conditions controlling calcium saturation in pore solution.

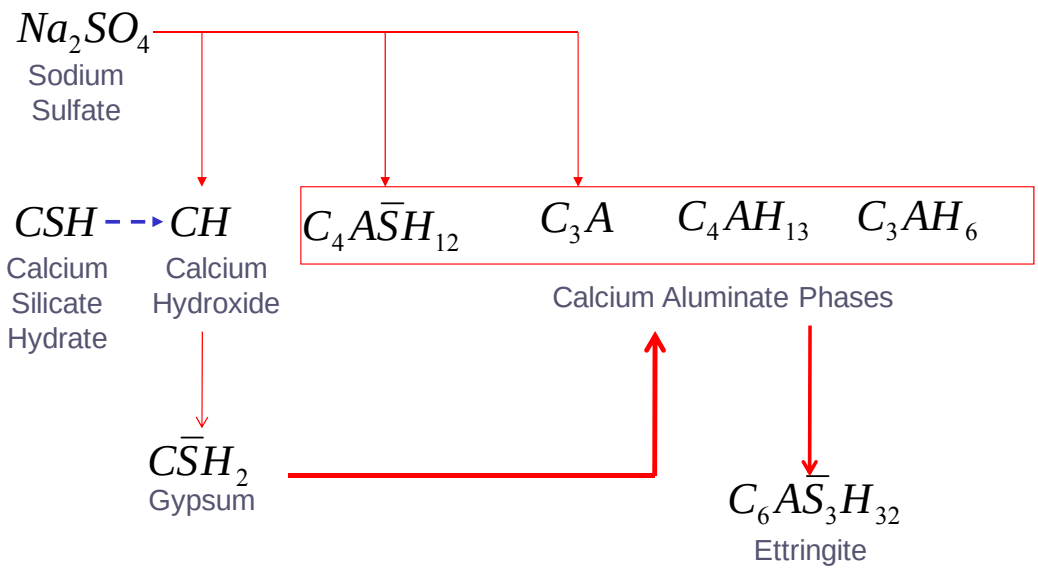

Figure 2.1 : Schematic diagram of the chemical reactions due to sulfate ingression.

The main expansive products formed as a result of the reactions are ettringite and gypsum. The changes in volume (ΔV_r) as a consequence of the chemical reactions with respect to the original volume of the reactants (V_r) are given in Table 2.1. Reactions involved in sulfate attack assuming the source of sulfate ions to be sodium sulfate are as follows [3, 10]:

- Portlandite

$$Na_2SO_4 + CH + 2H \rightarrow C\bar{S}H_2 + 2NaOH \quad (1)$$

- Monosulfate

$$C_4A\bar{S}H_{12} + 2C\bar{S}H_2 + 16H \rightarrow C_6A\bar{S}_3H_{32} \quad (2)$$

$$3C_4A\bar{S}H_{12} + 3Na_2SO_4 \rightarrow 6NaOH + 2Al(OH)_3 + 21H + 2C_6A\bar{S}H_{32} \quad (3)$$

- Tricalcium aluminate

$$C_3A + 3C\bar{S}H_2 + 26H \rightarrow C_6A\bar{S}_3H_{32} \quad (4)$$

$$C_3A + 3Na_2SO_4 + 3CH + 32H \rightarrow 6NaOH + C_6A\bar{S}H_{32} \quad (5)$$

- Tetracalcium aluminate hydrate

$$C_4AH_{13} + 3C\bar{S}H_2 + 14H \rightarrow C_6A\bar{S}_3H_{32} + CH \quad (6)$$

- Hydrogarnet

$$C_3AH_6 + 3C\bar{S}H_2 + 20H \rightarrow C_6A\bar{S}_3H_{32} \quad (7)$$

The change in volume due to the chemical reactions is obtained by subtracting the total volume of the products from the total volume of the reactants. The change in volume leads to volumetric strain if the volume of the products is greater than the volume of the reactants (as shown in Table 2.1). The strain developed exerts pressure on the surrounding cement matrix. The structure starts cracking when the strain exceeds the

strength of the material. Also, the calcium silicate hydrate dissociation into calcium hydroxide and silica gel results in loss of strength because silica gel is not adhesive. Thus, the net effects of sulfate attack are expansion, cracking and strength loss.

Table 2.1 : Relative volume change in reactions involved in sulfate attack.

Reaction	**Relative volume change ($\frac{\Delta V_r}{V_r}$)**
Eq. (1)	1.24 [3]
Eq. (2)	0.55 [3]
Eq. (3)	0.52 [3]
Eq. (4)	1.31 [3]
Eq. (5)	2.83 [3]
Eq. (6)	0.48 [10]
Eq. (7)	0.92 [3]

Several hypotheses have been proposed in the past to explain the mechanism of expansion [24, 52]. Two prominent hypotheses are – (i) crystal growth pressure hypothesis, where it is proposed that the expansion is caused by the growth of large ettringite crystals at the cement-aggregate interfaces and cracks; and, (ii) homogeneous paste expansion hypothesis where it is proposed that the expansion is caused by the growth of small ettringite crystals throughout the paste [53, 54]. But neither of the hypotheses is unanimously agreed upon. The model developed in this research is based on simplifying assumptions required for computational homogenization. It is assumed

that the cement hydration products are homogeneously distributed throughout the structure. When sulfate ions diffuse through the structure (Figure 2.2a), they react with the cement hydration products. The reaction products are also distributed homogeneously throughout the cement matrix. If the volume of the products is more than the volume of the reactants, the extra volume can only be accommodated in the pore space. The shaded area in Figure 2.2b shows the deposited solid product in pore space. The solid product grows in volume as the reaction progresses. When it touches the pore wall, it starts exerting pressure which leads to stress in the material. If the stress is more than the strength of the material, cracks start to form. The solid product does not need to fill up the total pore volume in order to start exerting pressure due to the difference in shape of the deposited solid and the pore as shown in Figure 2.2c. Thus it is assumed that a fraction of the pore volume is available for solid product deposition before strain develops and cracking starts.

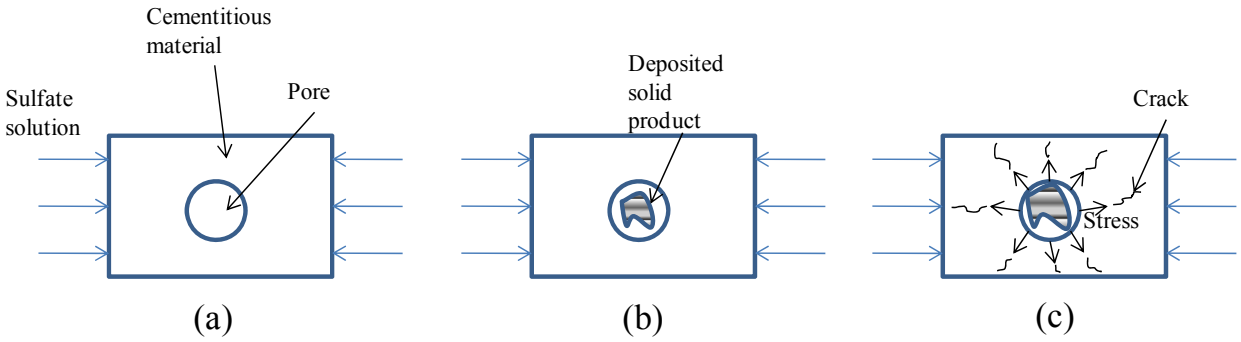

Figure 2.2 : Strain and crack development mechanism.

2.3 Numerical Modeling of Sulfate Attack

Different models have been developed in the past to numerically simulate the phenomenon of sulfate attack. One of the earliest models was developed by Atkinson and Hearne [21]. This model was based on an empirical relation between volumetric expansion of the structure and the total amount of ettringite formed, developed using experimental results. Following Atkinson and Hearne, Clifton and Pommersheim [3] developed a model from the assumption that volume change in the reaction gives rise to paste expansion which is linearly dependent on the amount of ettringite formed.

A simple micromechanical model developed by Krajcinovic *et al.* [11], was based on homogenization of microscopic responses on a macroscale for evaluation of the macro response of the structure. This model was refined recently by Basista and Weglewski [22]. Tixier and Mobasher [10, 33] developed a model similar to that developed by Clifton and Pommersheim with a different analytical expression assumed for expansion. The model included a continuum damage mechanics approach to evaluate structural damage and modified the diffusivity assuming that it increases linearly with increasing damage. Bary [16] developed another numerical model incorporating structural damage due to cracking; but only calcium and sulfate concentrations were considered to be the dominant species in the model.

Saetta *et al.* [18] developed a general framework for evaluation of mechanical behavior under physical/chemical attacks. This model evaluated the coupled effects of moisture, heat and chemical species. Evaluation of expansion and cracking due to chemical attack was not included in the model. Another general framework was developed by Schmidt-Dohl and Rostasy [19] which was based on thermodynamic and

kinetic considerations for evaluation of degradation of structures under chemical attack. This model can only be used for chemical reactions with known kinetic rates. Also, it is assumed in this model that cause of expansion and cracking of the structure is caused by ettringite formation only. Another general framework was developed by Shazali *et al.* [6] to evaluate degradation of concrete under sulfate attack but in relation to gypsum formation only. Damage was quantified by a chemical damage parameter (similar to Saetta *et al.*) and was incorporated to evaluate strength of the specimen.

Samson, Marchand and associates [9, 55-57] developed a numerical model for describing the mechanism of ionic transport in unsaturated cement systems. It included ionic diffusion through the use of extended Nernst-Planck equation, moisture transport and chemical reactions. The model also incorporated the effects of micro-structural changes on the transport properties of chemical species in the cementitious materials using empirical relations based on experimental results. But this model did not consider the changes in the mechanical properties due to cracking and consequent effects on the transport (e.g., diffusive) properties. Gospodinov *et al.* [17] developed a model which included diffusion of chemical species into cement and the effects of simplified chemical reactions on the changes in porosity. But this model did not include the effects of cracking on the material parameters.

Ping and Beaudoin [58] developed a theoretical model based on the chemical-thermodynamic principles. It was assumed that the expansion results from conversion of chemical energy in the form of crystallization pressure to mechanical energy which overcomes the cohesion of the system. The theory was qualitatively validated using experimental results; but it was not quantitatively implemented.

From the perspective of this research, Tixier's model and Krajcinovic-Basista's model are particularly important as these models evaluate cracking of the structure under sulfate attack using continuum damage mechanics. The general framework of these models is presented in Figure 2.3.

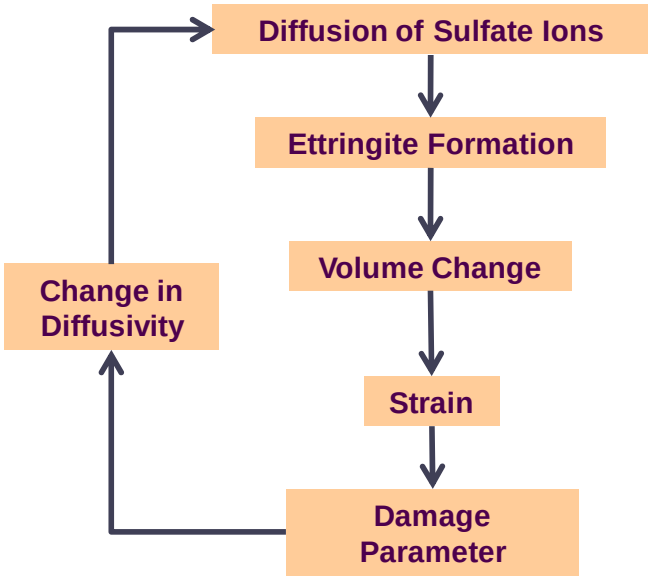

Figure 2.3 : Components of Tixier's and Krajcinovic-Basista's models.

As shown in Figure 2.3, diffusion of only sulfate ions was considered in Tixier's and Krajcinovic-Basista's models. Leaching out of the ions from inside of the structure and diffusion coupled with chemical equilibrium of other ions present in the external solution were not considered. Expansion of the specimen was assumed to occur due to ettringite formation only; gypsum formation, which is also seen to be expansive [6, 7], was not taken into account. Calcium leaching out of the specimen while in contact with water also was not considered in the aforementioned models. This increases the porosity of the

structure [59], hence accommodating more ettringite before strain can develop. Thus, improved diffusion and chemical reaction models are needed to accurately simulate the behavior of the cementitious materials under chemical attack that are robust enough to consider a broader range of cementitious material formulation and composition of solutions at the external boundary (i.e., contacting water composition).

The proposed framework of the model incorporating diffusion of additional species, responses to changes in pore structure and more extensive chemical reactions is shown in Figure 2.4.

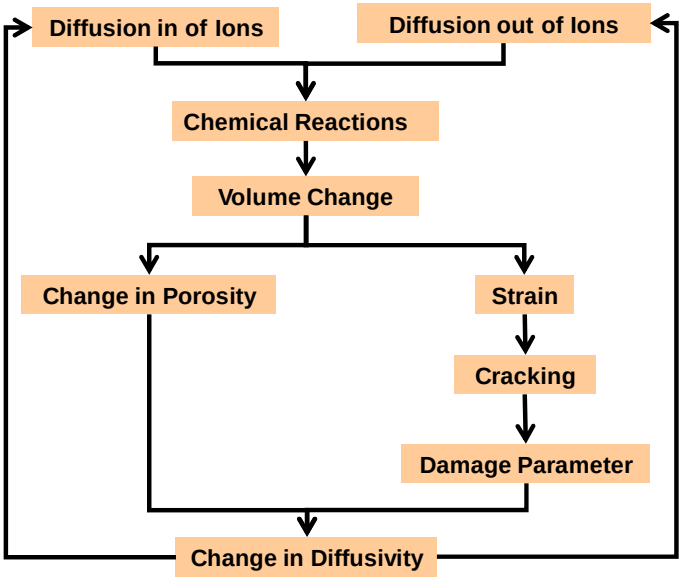

Figure 2.4 : Overview of the framework developed in this research.

In the proposed framework, diffusion of all ions from the external solution and simultaneous leaching out of the ions from inside of the structure are considered. Diffusion and leaching out of ions change the chemical composition of the pore solution which disturbs the local equilibrium and thus leads to chemical reactions. These

processes are assumed to change the porosity of the structure. Volume change of solid phases due to the chemical reactions leads to change in porosity and strain. Strain leads to cracking of the structure which is reflected in the damage parameter. Change in porosity and cracking are assumed to modify the diffusivity which affects further diffusion of the ions. Thus the developed framework integrates the needed parts for more robust assessment of degradation of cementitious materials under sulfate attack in a unified framework. The specific approaches used for each phenomenon are described below.

2.3.1 Diffusion of ions

Diffusion of an ion through a saturated porous material under isothermal condition is modeled by taking into account diffusion of ions under concentration gradient as well as under chemical activity gradient, assuming diffusion under electrical potential is negligible [9, 60, 61]. This is expressed as

$$\frac{\partial(\varphi c_i)}{\partial t} = \mathrm{div}\left(\frac{D_i^0 \varphi}{\tau}(\mathrm{grad}(c_i) + c_i \mathrm{grad}(\ln \gamma_i)\right) \quad (8)$$

where c_i is the concentration of the i^{th} ion, D_i^0 is the free solution diffusivity of the ion, φ is the porosity, τ is the tortuosity and γ_i is the chemical activity coefficient of the ion. The first term on the right hand side is the rate of diffusion due to the concentration gradient. The second term is the rate of diffusion due to the interactions of ions among each other. If there are N ions present in the system e.g. $Ca^{2+}, Na^{+}, SO_4^{2-}, Mg^{2+}$ etc., then N equations are formed for diffusion of all the ions using Eq. (8). These N equations are solved simultaneously in order to obtain diffusion profiles of all the ions. The modified Davies equation [62] is used to calculate the chemical activity of the ions which produces better results for highly concentrated ionic solutions (application range 0-1500

mmol/L) such as concrete pore solutions [63] than other formulations of activity coefficient [64] and is given as

$$\ln \gamma_i = -\frac{Az_i^2\sqrt{I}}{1 + a_i B\sqrt{I}} + \frac{(0.2 - 4.17 \times 10^{-5} I)Az_i^2 I}{\sqrt{1000}} \tag{9}$$

where z_i is the valence of the ion, and I is the ionic strength of the solution expressed as

$$I = \frac{1}{2}\sum_{i=1}^{N} z_i^2 c_i \tag{10}$$

and *A* and *B* are temperature dependent parameters given as

$$A = \frac{\sqrt{2}F_r^2 e_0}{8\pi(\varepsilon_k RT)^{\frac{3}{2}}} \tag{11}$$

$$B = \sqrt{\frac{2F_r^2}{\varepsilon_k RT}} \tag{12}$$

where e_0 is the electrical charge of one electron (1.602×10^{-19} C) and a_i is a parameter dependent on the species (assumed to be 3×10^{-10} m as an average value for all the species [62]), F_r is the Faraday's constant (96488.46 C/mol), R is the universal gas constant (8.3143 J/mol/K), T is the temperature and ε_k is the permittivity of the medium (i.e. water in this case) given as

$$\varepsilon_k = \varepsilon_0 \varepsilon_r \tag{13}$$

where ε_0 is the permittivity of the vacuum (8.854×10^{-12} F/m) and ε_r is the dielectric constant of water (80). The temperature is assumed to be $298\,K$ for the simulations presented in this chapter. However, it is important to verify the ionic strength of the pore solution before application of the Davies equation as pore solution ionic strength may

exceed the equation's application range as can be found in [65]. The appropriate activity coefficient is then applied to each ion in solution based on the actual speciation of individual ionic forms for each element in solution as calculated as part of the Orchestra equilibrium speciation calculations at each node and time step. The activity coefficients are used in Eq. (8) for the calculation of diffusion profiles of the ions and in the chemical equilibrium calculations as discussed in the next subsection.

2.3.2 Chemical reactions

When the ions diffuse through the cementitious material, they react with the cement hydration products. Some solids dissolve or precipitate to maintain the equilibrium state of the pore solution which leads to changes in porosity of the structure. Diffusivity changes due to the changes in porosity as shown in Figure 2.4. The approach adopted for chemical equilibrium calculations, changes in porosity and changes in diffusivity are discussed in this subsection.

Several researchers have used partial differential equations with empirical reaction rate constants combined with Fick's law to simulate diffusion and chemical reactions [6, 10, 11, 16, 36, 66]. Alternatively, some researchers have used an uncoupled approach to model diffusion and chemical reactions [55] which is computationally more efficient than the coupled approaches [9]. An explicit finite difference scheme is applied to solve the diffusion equations. Then, a sequential noniterative approach is used to couple diffusion and chemical reactions where transport equations are solved first followed by chemical equilibrium calculations. Iterations between these two modules are avoided by using a variable time stepping scheme. The criterion for choosing a time step is restricting the

change in mass between two adjacent cells to within 1% of the total quantities of all the ions present in the cells. The minimum of all the time steps calculated using this method is adopted for the next time step.

A built-in chemical reaction module in a geochemical speciation and transport code, ORCHESTRA [25], is used here to calculate the equilibrium phases of the solids formed/dissolved as a result of the chemical reactions within each unit cell. Consider two species *A* and *B* that react to form another species *C*, with the formation reaction as follows :

$$aA + bB \rightarrow cC \tag{14}$$

At equilibrium, the relation among *A*, *B* and *C* can be expressed as [34]

$$(C)^c = K_{eq}(A)^a(B)^b \tag{15}$$

where K_{eq} is the equilibrium constant and $(\ldots)$ is the activity of the corresponding species and is expressed as

$$(A) = \gamma_A c_A \tag{16}$$

where γ_A is the activity coefficient as calculated from Eq. (9) and c_A is the concentration of *A*. If *N* number of species are considered, there will be *N* simultaneous equations which will need to be solved to determine the amount of each species in the system at equilibrium. The resulting system of simultaneous equations along with charge and mass balance equations are solved at each time step. The chemical reaction module used here is flexible which allows any number of ions and mineral phases to be considered in the equilibrium calculations, thus making it an efficient platform for modeling a system as complicated as concrete. The solid phases and their equilibrium constants considered for simulations in this chapter are given in Table 2.2. The equilibrium constant values are

calculated with respect to the primary species Al^{3+}, Ca^{2+}, Fe^{3+}, Mg^{2+}, H_4SiO_4, $Na^+$and SO_4^{2-} using ORCHESTRA database.

Table 2.2 : Equilibrium constants of solid phases.

Chemical formula	Common name	log K
$2CaO.Al_2O_3.SiO_2.8H_2O$	Stratlingite	-49.44 [25]
$2CaO.Fe_2O_3.SiO_2.8H_2O$	Fe-Stratlingite	-42.33 [25]
$3CaO.Al_2O_3.6H_2O$	Hydrogarnet	-79.53 [25]
$3CaO.Al_2O_3.CaSO_4.12H_2O$	Calcium monosulfoaluminate	-74.29 [25]
$3CaO.Fe_2O_3.6H_2O$	Fe-Hydrogarnet	-72.41 [25]
$Mg(OH)_2$	Brucite	-16.84 [25]
$3CaO.Al_2O_3.3CaSO_4.32H_2O$	Ettringite	-56.90 [25]
$3CaO.Fe_2O_3.3CaSO_4.32H_2O$	Fe-Ettringite	-49.78 [25]
$Fe(OH)_3$	Iron hydroxide	-3.00 [25]
$Al(OH)_3$	Gibbsite	-7.76 [25]
$CaSO_4.2H_2O$	Gypsum	4.60 [25]
$Ca(OH)_2$	Portlandite	-22.80 [25]
$NaAlSi_3O_8$	Analbite	-3.51 [25]
$Na_2SO_4.10H_2O$	Mirabilite	1.11 [25]
SiO_2	Silica gel	2.71 [41]
$2CaO.2.4SiO_2.3.2H_2O$	Tobermorite-I	-28.03 [41]
$0.83CaO.SiO_2.1.3H_2O$	Tobermorite-II	-11.17 [41]
$1.67CaO.SiO_2.2.1H_2O$	Jennite	-29.52 [41]

At each time step, material properties change as chemical reactions alter the composition of the structure. Porosity increases or decreases due to the precipitation and dissolution of the solid phases. The change in porosity is calculated as

$$\varphi = \varphi_0 - \frac{\Delta V_s}{V} \tag{17}$$

where φ and φ_0 are the current and the initial porosities respectively, V is the volume of the representative volume element and ΔV_s is the change in solid volume expressed as

$$\Delta V_s = \sum_{m=1}^{M} \left(V_m - V_m^{init} \right) \tag{18}$$

where M is the number of solid phases, V_m^{init} and V_m are the initial and current volume of the m^{th} solid. The change in volume is negative (or positive) if the final volume of solids is less (or more) than the initial volume as a result of dissolution (or precipitation) of solids. The pore volume increases (or decreases) as can be calculated from Eq. (17). Diffusivity increases (or decreases) with increase (or decrease) in pore volume. The change in diffusivity due to the change in porosity is calculated using an empirical equation given as [9]

$$H_D(\varphi) = \frac{e^{\frac{4.3\varphi}{V_p}}}{e^{\frac{4.3\varphi_0}{V_p}}} \tag{19}$$

where V_p is the volume of the paste. Eq. (19) is a correction factor which is multiplied with the diffusivity ($\frac{D_i^0}{\tau}$) in Eq. (8) and is used as the changed diffusivity for the next time step.

The ions present in the pore solution can only react with the species in contact with them through the pore wall. Thus only a fraction of the total amount of the species will be available to the ions in the pore water. The available quantities are obtained from a database/expert decision support system, LeachXS [67]. The database contains results of a large number of experiments performed on a range of cement and mortar compositions. Specimens are crushed to simulate a completely degraded state (95% of the material < 2 mm in size resembling completely cracked specimen) and are allowed to leach while in contact with water under different pH conditions until solid-solution chemical equilibrium is approximated. It is assumed that the maximum leached amount as well as the maximum amount capable of reacting with the pore solution for a particular specimen (i.e. the available quantities) cannot exceed the amount obtained from the experiments.

The LeachXS database in conjunction with ORCHESTRA also provides information regarding the mineral phases most likely to be present in the system and required to produce good agreement between the experimental results and model representation for solution concentration of the set of dissolved species (e.g., OH^-, Ca^{2+}, SO_4^{2-}, etc.) as a function of pH and liquid-to-solid ratio of the extractions.

The chemical reaction module used in this research is flexible, and allows any number of ions and mineral phases to be included in the numerical framework provided the thermodynamic data for the mineral phases are known (i.e. equilibrium constants as in Eq. (15)).

2.3.3 Damage accumulation

The change in solid volume due to the chemical reactions and the leaching is calculated as in Eq. (18) where the volume of each solid is calculated by multiplying number of moles of the solid with its molar volume. The molar volumes of the solids considered in this study are shown in Table 2.3 [41, 68]. The change in solid volume leads to development of strain and cracking which changes the diffusivity of the ions as shown in Figure 2.4. The approach adopted to relate the changes in solid volume to the formation of cracks is described in this subsection.

Table 2.3 : Molar volumes of the mineral phases [41].

Mineral Phase	Molar Volume (cm^3/mol)
$C_6A\bar{S}H_{32}$	707
C_3AH_6	150
C_3FH_6	155
C_2ASH_8	216
C_2FSH_8	227
$C_{1.67}SH_{2.1}$	78
$C_{0.83}SH_{1.3}$	59
CH	33
S (amorphous)	29
$C\bar{S}H_2$	75
$C_4A\bar{S}H_{12}$	309
$Al(OH)_3$ (amorphous)	32
$C_2S_{2.4}H_{3.2}$	59*
$Fe(OH)_3$ (microcrystalline)	34
Na_2SO_4	220

* It is assumed that the molar volume of Tobermorite-I ($C_2S_{2.4}H_{3.2}$) is the same as Tobermorite-II ($C_{0.83}SH_{1.3}$) due to lack of data.

The solid products formed as a result of chemical reactions will precipitate in the capillary pores. It is assumed that a fraction of the pore volume will be filled before strain starts to develop. This accounts for the fact that ettringite (one of the main expansive products formed as a result of sulfate attack) is a needle shaped structure and it can generate stress as soon as its ends touch the pore wall [69] even if the pore is not completely filled. In general, it accounts for the differences in morphologies of the pore and the precipitated solids. It also accounts for the effect of pore size distribution on solid deposition and does not require distinction amongst pore size domains. Essentially this feature is a model parameter which needs to be calibrated using experimental results. A first estimate of this parameter can be obtained by assuming a fraction of the capillary porosity as ions diffuse mainly through capillary pores and diffused ions interact with the

solids surrounding the capillary pores. Let us assume the fraction of porosity to be b. The net solid volume change contributing to strain development is then calculated as

$$\overline{\Delta V_s} = \Delta V_s - b\varphi V \tag{20}$$

Clifton and Pommersheim [3] assumed that expansion and cracking will not start until all of the pore volume is filled up by reaction products which leads to $b = 1$. Tixier and Mobasher [33] estimated the value of b to be between 0.05 to 0.45 by calibrating the model response using experimental results, Basista and Wegnewski [36] assumed it to be 0.5. Denham [70] estimated the maximum porosity loss under different scenarios to be 34% by performing numerical simulations and it was concluded that fracture will only start occurring if the amount of porosity available is $\leq 34\%$. More pore volume is available for solid product deposition if b is greater, leading to delayed initiation of cracking. Similarly, initiation and rate of crack progression is faster if b is smaller.

If $\overline{\Delta V_s} > 0$, volumetric strain can be calculated as

$$\bar{\varepsilon} = \frac{\overline{\Delta V_s}}{V} \tag{21}$$

Otherwise, strain is zero. Assuming that the material is isotropic, uniaxial strain is calculated as

$$\varepsilon = \frac{\bar{\varepsilon}}{3} \tag{22}$$

Cracks start to form once the developed strain exceeds the strength of the material. A continuum damage mechanics based model is used to relate the cracked state of the structure to the strain calculated from Eq. (22). The cracked state of the structure is manifested in a scalar quantity known as damage parameter. Conceptually, the damage parameter used here can be interpreted as the surface density of material defects [18] and it can be expressed as the ratio of the damaged area (area of the crack) to the original area

[18, 71] as shown in Figure 2.5. Several formulations are available in the literature which relates strain/stress to the damage parameter [72-76]. The approach used in this research is described in the following paragraphs.

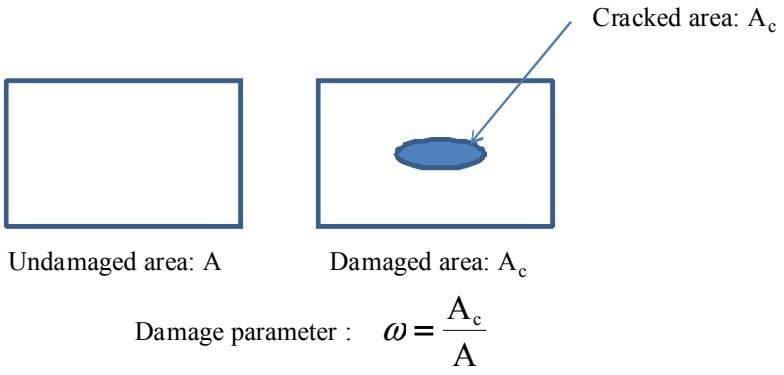

Figure 2.5 : Schematic diagram depicting concept of damage parameter.

A qualitative stress-strain diagram for cementitious materials under tensile stress is shown in Figure 2.6.

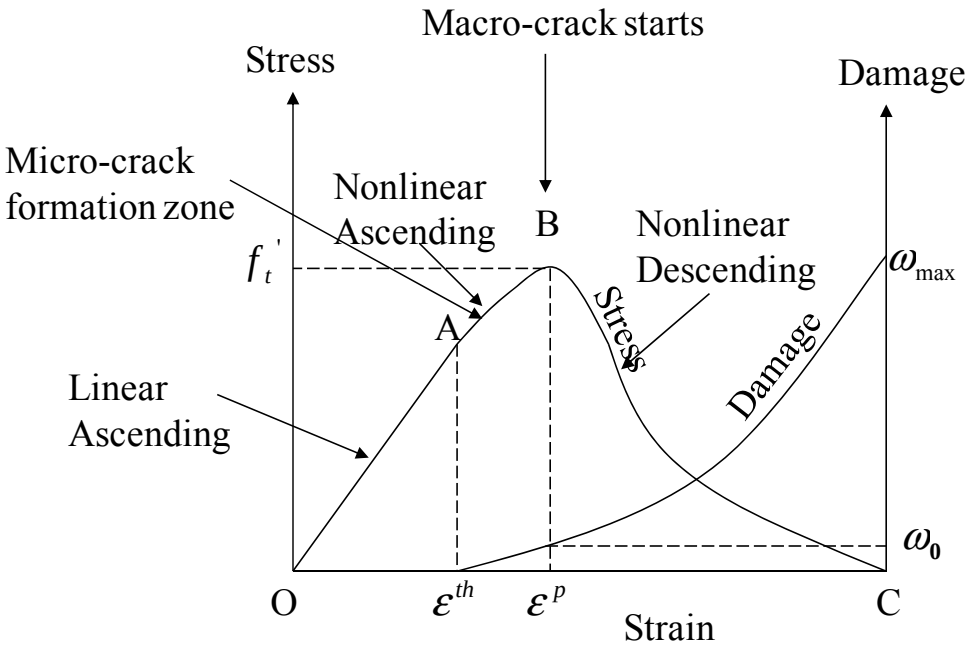

Figure 2.6 : Stress-strain diagram of concrete under tension [6].

Cementitious materials contain pores and micro-cracks which do not affect the strength of the structure in the elastic region (segment OA in Figure 2.6). In the nonlinear ascending region (segment AB in Figure 2.6), new micro-cracks form which finally coalesce at B to form macro-cracks leading the structure to failure defined by the nonlinear descending curve. In the nonlinear ascending region, the damage parameter ω is related to the Poisson's ratio (If a load is applied in the longitudinal direction of a specimen, then the Poisson's ratio can be expressed as $\nu = -\frac{\text{Lateral strain}}{\text{Longitudinal strain}}$) of the damaged structure for a three-dimensional case and the density of the nucleated cracks C_d [71]. C_d combines the information about the number and the size distribution of the cracks per unit volume of the material and can be expressed as [71]

$$C_d = k(1 - \frac{\varepsilon^{th}}{\varepsilon})^m \text{ for } \varepsilon > \varepsilon^{th} \tag{23}$$

where ε is the strain, ε^{th} is the threshold strain at which the micro-cracks start forming, and k and m are model parameters that need to be calibrated from the experimental stress-strain diagram following the procedure given below.

In the nonlinear ascending region of the stress strain diagram, an equivalent Young's modulus (E) can be expressed as

$$E = E_0(1 - \omega) \tag{24}$$

where E_0 is the Young's modulus obtained as the initial tangent or the slope of the linear part of the curve (segment OA in Figure 2.6) and ω is the damage parameter. For the uniaxial case, stress (σ) and strain (ε) in the nonlinear region can be related as

$$\sigma = E_0(1 - \omega)\varepsilon \tag{25}$$

Assuming that the damage parameter is not affected by the Poisson's ratio of the damaged structure for a one-dimensional simulation, ω can be expressed as [71, 77]

$$\omega \approx \frac{16}{9} C_d \tag{26}$$

Combining Eqs. (23), (24), (25) and (26) the following expression can be obtained as

$$\sigma = E_0[1 - \frac{16}{9} k \left(1 - \frac{\varepsilon^{th}}{\varepsilon}\right)^m]\varepsilon \tag{27}$$

From Eq. (27) and the stress strain diagram obtained from the experimental data, k and m can be calibrated using a least squares curve fitting method.

The post-peak stress and deformation of the structure (segment BC in Figure 2.6) are modeled by using the relations proposed by Nemat-Nasser and Hori [10, 78]. based on fracture mechanics and are given as

$$\frac{\sigma}{f_t'} = \sqrt{\frac{\tan\left(\frac{\pi\omega_0}{2}\right)}{\tan(\frac{\pi\omega}{2})}} \tag{28}$$

$$\frac{w}{w_0} = \frac{\sigma}{f_t'} \frac{\log[\sec(\frac{\pi\omega}{2})]}{\log[\sec(\frac{\pi\omega_0}{2})]} - 1 \tag{29}$$

where f_t' is the maximum tensile stress, ω_0 is the damage parameter corresponding to the peak stress, w is the post-peak deformation ($= \left(\varepsilon - \varepsilon_p\right)dx$ where dx is the thickness of the cell) and w_0 is the deformation corresponding to the peak stress ($= \varepsilon_p dx$). A relation between the damage parameter and the deformation of the structure can be obtained by combining Eqs. (28) and (29).

2.3.4 Change in mechanical and diffusion properties due to cracking

Mechanical and diffusion properties change due to the presence of the cracks. In the literature, the effect of the cracks on the material properties has been studied using effective continua or mean field models when the density of the cracks is sparse [79] (referred to as mean field regime). The modified relation between the diffusivity and the crack density parameter in this regime can be expressed as [11, 36]

$$D = \frac{D_i^0}{\tau}(1 + \frac{32}{9}C_d) \tag{30}$$

Similar linear relations between the elastic moduli (Young's modulus and Poisson's ratio) and the damage parameter are also derived as [11, 36]

$$E = E_0(1 - \frac{16}{9}C_d) \tag{31}$$

$$\nu = \nu_0(1 - \frac{16}{9}C_d) \tag{32}$$

where E_0 and ν_0 are the initial Young's modulus and Poisson's ratio. Eqs. (30), (31) and (32) are derived based on a self-consistent method which is not valid once macro-cracks

start forming and propagating through the structure (referred to as percolation regime). In this region, the scaling law for diffusivity is given as [11, 36, 80]

$$D_p \propto (C_d - C_{dc})^{\mu} \tag{33}$$

where C_{dc} is the conduction percolation threshold below which concentration of cracks is sparse and μ is a universal exponent (= 2 for three dimensional cases). The percolation threshold was determined to be 0.182 using numerical simulation for a specimen with randomly oriented penny shaped cracks by Charlaix [81]. It is assumed by Krajcinovic *et al.* [11] that a parallel connection exists between the nonintersecting microcracks still present in the system and the growing macrocracks. Thus the overall diffusivity is calculated as [11, 36]

$$D = \frac{D_i^0}{\tau}\left[\left(1 + \frac{32}{9}C_d\right) + \frac{(C_d - C_{dc})^2}{(C_{dec} - C_d)}\right] \tag{34}$$

where C_{dec} is the rigidity percolation threshold at which the cluster of cracks transects the volume. At the rigidity percolation threshold, the strength of the structure vanishes. The rigidity percolation threshold was determined to be 0.712 using numerical simulation by Sornette [82]. The effect of damage on the elastic moduli in this regime is not well investigated in the literature. Thus Eqs. (31) and (32) are assumed to be valid in the percolation regime as well which modifies the rigidity percolation threshold to 9/16 at which E and ν become zero [11, 36].

In summary, the model described here combines multi-ionic diffusion with chemical equilibrium calculations and continuum damage mechanics. The model can be used to predict distribution profiles of the various ions in solution and solid phases. Also, the progression of damage in space and time can be simulated, which then can be used to assess the durability of the structure.

2.4 Simulation Results

2.4.1 Model calibration and validation

Data on a test specimen was obtained from the literature [9, 83]. The specimen consisted of CSA Type 10 cement with water cement ratio 0.6 and density 1742 kg/m^3. Porosity of the specimen is experimentally found to be 0.52 by [9] and this value is used in the simulations. The specimen was a 7 cm diameter disk of height 20 mm which was immersed in 30 L of 50 mmol/L Na_2SO_4 solution at pH 10.3 for a year. All the faces of the sample were sealed except for one circular face so that diffusion can be simplified as a net 1-dimensional phenomenon. The external solution was renewed every 7 days. The initial pH of the pore solution is calculated to match the initial OH^- concentration as given in [9] and is used in the simulation. The comparison between the initial pore solution composition as computed by the proposed model and that experimentally determined by [9] is given in Table 2.4.

Table 2.4 : Comparison of pore solution compositions.

Ions	Computational results of proposed model (mmoles/L)	Experimental results by Samson and Marchand [7] (mmoles/L)
OH^-	465.0	429.3
Na^+	215.4	111.1
K^+	273.1	327.0
SO_4^{2-}	3.45	5.6
Ca^{2+}	1.03	1.3
$Al(OH)_4^-$	0.17	0.2

The calcium and sulfur profiles were measured at the end of 3 months, 6 months and 1 year. Model calibration parameters are the fraction of porosity available for solid product

deposition, i.e. b in Eq. (20), and tortuosity. The calibrated values were found to be 0.3 and 35 for b and tortuosity, respectively, to fit the experimental results of 3 months. The total available concentrations of the different species are obtained for a Portland cement paste of similar composition from the LeachXS database. 15 minerals are considered for dissolution/precipitation as shown in Table 2.2. The CSH phase is modeled using the 'solid solution model' developed by Kulik and Kersten [41, 84]. The model is based on the assumption that the CSH phase can be described by two concurrent solid solution systems – (i) mixture of amorphous silicon dioxide (SiO_2) and Tobermorite-I ($2CaO.2.4SiO_2.3.2H_2O$) and (ii) mixture of Jennite ($1.67CaO.SiO_2.2.1H_2O$) and Tobermorite-II ($0.83CaO.SiO_2.1.3H_2O$). The calibration results are shown in Figure 2.7.

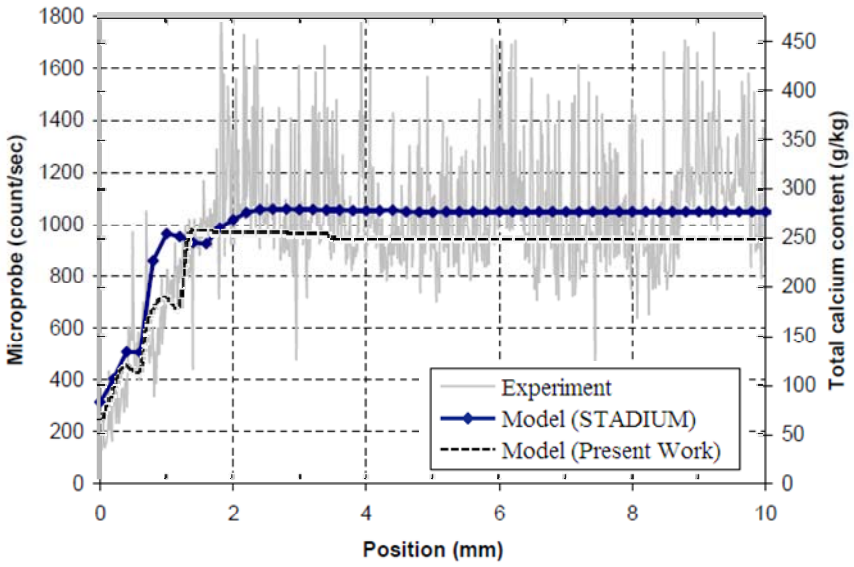

(a) Total calcium profile

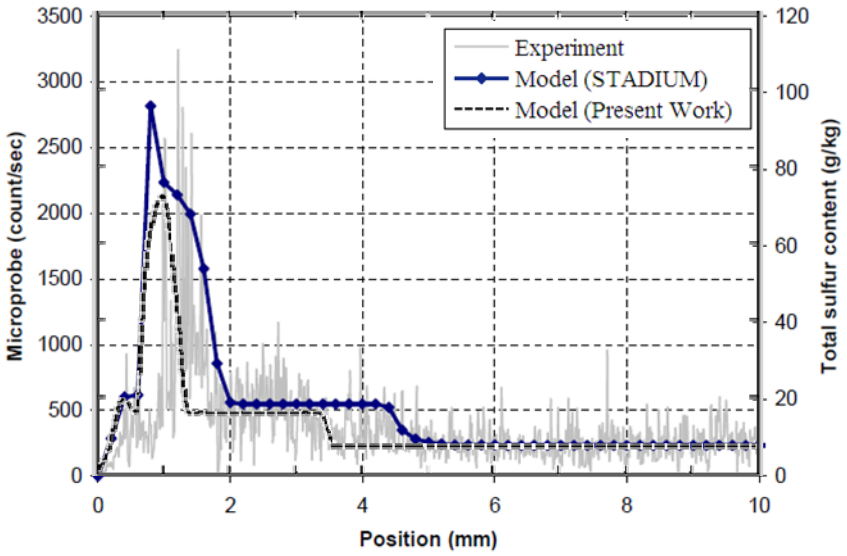

(b) Total sulfur profile

Figure 2.7 : Total calcium and sulfur profiles in solid phases at the end of three months after Samson and Marchand [7].

Experimental profiles (solid lines) for calcium and sulfur and the simulation results (solid-dotted lines) shown in Figures 2.7 and 2.8 were obtained from Samson and Marchand [9]. The experimental results performed by SIMCO technologies, Canada were scaled to match the simulation results performed using STADIUM software by Samson and Marchand [9]. The simulations performed using the model developed in this research (shown as dashed lines) are seen to qualitatively match with the experimental results. The initial mineral composition used in Samson and Marchand are based on the mass conservation law (equating amount of each species in the cement with that in the probable solid phases) whereas the initial mineral composition for the current simulations is obtained by attaining thermodynamic equilibrium along with the conservation of mass of each species in the cement and in the potential solid phases (mass conservation law as described above). The calibrated model as developed here then was used to validate the

model responses at the end of 6 months and 1 year using the experimental results as shown in Figure 8. The experimental results are the total concentrations of calcium and sulfur present as solid phases in the system. The model uses the available quantities (i.e. readily leachable) of the species to calculate the solid compositions in the system as mentioned earlier. Thus the total quantities are calculated by adding the unavailable quantities (= total quantity – available quantity) to the simulation results. The concentrations of the species are calculated at each node. As the concentration at a very small distance inside the structure ($x = \delta$) i.e. in between the first node (boundary corresponding to the external solution) and second node (inside the structure) is not known, the unavailable quantities are plotted at $x = 0$. In Figures 2.7 and 2.8, the calcium profiles show a decrease in concentration near the boundary due to leaching of calcium to the outside solution. The peaks in the sulfur profiles occur due to the formation of gypsum which are followed by ettringite formation, which can be identified as a further reduction in sulfur concentration in Figures 2.7b, 2.8b and 2.8d. Thus, the mineralogical evolution can be predicted from the numerical simulations, as well as the damage progression as presented below.

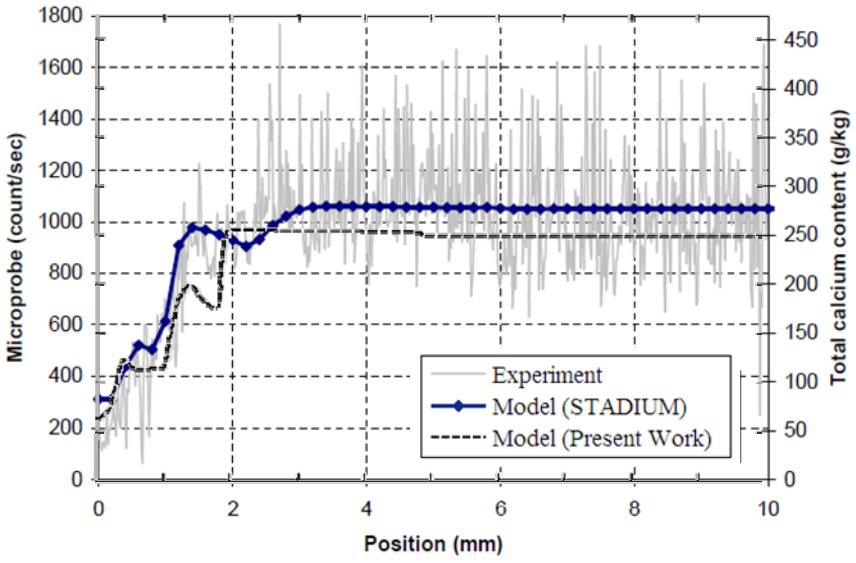

(a) Total calcium profile

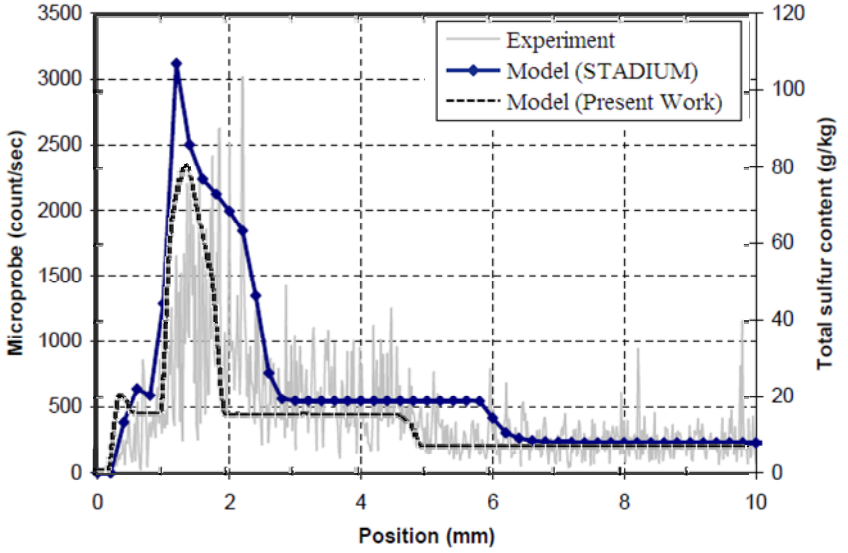

(b) Total sulfur profile

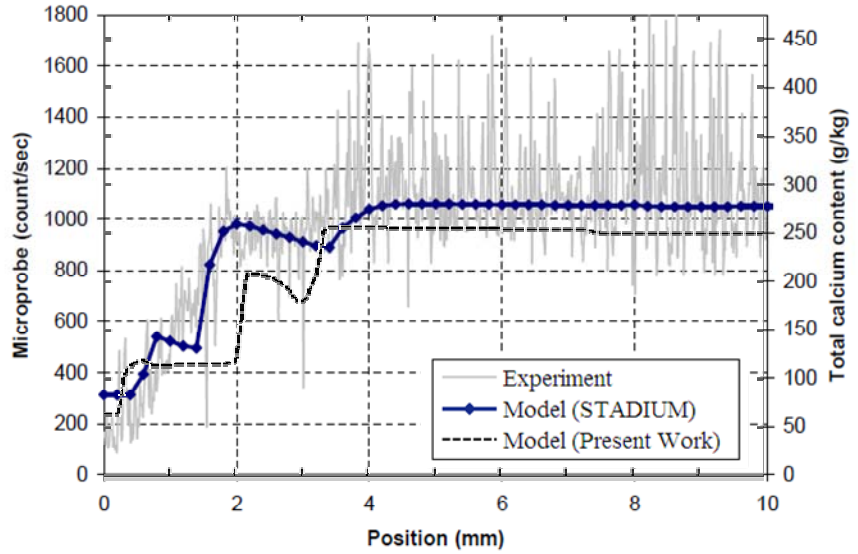

(c) Total calcium profile

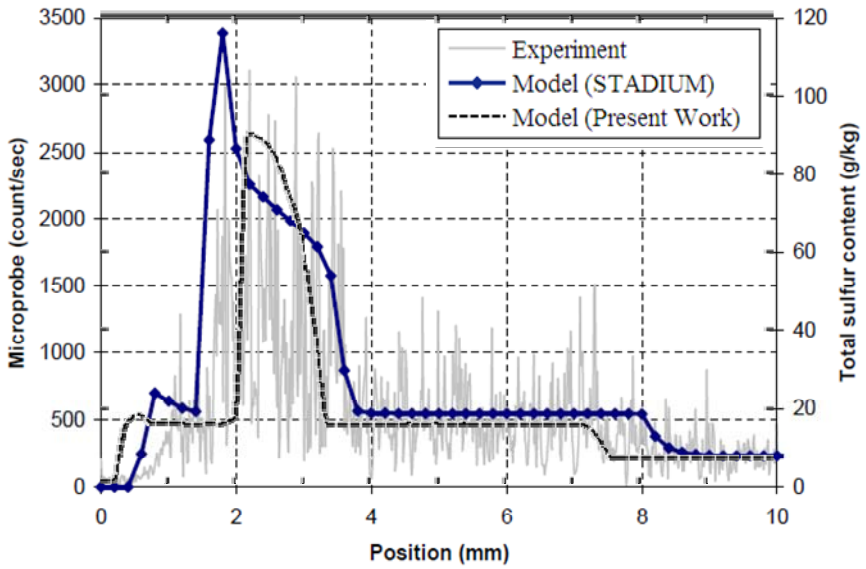

(d) Total sulfur profile

Figure 2.8 : (a), (b) – Total calcium and sulfur profiles in solid phases at the end of six months after Samson and Marchand [7]; (c), (d) – Total calcium and sulfur profiles in solid phases at the end of one year after Samson and Marchand [7].

The maximum value of the damage parameter for the purpose of the above simulations is assumed to be 0.9 instead of 1 to allow for the additional system uncertainties and

adequate margin in 'design' performance. The damage front progression for the experimental case simulated is estimated by the depth up to which all the elements are calculated to be cracked (i.e. damage parameter reaching its maximum value of 0.9) at the simulation time corresponding to the experimental results. The calculated damage front is calculated to be at 1.4 mm and 2.4 mm from the specimen boundary based on the numerical simulation after 6 months and 1 year, respectively as shown in Figure 2.9.

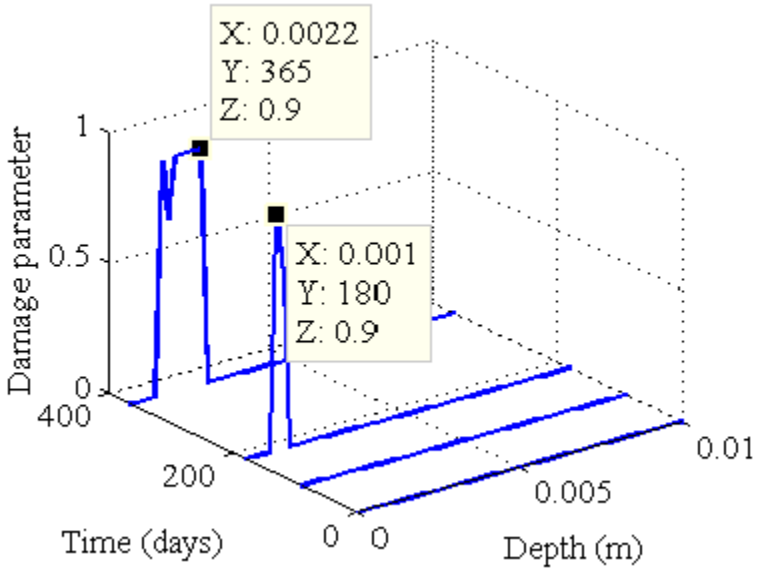

Figure 2.9 : Progression of damage parameter in time and space.

The drop in the damage parameter at approximately 1.2 mm as seen in the damage parameters profiles at the end of 6 months and 1 year is due to the fact that calcium leaching (which occurs simultaneously with cracking due to expansive product formation) increases porosity before the element is completely cracked. It is important to note that damage occurs not at the structure surface, but rather at some depth from the surface as a combined result of calcium leaching and sulfate attack. The indicated depth

of the initial damage is suggestive of the spalling depth generally observed in the literature, but this needs to be experimentally verified. The sample used in the reported experiment had a large porosity value (= 0.52) which allows for more solid product deposition before strain develops. Cement mortar and concrete samples generally have much smaller porosities (0.1 – 0.3). Thus strain develops more easily in the case of cement mortar and concrete samples than in cement paste samples.

2.4.2 Damage progression

Damage may not be a significant factor for short term performance, but it can affect the long term durability of the structures and therefore needs to be considered through numerical simulations. A structure fails under sulfate attack due to cracking, thus requiring consideration of the cracking progression as a function of initial conditions (i.e., formulation) and external conditions. The usefulness of the numerical modeling framework developed in this research in evaluating damage progression and subsequent failure of a structure is illustrated next.

A numerical simulation is performed on an example case to demonstrate the progression of damage in space and time. The simulated specimen is a US Type I cement mortar with porosity 0.3, cement:water:sand mass ratio 1:0.5:3, tortuosity 36, density 1800 kg/m^3. The fraction of available porosity is assumed to be 0.2. The specimen is immersed in a 0.35 M Na_2SO_4 solution (0.35 moles/L) and the solution is renewed every 7 days. The specimen is a 25 mm x 25 mm x 285 mm prism and the volume of the external solution is 1.78 L assuming liquid to solid volume ratio to be 10. All the six faces of the specimen are exposed to the external solution. This three-dimensional

problem is chosen to represent real life cases. In most of the experiments found in the literature, a specimen is immersed in an aggressive solution where all the faces of the specimen are exposed to the solution. Also, all the real life cases are three-dimensional. The numerical model proposed in this dissertation is one-dimensional. If simulations are needed for such real cases, it is essential to idealize them as one-dimensional problems. Thus the actual three dimensional problem is idealized to represent a one-dimensional problem as shown in Figure 2.10. For simplicity of demonstration, the structure is assumed to be a cube having each side to be of length L. The structure is divided into N hollow cubes (or shells) of thickness dx starting from outside towards the center of the specimen. The hollow cubes are labelled as A, B, C and D in Figure 2.10a. The three-dimensional structure is idealized as a one-dimensional structure as shown in Figure 10b. The area in contact with the external solution for the first element is $A = \mathbf{6}L^2$ and volume is $V = Adx$. This constitutes the first element of the one dimensional idealized structure which is labelled as A. The area of the second element is $A' = \mathbf{6}(L - dx)^2$ and volume is $V' = \mathbf{6}(L - dx)^2 dx$. This constitutes the second element of the idealized structure which is labelled as B. In this way, all the elements of the three dimensional structure can be idealized to represent one-dimensional elements. The three-dimensional structure is exposed to the external solution on all sides whereas the idealized structure is exposed to the external solution only on one side as shown by the arrows in the figure. This process can be modified to idealize a prismatic shape as is used in this example problem.

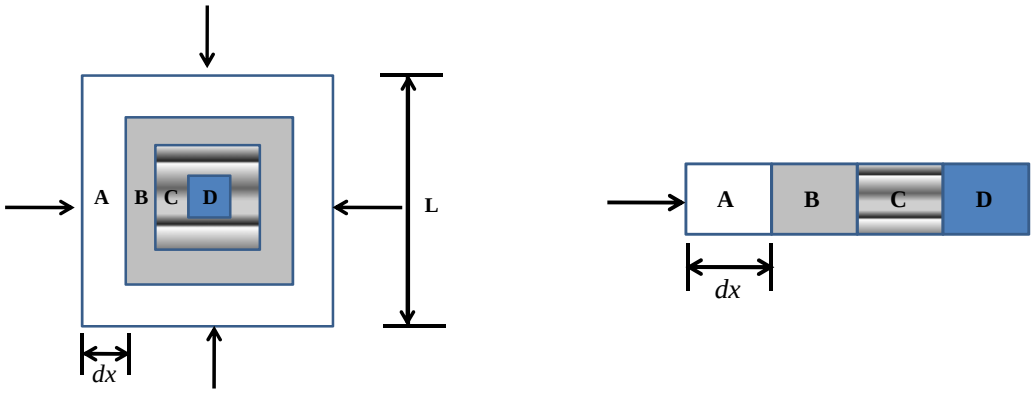

(a) Three dimensional structure (b) One dimensional idealization

Figure 2.10 : One dimensional idealization of a three dimensional structure.

Similar to the previous numerical simulation, the total available (i.e. readily leachable) concentrations of the different species were obtained for a Portland cement mortar from the LeachXS database. The available concentrations are lesser than the total concentrations of the species present in the system. The initial solid phase distribution along 25 mm dimension using the available concentrations of the ions is shown in Figure 2.11a, where the Y-axis is the amount of the indicated minerals in g/kg of the total material and X-axis is the depth within the material from the face in mm. Since the solid phase distribution is symmetrical about the center of the specimen, only a half-width is shown in the figures. It is important to note that the available concentration of Portlandite is more than that of CSH in Figure 2.11a. Portlandite reacts/leaches more easily than CSH which starts reacting only when Portlandite is depleted from the system. Therefore, the available quantity of Portlandite as shown in Figure 2.11a is most of the total quantity whereas the available concentration of CSH is a small fraction of the total quantity (available silicon concentration is 20% of the total quantity for this example problem).

The final solid phase distribution after one year of simulation is shown in Figure 2.11b. The complete dissolution of hydrogarnet combined with sulfate ion ingression contribute to the increase in ettringite concentration. It is also evident from Figure 2.11b that gypsum forms from Portlandite (calcium hydroxide) and sulfate ions (as shown in Eq. (1)) as the Portlandite dissolution front coincides with the gypsum formation front. Also, decalcification of CSH is seen by the dissolution of the Jennite-Tobermorite-II mixture as is expected when the structure is exposed to aggressive water [13, 31, 85]. Figure 2.11b also shows that at a depth up to approximately 0.5 mm ettringite is completely depleted. This is found to be due to the low pH value near the surface (below 8), which also corresponds with the literature reports [8]. Thus, the mineralogical features of the cementitious materials under sulfate attack are reasonably simulated using the numerical model developed in this research. The change in porosity due to the change in volume as a result of the chemical reactions is shown in Figure 2.12. The initial decrease in porosity is due to the formation of gypsum and ettringite. As soon as the available porosity is filled up, strain starts to develop which leads to cracking of the structure. After a while, porosity increases when calcium starts to leach out to the surrounding solution.

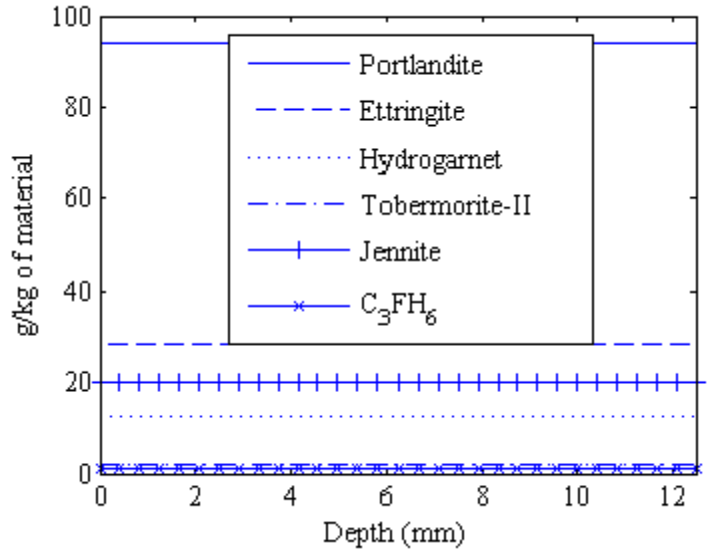

(a) Solid phase distribution of undamaged structure (initial condition)

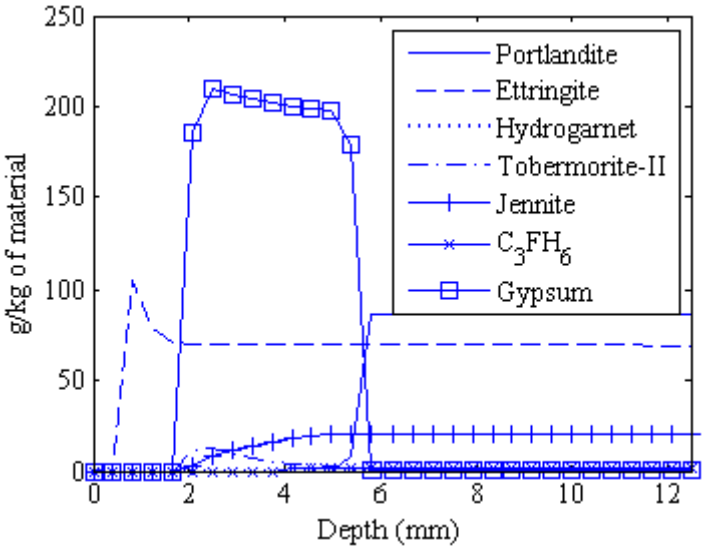

(b) Solid phase distribution after one year of simulation

Figure 2.11 : Distribution of the solid phases.

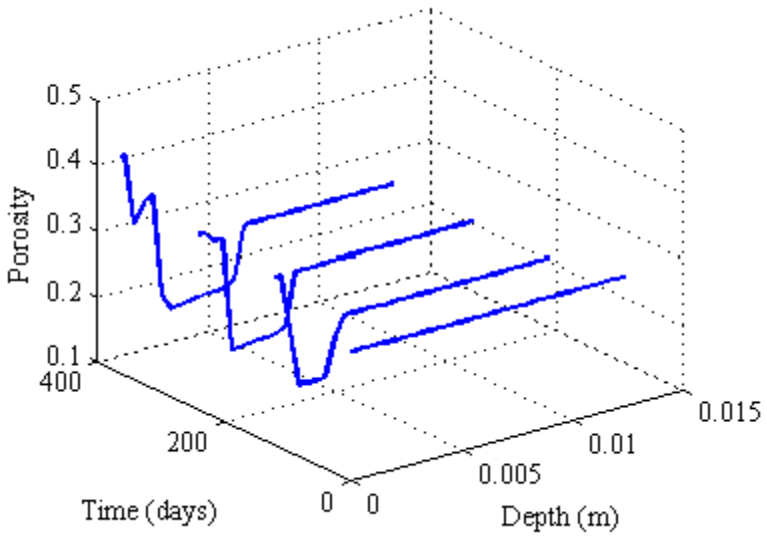

Figure 2.12 : Porosity profile with time and space.

Figure 2.13 shows the progression of damage with time and space. Figure 2.14 shows the damage front has progressed up to approximately 6 mm after one year. It is evident from Figures 2.11b and 2.12 that the damage front is coincident with the gypsum progression front (end of the peak of Gypsum is approximately at 6 mm). The calcium aluminate phase (for this case hydrogarnet phase) is completely consumed by sulfate to produce ettringite as can be observed in Figure 2.11b. If ettringite had initiated damage, the front would have moved to the end of the structure which is not the case as can be seen in Figure 2.12. As calcium hydroxide was available in the system, gypsum continued to form as sulfate ions continued to diffuse (refer to Eq. (1)). This corresponds to an increase in solid volume as can be seen from Table 2.1. This increase in volume leads to strain and cracking. This indicates that gypsum in addition to ettringite is a prominent contributor of volumetric expansion which was not included in the prior models as can be seen from Figure 2.3.

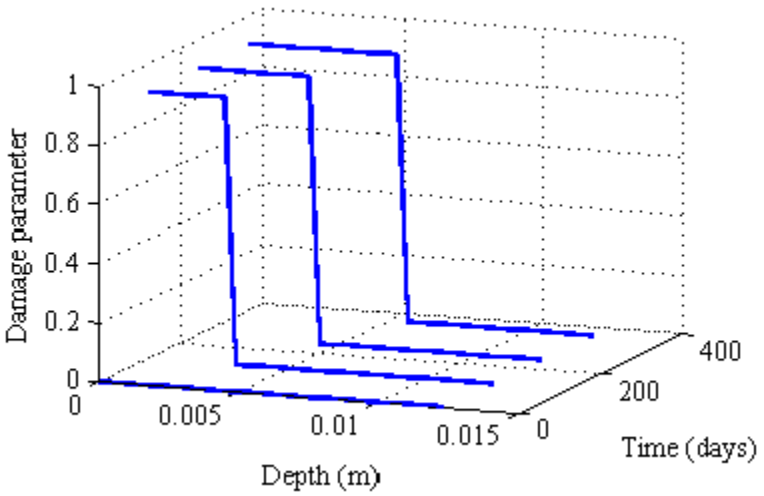

Figure 2.13 : Progression of damage parameter in time and space.

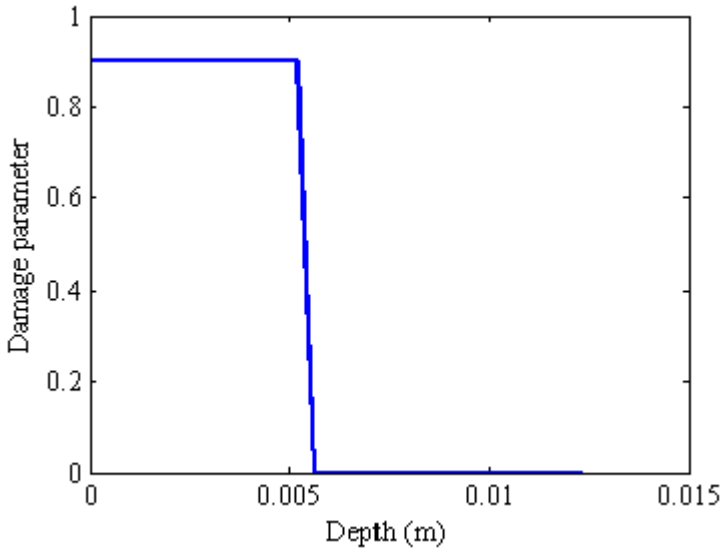

Figure 2.14 : Damage progression front at the end of one year.

As time progresses, the damage parameter increases with the increase in strain until it reaches the maximum value. The element is assumed to have failed when it reaches the completely cracked state characterized by the maximum damage parameter. More sulfate ions then diffuse in more rapidly through the cracks and more ettringite and gypsum are formed due to the chemical reactions, leading to failure of more elements. This increases

the rate at which damage front progresses. A failure criterion of the structure can be defined as the failure of all or some of the elements reaching the maximum damaged state. Finally, a time to failure of the structure can be obtained from the simulation. This type of simulation is especially useful in design for durability as well as for inspection and maintenance scheduling.

2.5 Conclusions

A numerical model for assessing the degradation of cementitious materials under sulfate attack is developed in this chapter. The model combines detailed approaches for the three essential components of degradation under sulfate attack: (1) multi-ionic diffusion under concentration gradient and chemical activity gradient, (2) chemical equilibrium calculation to determine the amounts of dissolution and precipitation of solid products, and (3) assessment of the cracked state of the structure that affects further diffusion of the sulfate ions using a continuum damage mechanics model. The model is calibrated and validated using experimental results obtained from the literature. This model can be used to determine the profiles of the ions and the minerals as well as the progression of structural damage in time and space. Thus this model can potentially be applied for the assessment of long-term durability of cementitious structures.

CHAPTER III

NUMERICAL SIMULATION OF CHANGE IN STRENGTH AND STIFFNESS OF CEMENTITIOUS MATERIALS DUE TO CHEMICAL REACTIONS

3.1 Introduction

Various chemical reactions take place between cement hydration products and the diffusing sulfate ions when a cementitious structure is exposed to aggressive sulfate containing environment as is mentioned in Chapters I and II. The chemical reactions alter the mineralogical compositions leading to changes in the mechanical properties of the structure. The numerical model described in Chapter II is extended in this chapter by incorporating changes in the mechanical properties of the structure due to changes in the mineralogical composition under exposure to aggressive sulfate rich environment. This extension of the previous model is shown as the damage assessment box in Figure 3.1.

The concrete structure is idealized as a homogeneous matrix by applying homogenization schemes at different length scales. The changes in the mechanical properties are obtained by using the compositions of the mineral phases at different time steps. Finally, the damage due to cracking and mineralogical evolutions are combined to obtain overall damage state of the structure. The numerical simulation framework developed for evaluating changes in the mechanical properties of the structures due to chemical reactions is described in this chapter. The improved model is calibrated and validated with the experimental results available from the literature.

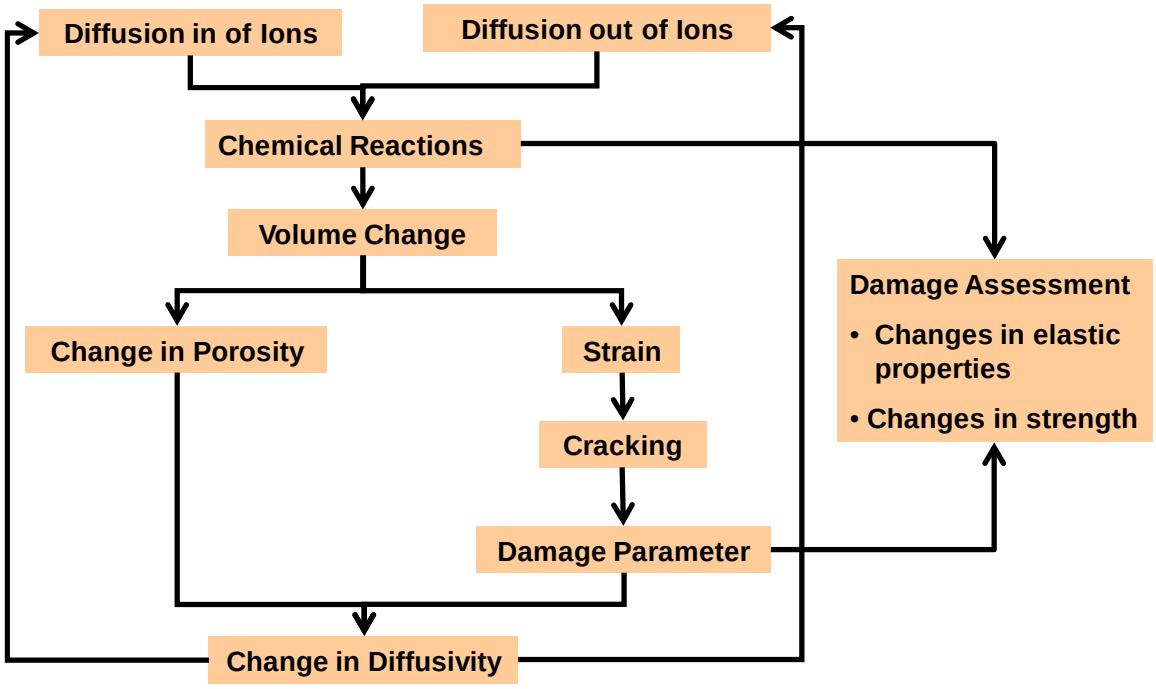

Figure 3.1 : Overview of the extended modeling framework.

3.2 Numerical Simulation Framework

Concrete can be viewed as a composite material where various phases at different length scales control its mechanical properties (see Figure 3.2).

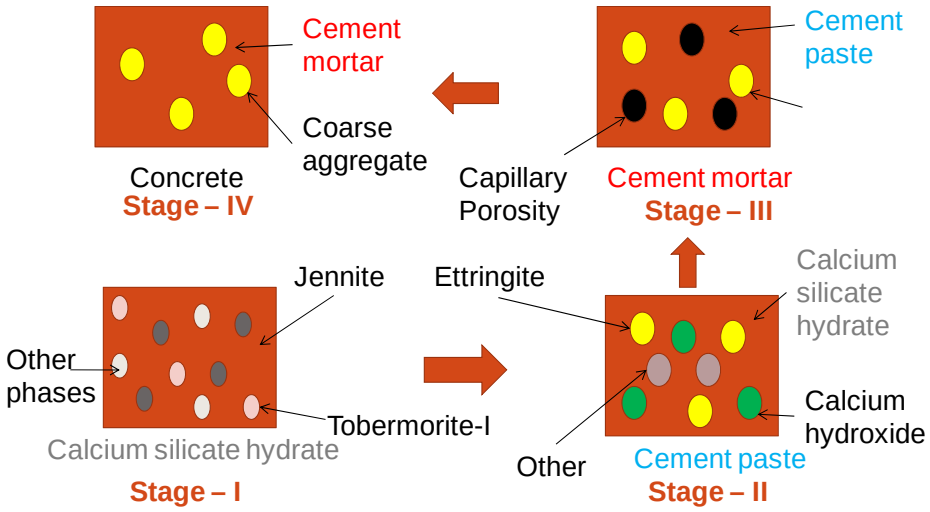

Figure 3.2 : Homogenization stages of concrete.

Various homogenization schemes have been used in the literature to estimate the mechanical properties at different stages of hydration of cementitious materials [44, 45, 86]. Yang and Huang [87] estimated the mechanical properties of concrete structures using the properties of cement pastes and aggregates obtained from the experiments. Guillon *et al.* [88] evaluated the effects of complete dissolution of various phases on the stiffness of the material using a homogenization scheme applied to a finite element code; but diffusion of various ions and the evolution of the mineralogical features as a function of time were not considered. Constantinides and Ulm [89] used another homogenization scheme to estimate mechanical properties of sound and leached pastes using volume fraction of various phases from the experiments. Bary [16] used a numerical model combined with a homogenization scheme to evaluate the effect of sulfate ingress and calcium leaching on degradation of cementitious materials. However, this model considers calcium and sulfur to be the only diffusing species and gypsum and ettringite to be the only products that form as a result of chemical reactions. Also, this model does not

consider the changes in the mineralogical characteristics of C-S-H as a result of calcium leaching. In this research, two homogenization schemes combined with Eshelby's equivalent inclusion method are used at different length scales to homogenize the multi-phase system to an equivalent homogeneous system at the macro-scale. Following Constantinides and Ulm [89], four homogenization stages (i.e. length scales) are considered as shown in Figure 3.2.

Stage I : This stage is composed of C-S-H which is the main cement hydration product. This phase is modeled as a combination of two concurrent solid solution systems [41] – (i) mixture of amorphous silicon dioxide (SiO_2) and Tobermorite-I ($2CaO.2.4SiO_2.3.2H_2O$) and (ii) mixture of Jennite ($1.67CaO.SiO_2.2.1H_2O$) and Tobermorite-II ($0.83CaO.SiO_2.1.3H_2O$). According to Taylor's C-S-H model, Jennite comprises the majority of the C-S-H phase in an undegraded structure [90]. However, the composition of C-S-H changes as the chemical reactions progress when the structure is exposed to aggressive environment.

Stage II : This is composed of various cement hydration products, e.g., homogenized C-S-H (from stage I), Portlandite, ettringite, hydrogarnet, gypsum. Application of a homogenization scheme at this stage results in a homogeneous cement paste phase. The composition of this phase also changes with time as a result of chemical reactions.

Stage III : Sand particles and capillary pores embedded in a homogenized cement paste phase (from stage II) comprise stage III. This is referred to as cement mortar. The interfacial transition zone is not considered to keep the formulation simple. This phase loses complete strength if all of the cement paste leaches out.

Stage IV : This stage is modeled as a cement mortar matrix with coarse aggregates embedded in it. This describes the macro-scale concrete structure.

The above mentioned stages are separated by at least one order of length magnitude. This condition is necessary to satisfy the separation of scales condition [91]. There is a discrete difference in modeling stages I/II and stages III/IV. Stages I/II are composed of various phases where the composition changes during the degradation process in a way that any phase may become dominant. However, a dominant phase can easily be identified throughout the degradation process for stages III (cement paste) and IV (cement mortar). Complete degradation of the dominant phases in stages III and IV signify complete loss of strength due to the loss of the binding material. Thus two different modeling approaches are used to simulate stages I/II and stages III/IV. A self-consistent approach is applied to model stages I/II where the elastic properties are estimated by solving simultaneous nonlinear coupled equations and Mori-Tanaka scheme is applied to model stages III/IV where the elastic properties are estimated by solving nonlinear simultaneous uncoupled equations. The general homogenization scheme is described below [44, 89, 92].

The macroscopic strain is assumed to be the volumetric average of the microscopic strains and is expressed as

$$\bar{\varepsilon} = \frac{1}{V}\int \varepsilon(\boldsymbol{x})dV = \langle \varepsilon_r \rangle_V \tag{35}$$

where $\boldsymbol{x}$ is the position vector, ε_r is the strain in phase r, V is the volume of the representative volume element and $\langle P \rangle_V$ represents volume average of the quantity P. The microscopic strain is related to the externally applied strain (ε^0) as

$$\varepsilon_r = A_r : \varepsilon^0 \tag{36}$$

where A_r is a fourth order tensor called the 'concentration factor' and is expressed as

$$A_r = [I + S : C_0^{-1} : (C_r - C_0)]^{-1} \tag{37}$$

where I is a fourth order identity tensor, S is a fourth order Eshelby tensor and C_0 and C_r are stiffness tensors of the reference phase and phase r. The stiffness matrices are defined as

$$C_r = 3k_r K + 2\mu_r J \tag{38}$$

$$C_0 = 3k_0 K + 2\mu_0 J \tag{39}$$

where k and μ are the bulk and the shear moduli, $K = \frac{1}{3}\delta_{ij}\delta_{kl}$ where δ_{ij} is the Kronecker delta function, and $J = I - K$. The Eshelby tensor is expressed as

$$S = \alpha K + \beta J \tag{40}$$

where for a spherical inclusion in a homogeneous matrix, the expressions for α and β reduce to

$$\alpha = \frac{3k_0}{3k_0 + 4\mu_0} \text{ and } \beta = \frac{6(k_0 + 2\mu_0)}{5(3k_0 + 4\mu_0)} \tag{41}$$

Using Eqs. (35) and (36), the relation between macroscopic strain and the applied strain is expressed as

$$\bar{\varepsilon} = \langle A_r \rangle_V : \varepsilon^0 \tag{42}$$

The macroscopic stress ($\bar{\sigma}$) and the macroscopic strain are related as

$$\bar{\sigma} = \bar{C} : \bar{\varepsilon} \tag{43}$$

where $\bar{C}$ is the homogenized stiffness tensor. Assuming that the macroscopic stress can be calculated as the volumetric average of the microscopic stresses, the homogenized stiffness tensor can be expressed as

$$\bar{C} = \langle C_r : A_r \rangle_V : \langle A_r \rangle_V^{-1} = 3\bar{k}K + 2\bar{\mu}J \tag{44}$$

where $\bar{k}$ and $\bar{\mu}$ are the homogenized bulk and shear moduli which can be expressed as [44]

$$\bar{k} = \sum_r f_r k_r (1 + \alpha \left(\frac{k_r}{k_0} - 1\right))^{-1} \times [\sum_r f_r (1 + \alpha \left(\frac{k_r}{k_0} - 1\right))^{-1}]^{-1} \quad (45)$$

$$\bar{\mu} = \sum_r f_r \mu_r (1 + \beta \left(\frac{\mu_r}{\mu_0} - 1\right))^{-1} \times [\sum_r f_r (1 + \beta \left(\frac{\mu_r}{\mu_0} - 1\right))^{-1}]^{-1} \quad (46)$$

where f_r is the volume fraction of phase r. The elatic moduli of various phases (i.e., k_r and μ_r values) are obtained from the literature [45, 88, 93] and are given in Table 3.1.

Table 3.1 : Mechanical properties of various phases [45, 88, 93].

Mineral/Aggregates	Formula	Bulk modulus, k_r (GPa)	Shear modulus, μ_r (GPa)
Calcium hydroxide	$CaO.H_2O$	40	16
Calcium monosulfate	$CaO.Al_2O_3.CaSO_4.12H_2O$	40	16
Gibbsite*	$Al(OH)_3$	14.9	9
Ettringite and Fe-Ettringite*	$3CaO.Al_2O_3.3CaSO_4.32H_2O$ and $3CaO.Fe_2O_3.3CaSO_4.32H_2O$	14.9	9
Hydrogarnet and Fe-Hydrogarnet*	$3CaO.Al_2O_3.6H_2O$ and $3CaO.Fe_2O_3.6H_2O$	14.9	9
Stratlingite* and Fe-Stratlingite*	$2CaO.Al_2O_3.SiO_2.8H_2O$ and $2CaO.Fe_2O_3.SiO_2.8H_2O$	14.9	9
Gypsum	$CaO.SO_3.2H_2O$	42.5	15.7
Iron hydroxide	$Fe(OH)_3$	14.9	9
Jennite	$1.67CaO.SiO_2.2.1H_2O$	18.9	11.9
Tobermorite-II	$0.83CaO.SiO_2.1.3H_2O$	13.9	8.8
Tobermorite-I	$2CaO.2.4SiO_2.3.2H_2O$	18.9	11.9
Silica gel	SiO_2	0.4	0.5
Gravel	-	69	0.23
Sand	-	80	0.21

* Assumed to be same as that given for C-S-H in Haecker *et al.* due to the lack of data.

This approach is known as the self consistent scheme if $C_0 = \bar{C}$ in Eq. (39) and the Mori-Tanaka scheme if $C_0 = C_m$ where m represents the matrix or the dominant phase. Finally, the homogenized Young's modulus can be calculated as

$$\bar{E} = \frac{9\bar{k}\bar{\mu}}{3\bar{k} + \bar{\mu}} \tag{47}$$

A structure fails as a result of cracking and loss of strength due to sulfate attack and calcium leaching. Thus it is important to evaluate the interaction of these two failure modes. When calcium in the pore solution decreases, calcium silicate hydrate dissociates into silica gel releasing calcium in the pore solution. This leads to an increase in porosity that creates more space for solid product deposition before strain can develop; hence the process of cracking under tension is delayed. Thus calcium leaching acts as a beneficial process with respect to cracking. On the other hand, when sulfate starts diffusing into the structure, gypsum and ettringite form that may lead to cracking and hence increased leaching and diffusion. Thus cracking aggravates both calcium leaching and sulfate attack. The numerical model is capable of representing these effects as shown in chapter II. Additionally, formation and deposition of additional products in the pore increases the compressive strength as more material is present to resist the compression. But the same argument may not be true in case of tensile strength as the newly deposited material may not be perfectly bonded so that it can resist the tensile stress. Thus it is assumed in this dissertation that the deposition of additional solids in the pore will increase the compressive strength, but not the tensile strength.

As mentioned earlier, the structure experiences tensile stress due to the formation of expansive products under sulfate attack. The three dimensional volumetric expansion results in three dimensional tensile strain which may lead to cracks in three axial directions. In a compressive strength assessment experiment, the specimens at various stages of their degradation are taken out of the aggressive solution and a uniaxial compressive load is applied on them to evaluate their compressive strength. When a three dimensional structure is subjected to uniaxial compressive load, it experiences a tensile

stress in the directions perpendicular to the axis of application of the compressive load. A preexisting crack perpendicular to the axis of load application closes due to load reversal (tensile to compressive), but the cracks perpendicular to the other axes open up under tensile load that ultimately leads the structure to failure. Detailed analysis of this phenomenon requires three dimensional numerical modeling of the damage mechanics. This could be achieved by extending the present one-dimensional model to three-dimensions. In order to simplify the problem, it is assumed in this chapter that the relative change in the effective Young's modulus is equivalent to the relative change in the compressive strength of the structure. In this regard, alternative relations between the Young's modulus and the compressive strength available from the literature [51] can also be used. It is also assumed that the effect of the changes in chemical composition of the structure due to the exposure to an aggressive environment and cracking can be obtained by superimposing the effect of one factor (e.g., changes in chemical composition which results in $\bar{E}$) on another (e.g., cracking which is manifested in C_d). This approach has been used previously by many researchers to evaluate the effects of various factors on material properties [6, 94-99] and it is commonly known as the multifactor law [100]. The effective Young's modulus in compression at the macroscale is then calculated as

$$E_{\text{eff}} = \bar{E}\left(1 - \frac{16}{9} C_d\right) \tag{48}$$

3.3 Model Calibration and Validation

Experimental results are gathered from the literature for the purpose of calibrating and validating the model presented in the previous section. This is achieved in two steps – (a) calibration and validation of the model for evaluating strength loss due to calcium

leaching only and (b) calibration and validation of the model for evaluating strength loss due to combined calcium leaching and sulfate attack.

3.3.1 Strength loss due to calcium leaching

The experimental data for strength loss due to calcium leaching are obtained from Nguyen *et al.* [101]. A concrete cylinder of 110 mm diameter and 220 mm height is immersed in 6 moles/L of ammonium nitrate solution for a period of approximately 700 days after curing the sample for five months in water. Ammonium nitrate solution creates a more aggressive environment for leaching than deionized water [101, 102]. The specimen is composed of ordinary Portland cement, sand and gravel with a mass ratio of 1:1.82:2.8 and water-cement ratio of 0.6. Both ends of the specimen are sealed so that diffusion only occurs through the curved area of the specimen. The volume of the external solution is chosen in the experiment in such a way that renewal of the solution can be avoided if pH is less than 8.2. Thus the pH is fixed at 8 in the numerical simulation. The structure is divided into 80 elements and concentration and pH of the external solution at the boundary is kept fixed throughout the simulation. Initial solid composition as calculated by the chemical reaction module (ORCHESTRA) is given in Table 3.2.

Table 3.2 : Initial solid composition.

Solid phases	Quantity (moles/m^3)
Portlandite	1.3×10^3
Ettringite	49.63
Hydrogarnet	1.3×10^2
Tobermorite-II	1.63×10^2
Jennite	1.04×10^2
Fe-Hydrogarnet	75.68

Porosity and tortuosity of the specimen are calibrated to satisfy two conditions – (i) the sum of the volumes of the aggregates, minerals and pores is equal to the volume of the representative volume element; and (ii) the error between the experimental results and the model responses is minimal. The calibrated values are 0.15 and 120 for porosity and tortuosity, respectively. Figure 3.3 shows a comparison of the model response and the experimental results of mean stiffness as a function of time.

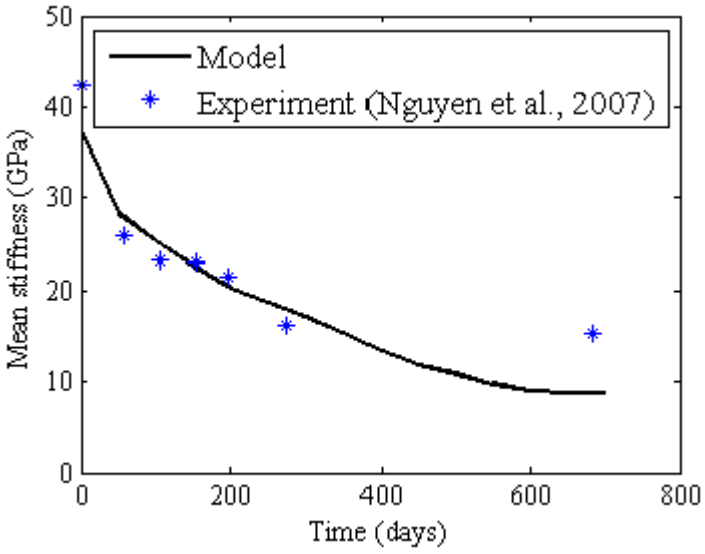

Figure 3.3 : Mean stiffness as a function of time.

The difference between the model response and the experimental results is mainly due to the assumed values of the porosity, tortuosity, the elastic moduli of different phases. It is important to acknowledge that the model similar to all available numerical models is based on various assumptions and approximations which may also contribute to the difference between model predictions and experimental observations. It is also important to note that calibration of the necessary parameters requires much more than the available data. Nguyen *et al.* determined the extent of the degradation by adding phenolphthalein that turns from colorless to pink around pH 9. Thus the depth up to which pH < 10 is plotted as a function of the square root of time using the calibrated parameters and compared to the experimental results as shown in Figure 3.4. The figure shows an acceptable agreement between the experimental results and the numerical simulation results given the fact that there are numerous parameters not available for this particular experiment (e.g., pH and renewal rate of the external solution, volume of the external tank and elastic moduli of sand and gravel) that need to be assumed for the simulation.

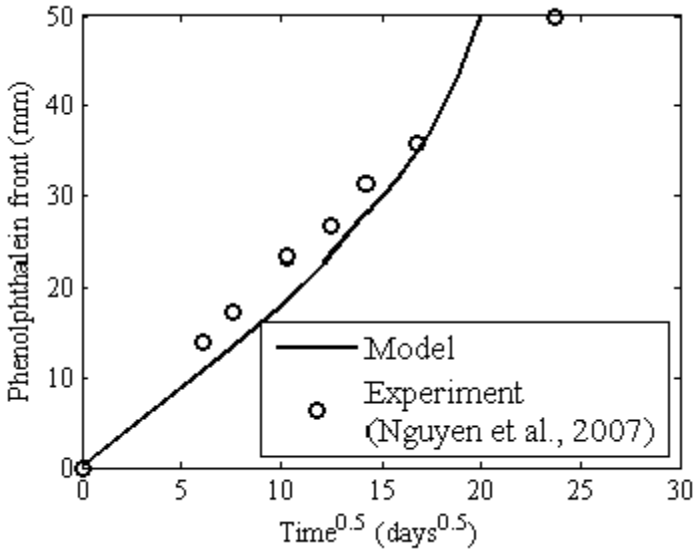

Figure 3.4 : Degradation depth as a function of square root of time.

3.3.2 Strength loss due to combined effect of calcium leaching and sulfate attack

The experimental data for compressive strength of an ordinary Portland cement mortar sample under the combined effect of calcium leaching and sulfate attack are obtained from Akoz *et al.* [103]. The oxide composition of the Portland cement is obtained from Akoz *et al.* The specimens of size $40 \times 40 \times 160$ mm are cured in lime saturated water at 20^0C for 27 days. Then they are immersed in Na_2SO_4 solution of 2700 mg/L (Exp 1), 18000 mg/L (Exp 2) and 72000 mg/L (Exp 3) except for some control specimens. Cement-sand mass ratio is 1:3 and water-cement ratio is 0.5. The experiment is performed for 300 days. The structure is divided into 50 elements for simulation purposes. The concentration of external solution is renewed every 14 days and pH of the solution is restored to 7 (assumed value due to the lack of data). The volume of the immersion tank is assumed to be 10 times the volume of the specimen as no

information is available on the size of the tank. The initial solid composition as calculated by the chemical reaction module is given in Table 3.3.

Table 3.3 : Initial solid composition.

Solid phases	Quantity (moles/m^3)
Portlandite	1.28×10^3
Ettringite	37.25
Hydrogarnet	2.01×10^2
Tobermorite-II	1.77×10^2
Jennite	1.13×10^3
Fe-Hydrogarnet	85.95
Brucite	1.23×10^2

The model parameters are calibrated using the results of Exp 3 (Figure 3.5) and validated with the results of Exp 1 and 2 (Figures 3.6 and 3.7). The calibration parameters are porosity (0.25) and tortuosity (50) and the fraction of porosity available for solid product deposition (0.55). It is evident from Figure 3.5 that there is a significant decrease in the strength of the specimen under 72000 mg/L of Na_2SO_4 solution. Figure 3.6 shows that there is very little increase in strength followed by a very small decrease in strength under 18000 mg/L of Na_2SO_4 solution. But the change in strength of the specimen under 2700 mg/L of Na_2SO_4 solution is not significant as shown in Figure 3.7. The increase in strength is due to the precipitation of ettringite and gypsum if no cracks form. Strength starts decreasing as soon as cracks form. Increase in concentration of sulfate solution increases the amounts of gypsum and ettringite formation that results in crack formation and finally loss of strength. Figure 3.8 shows the damage parameter profiles under three different concentrations of sulfate solution at the end of 300 days.

The maximum value of the damage parameter is assumed to be 0.9 instead of 1 to allow for additional system uncertainties and adequate margin in design performance. It can be seen from the figure that there is no crack development in the structure exposed to 2700 mg/L of sulfate solution. Sulfate attack and calcium leaching are simultaneous and competing processes. Calcium leaching increases porosity which in turn delays the cracking process under sulfate attack. The effects of these simultaneous processes are manifested in the damage profile for 18000 mg/L of sulfate solution. The damage parameter rises to approximately 0.56 near the boundary (1st element) and then decreases to approximately 0.1 (2nd element) and then rises back up to 0.35 (3rd element). Figure 3.9 shows higher porosity at approximately 1.4 mm at the end of 300 days for the specimen under 18000 mg/L of sulfate solution than that under 72000 mg/L of sulfate solution. The higher porosity prevented cracks to grow further as shown in Figure 3.8. Crack formation was most prominent for the specimen exposed to 72000 mg/L of sulfate that resulted in significant loss of strength of the specimen as shown in Figure 3.5. It is important to note that strength loss under sulfate attack is mostly governed by the crack formation, and effect of calcium leaching and C-S-H deterioration on strength loss is not very significant.

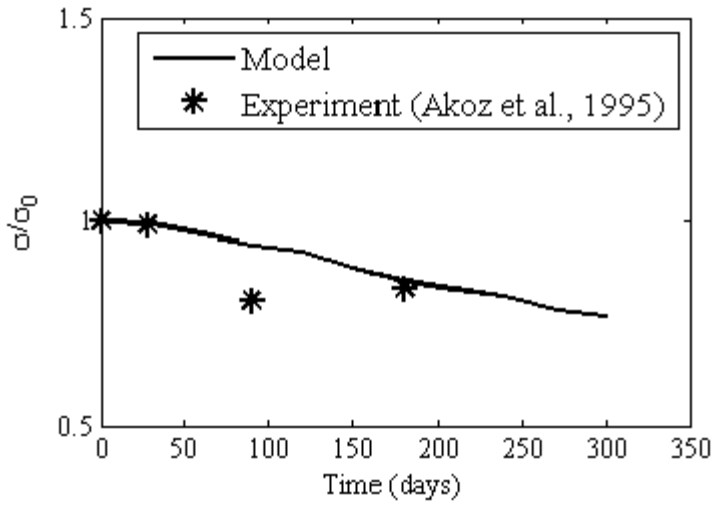

Figure 3.5 : Changes in compressive strength under 72000 mg/L of sodium sulfate solution.

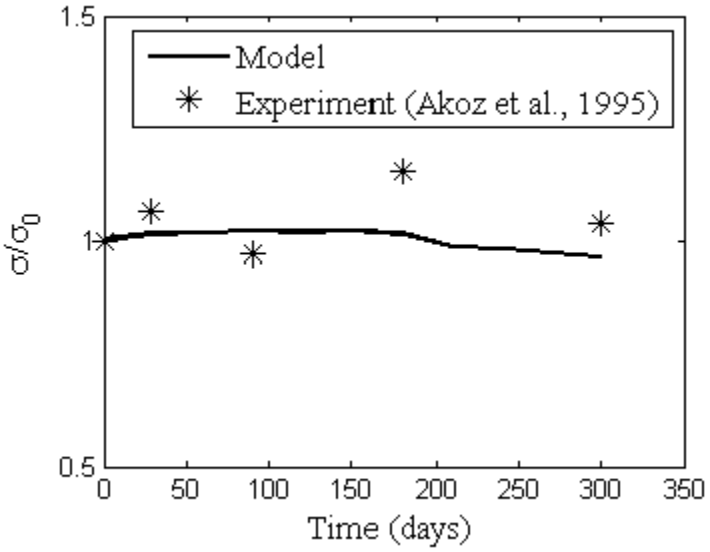

Figure 3.6 : Changes in compressive strength under 18000 mg/L of sodium sulfate solution.

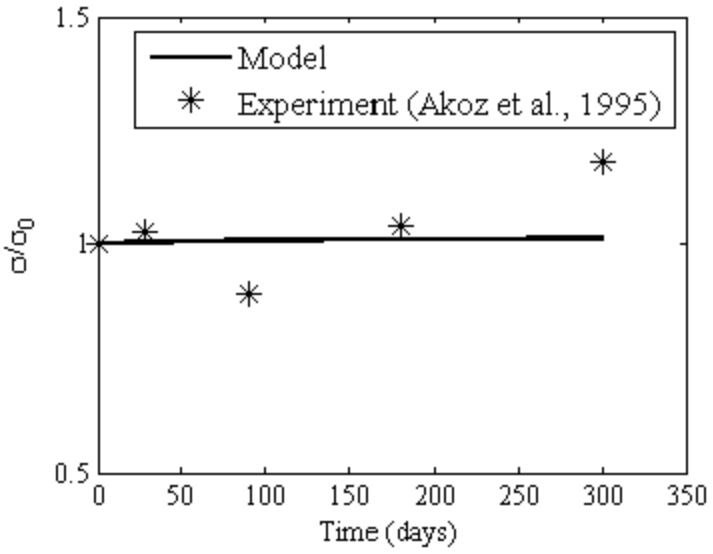

Figure 3.7 : Changes in compressive strength under 2700 mg/L of sodium sulfate solution.

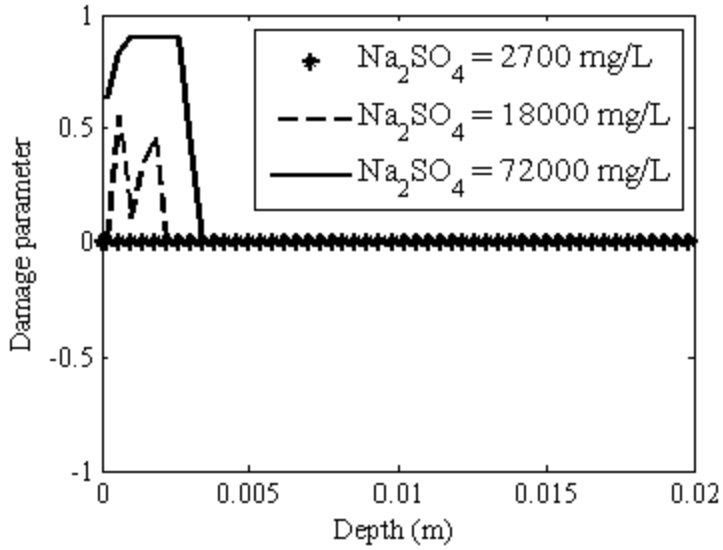

Figure 3.8 : Damage parameter profile at the end of 300 days for various concentrations of sodium sulfate solution.

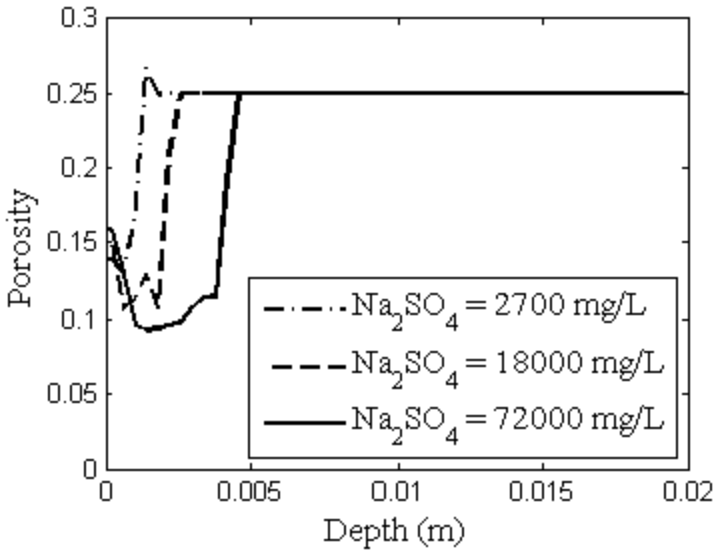

Figure 3.9 : Porosity profile at the end of 300 days for various concentrations of sodium sulfate solution.

3.4 Conclusions

A numerical model for assessing the degradation of cementitious materials exposed to sulfate solution is described in Chapter II and it is extended in this chapter. The previous model combined detailed approaches for three essential components of degradation: (1) multi-ionic diffusion under concentration and chemical activity gradients, (2) chemical equilibrium calculation to determine the amounts of dissolved and precipitated solid products, and (3) assessment of the cracked state of the structure using continuum damage mechanics. In this chapter, the model is extended by incorporating a continuum micromechanics based approach for the assessment of changes in the strength of the structure due to changes in its mineralogical composition during degradation e.g. formation of expansive phases such as ettringite and gypsum and dissolution of solid phases such as calcium hydroxide and calcium silicate hydrate (i.e. commonly known as calcium leaching). The improved model can be used to evaluate the elastic properties and

the strength of the structure as a function of time in addition to the profiles of the ions and the minerals as well as progression of cracking in time and space.

CHAPTER IV

SENSITIVITY ANALYSIS

4.1 Introduction

Identification of influential parameters is helpful in designing and maintenance scheduling of a structure for long-term durability. Use of a reliable numerical model can save time and cost when used judiciously in conjunction with experimental validation. In this regard, very few numerical studies are available in the literature that evaluate the effects of external and internal factors using a numerical model [33] that includes robust representation of chemical and physical processes. The numerical model that has been shown to be able to reproduce the trends in the experimental results with reasonable accuracy in the Chapters II and III, is used in this chapter to evaluate the effects of various factors on the response of the structure. The results of the numerical sensitivity analysis are then used to interpret implications of such changes in the field conditions.

4.2 Sensitivity Analysis Framework

Seven parameters are selected for sensitivity analysis – pH, concentration and renewal rate of external solution, initial porosity and tortuosity of the structure, available fraction of porosity (b in Eq. (20) in Chapter II), and cement type. A base test case, about which specific variables are varied as part of sensitivity analysis, is defined using a $50\ \text{mm} \times 50\ \text{mm} \times 50\ \text{mm}$ US Type I cement mortar sample immersed in a tank. All faces are exposed to a 350 mmol/L of Na_2SO_4 solution. The initial pH value for external

solution is 7 and volume of the tank is chosen to be 30 L. The volume of the tank is chosen to be large (as opposed to 4 ×volume of the solid as recommended in ASTM C1012 [20]) so that the changes in the external solution do not influence the results from other factors. Initial porosity and tortuosity are assumed to be 0.25 and 100. The mass ratio of cement to water to sand is assumed to be 1:0.5:3. A 2 year period is simulated with these basic values unless otherwise specified and one factor is varied at a time while fixing the other factors at their basic values. A one-dimensional idealization scheme is adopted as shown in Figure 2.10 of Chapter II. Half of the structure is divided into 51 elements where the first cell represents the external solution.

4.2.1 External solution pH

The external solution pH is fixed at values of 3, 5, 7, 9 and 12. The external solution concentration and pH are restored to the starting values at every renewal occurrence, which is 7 days in the base case. The simulations are performed for 10 years to magnify the effects of pH on the degradation of cement-based structures. Stability of solids in the cement matrix is dependent on the pore solution pH which is affected by the pH of the surrounding solution. Figure 4.1 shows the pH profiles of the pore solutions after 10 years. It is evident from Figures 4.1 and 4.2 that the calcium-leached depth increases with decreasing pH. This phenomenon was also observed by Cao *et al.* [31]. He investigated the effect of three pH values i.e. 3, 7 and 12 on the strength of the structure. It is important to note that calcium profiles for pH – 5, 7, and 9 are close while the calcium profiles for pH = 3, 7 (or 5 or 9) and 12 are widely separated. It is also important to note that complete dissolution of calcium phases near the boundary is seen in the simulations

(Figure 4.2). This may not reflect the real situation as kinetic aspect of the reactions is not included in the present model and external solution pHs of 3 and 12 are considered extreme environmental conditions. Thus a certain amount of calcium will probably be present even if the structure is exposed to aggressive environment for a long time. Porosity increases due to calcium leaching which enhances further diffusion. Diffusion of more sulfate increases the formation of more ettringite and gypsum that may lead to more cracking. In contrast, the increase in porosity (pore space) for solid product deposition as a result of calcium leaching delays cracking. Thus the degradation of structures is dependent on the relative rates of diffusion of sulfate ions and calcium leaching. These competing processes result in damage front progression rates that are not significantly different from each other as shown in Figure 4.3. The decrease in pH increases calcium leached depth, but it may not increase the rate of damage progression significantly. In this respect, the use of a numerical model can provide important insights to the mineralogical characteristics and degradation of the structure and provide a useful basis for further experimental verification.

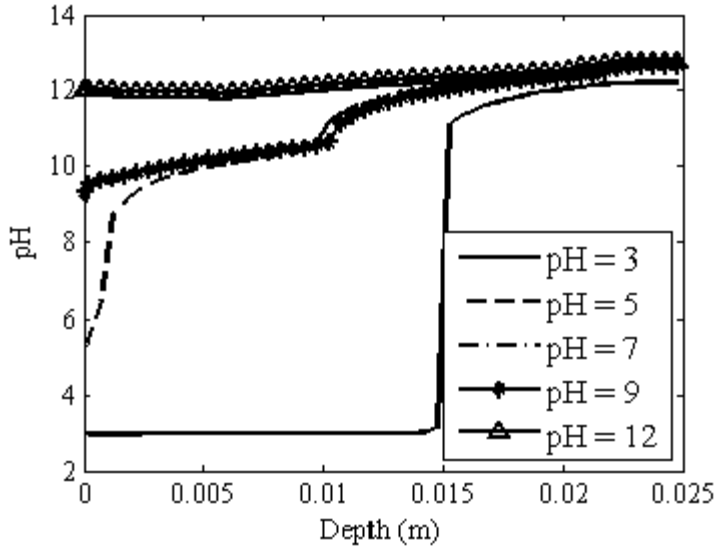

Figure 4.1 : Effect of external solution pH on pore solution pH profiles after 10 years of simulated immersion.

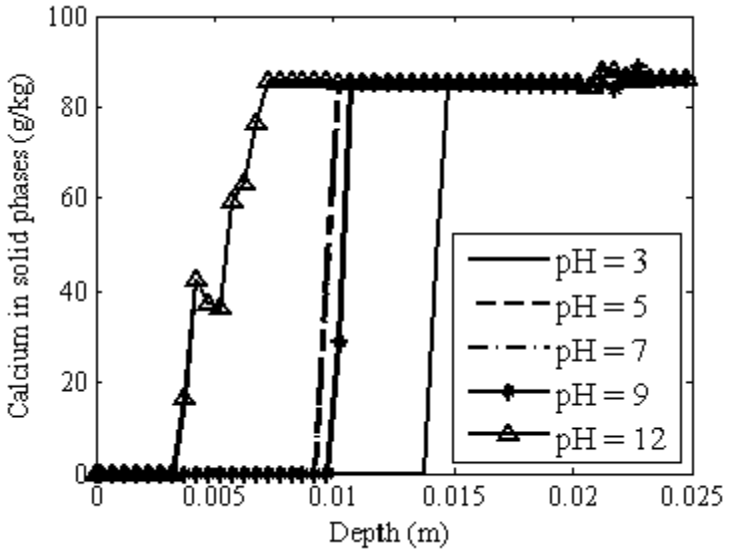

Figure 4.2 : Effect of external solution pH on calcium profiles after 10 years of simulated immersion.

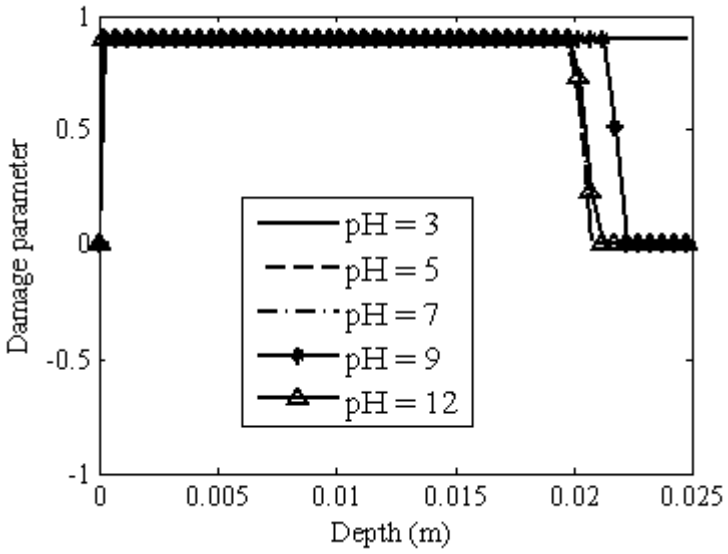

Figure 4.3 : Effect of external solution pH on damage progression after 10 years of simulated immersion.

4.2.2 External solution concentration

The concentration of external sulfate solution is fixed at five different values – 0.15, 0.25, 0.35, 0.45, and 0.55 moles/L. Higher concentration of sulfate in the external solution induces a higher concentration gradient which enhances diffusion of more sulfate ions. This leads to formation of more ettringite and gypsum which can be observed as progressively broader peaks of sulfur in solid phases in Figure 4.4. Formation of more ettringite and gypsum leads to more cracking which enhances further diffusion of sulfate ions which in turn induces more damage. Figure 4.5 shows the rate at which the damage progresses that is more rapid for higher concentrations of sulfate solution. Thus the model described in this research can be used to estimate the rate of damage progression and hence service life of the structure exposed to a particular concentration of sulfate.

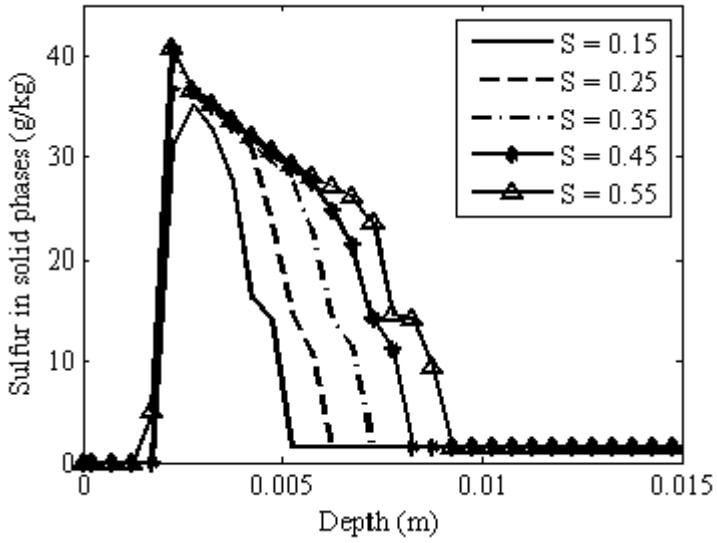

Figure 4.4 : Effect of external solution concentration on sulfur profiles after 2 years of simulated immersion.

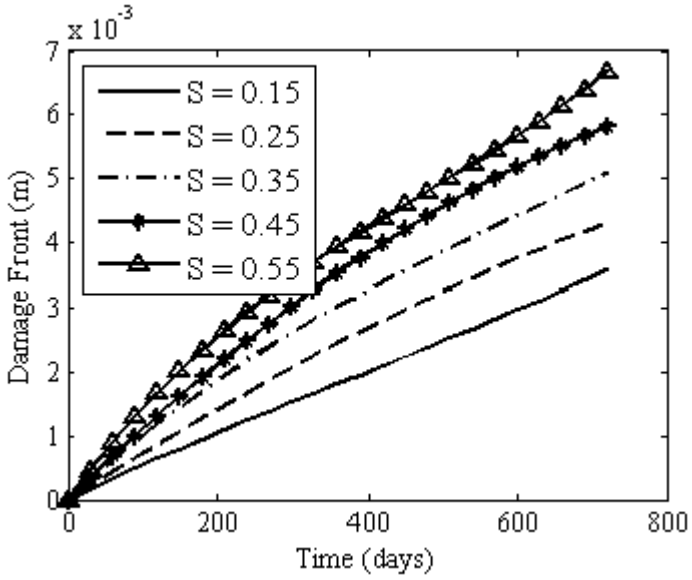

Figure 4.5 : Effect of external solution concentration on rate of damage progression after 2 years of simulated immersion.

4.2.3 Renewal rate of external solution

Ions can diffuse into an underground structure from the surrounding soil. The saturation level and the amount of ions in the soil are dependent on the fluctuating level of groundwater and percolation from the surface due to precipitation. The pH and concentration of the external solution in contact with the structure change in response to soil pore water flow. In many case the surrounding soil is not a significant source of sulfate. Immersion tests are generally performed to assess the degradation of the vault concrete materials. In this case, the renewal rate of the external solution also plays an important role on leaching of various species from the structure. Thus numerical simulations are performed to evaluate the effect of renewal rate of external solution on the response of the structure. Six renewal rates are chosen for this purpose – 1 day, 7 days, 14 days, 30 days, 180 days and no renewal for 2 years. 1day, 7 days and 14 days renewal rates represent frequent rain incident in the field; 30 days represents moderately humid area where rain and groundwater fluctuation are common; 180 days and 2 years represent relatively and extremely dry areas respectively. The volume of the external solution is fixed at 0.5 L (4 times the volume of the solid) for this particular simulation to magnify the effect of the renewal rate. Increasing frequency in renewal rate results in more aggressive conditions than less frequent renewal rates. Figure 4.6 shows that the calcium leached depth is more for frequent renewal rate than that for rare renewal rate. Calcium leaching increases porosity of the structure which in turn increases further diffusion of sulfate; but it also increases the available pore space for solid product delaying cracking. Thus the competing processes of calcium leaching and diffusion of sulfate result in similar rates of damage progressions for renewal rates up to 1 month, but

then it becomes progressively slower for renewal rates of 6 months and no renewal as shown in Figure 4.7. The behavior of the structure as seen in Figure 4.7 would be impossible to predict from intuitive reasoning without performing experiments or numerical simulations.

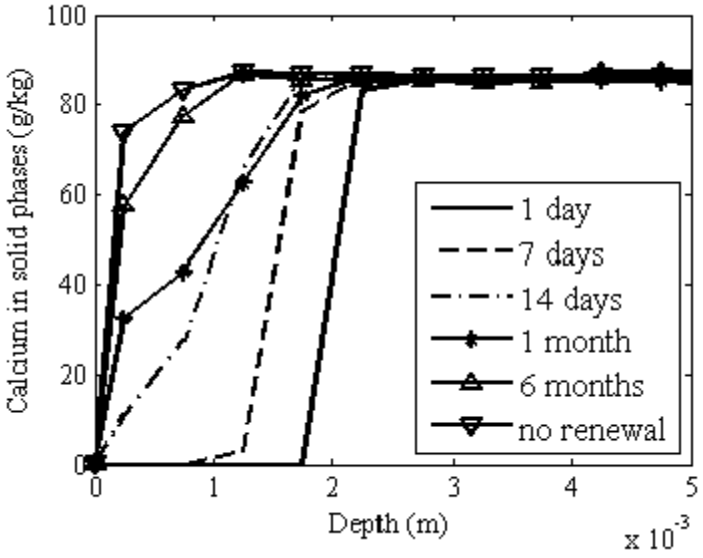

Figure 4.6 : Effect of renewal rate of external solution on calcium profiles after 2 years of simulated immersion.

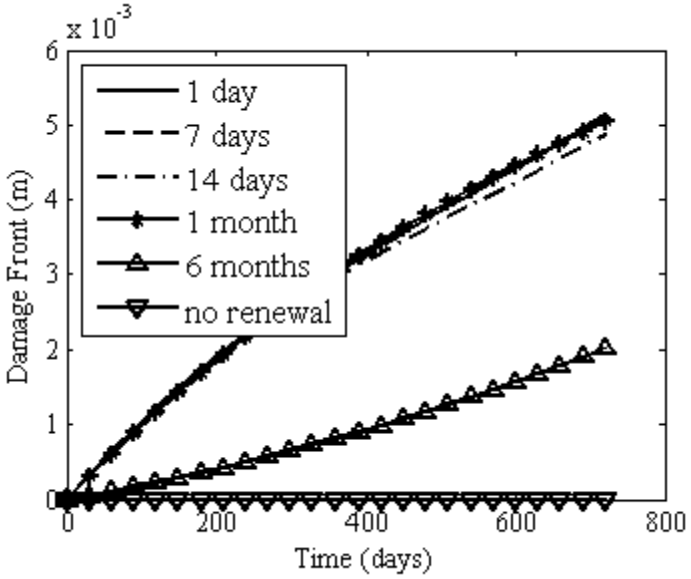

Figure 4.7 : Effect of renewal rate of external solution on rate of damage front progression after 2 years of simulated immersion.

4.2.4 Initial Porosity

The initial porosity is fixed at 0.15, 0.2, 0.25, 0.3 and 0.35 to evaluate the effect of the initial porosity on the response of the structure. Ions diffuse faster if porosity is more which leads to faster formation and dissolution of solids. In contrast, the available solid volume is less if porosity is greater in a fixed representative volume element, which results in the availability of less solid phases for reaction. As the available fraction of porosity (*b*) is fixed in the simulations, less solid volume is needed to initiate strain in a less porous structure resulting in faster formation of cracks. Thus a linear empirical relation cannot be established between the initial porosity and the loss of strength because of the aforementioned competing processes. Figure 4.8 shows that the movement of sulfur peaks does not have any direct relationship to the initial porosity. Figure 4.9 shows the lack of a direct relationship between the rate of damage front progression to the initial porosity. The figure also shows that with the increase in porosity, rate of damage

progression increases initially and then it starts to decrease. Thus an upper limit on the rate of damage progression can be found for a particular exposure condition and for a range of porosity values that a structure can have due to uncertainties arising from various sources. This limit can be estimated by performing numerical simulations for use in designing a structure for a particular purpose.

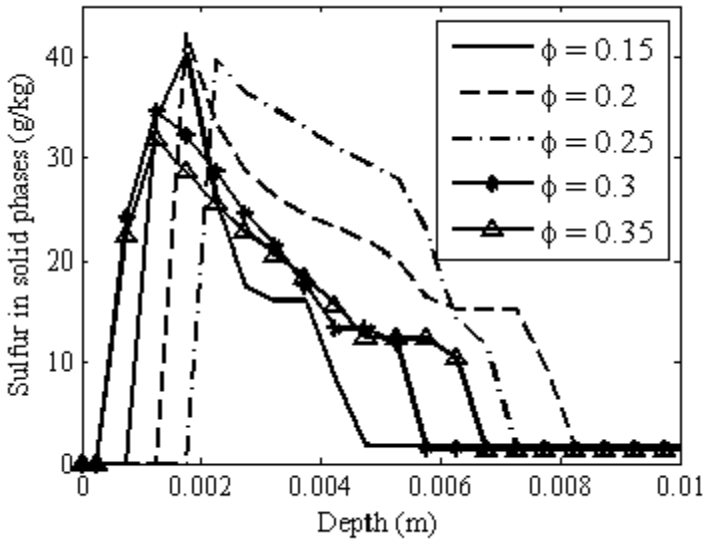

Figure 4.8 : Effect of initial porosity on sulfur profiles after 2 years of simulated immersion.

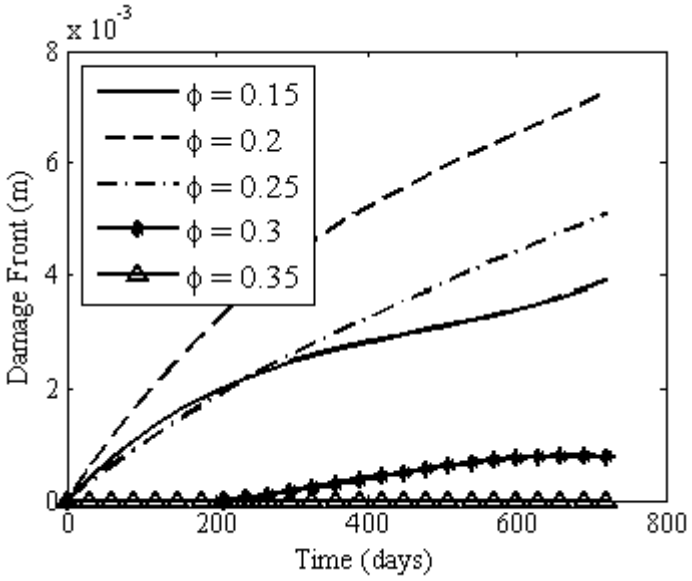

Figure 4.9 : Effect of initial porosity on rate of damage front progression after 2 years of simulated immersion.

4.2.5 Available fraction of porosity

As mentioned before, strain starts to develop once the pore volume is partly or completely filled. The fraction of the pore volume which is available for solid product deposition (*b*) before strain starts to develop is a model parameter that depends on the shape of the solid deposited and the pore size distribution of the structure. Numerical simulations are performed for 30%, 40%, 50%, 60% and 70% of initial porosity to evaluate the effect of the factor on the behavior of the specimen after 2 years. Increase in available porosity increases the amount of solid that must be deposited before strain can develop. Thus, an increase in *b* delays the initiation and progression of cracking. Figure 4.10 shows the rate of damage front progression with increasing *b*. It is evident from the figure that the structure experiences more damage if the available pore space is less. As

damage increases, diffusion of ions in and out of the structure also increases leading to faster damage as shown in Figure 4.10.

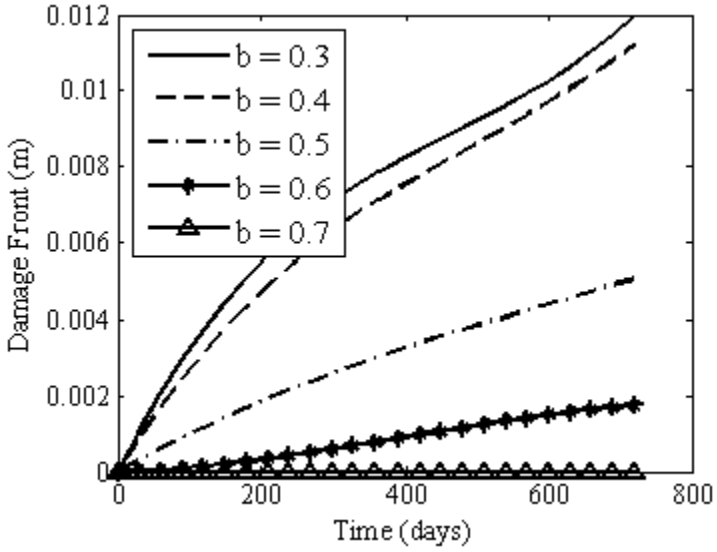

Figure 4.10 : Effect of available fraction of porosity on rate of damage front progression after 2 years of simulated immersion.

4.2.6 Initial tortuosity

Tortuosity is defined as the ratio of the length of the actual path between two points travelled by species to the linear distance between them. Diffusion of ions will take longer if the structure has a higher tortuosity value. This results in faster damage accumulation for less tortuous structures and a higher rate of strength loss as shown in Figure 4.11. A structure with a low water-cement ratio has a higher tortuosity value that results in a slower diffusion rate and a slower rate of damage progression, thus making it preferable to a structure with a high water-cement ratio.

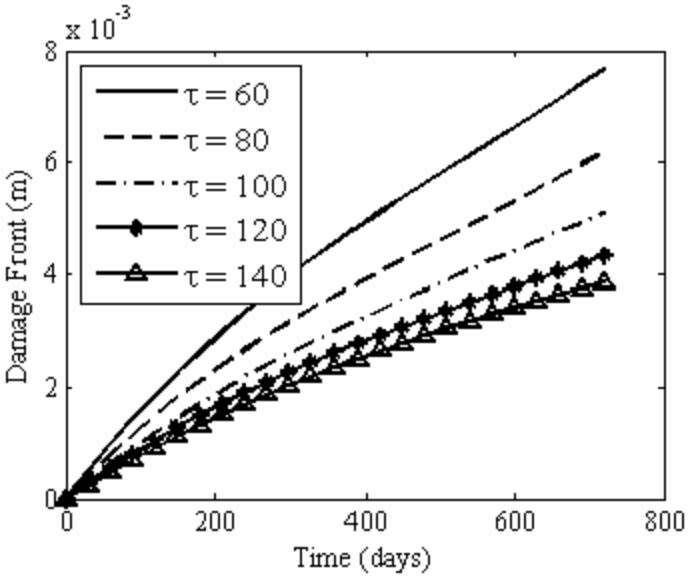

Figure 4.11 : Effect of initial tortuosity on rate of damage front progression after 2 years of simulated immersion.

4.2.7 Cement type

Type I cement is commonly used in construction whereas if the structure can be potentially exposed to sulfate solutions, Type V cement or a sulfate resistant cement is used. The compositions of the cements used in the simulation are taken from Al-Dulaijan *et al.* [32]. Table 4.1 shows the initial solid compositions for the two cement types as calculated using the chemical reaction module. It is important to note that the use of different cements result in different material characteristics e.g. porosity and tortuosity. But in the numerical simulations all the parameters (e.g., porosity and tortuosity) are kept at their base values as the effect of only cement composition on the damage progression is of interest in this subsection.

Table 4.1 : Comparison of initial solid phases.

Solid phases	Type I (moles/m^3)	Type V (moles/m^3)
Portlandite	1.19×10^3	1.18×10^3
Ettringite	29.27	27.34
Hydrogarnet	1.57×10^2	1.08×10^2
Tobermorite-II	1.56×10^2	1.67×10^2
Jennite	9.97×10^2	1.07×10^3
Fe-Hydrogarnet	80.33	89.57
Brucite	1.77×10^2	1.85×10^2

Figure 4.12 shows the concentration profiles of ettringite and gypsum in Type I and V cements. The amount of ettringite formed in Type I cement is more than that in Type V cement. However the progression of the damage front is dependent on the amount of gypsum formed, which is similar for both the cements and the position of gypsum fronts, which are almost coincident, as shown in Figures 4.12 and 4.13. The behavior of the two types of cements is not significantly different in this particular exposure condition. Thus it can be concluded that the Type V cement which is expected to be more sulfate resistant than Type I in a sulfate rich environment, is not necessarily more efficient in a particular exposure condition. Thus the numerical simulations can be used in assessing the behavior of a particular structure that may not be apparent from common sense for a given exposure condition.

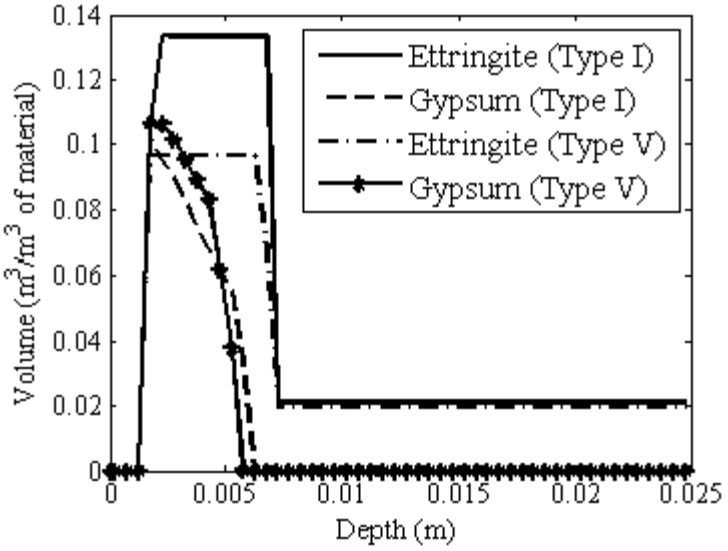

Figure 4.12 : Effect of cement type on ettringite and gypsum profiles after 2 years of simulated immersion.

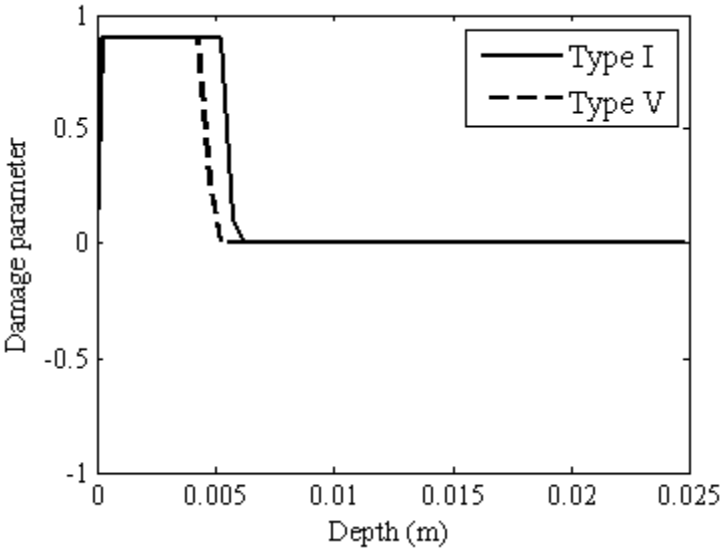

Figure 4.13 : Effect of cement type on damage progression after 2 years of simulated immersion.

As mentioned before, the sulfate concentration in the saltstone pore solution is considered to be significant (24000 mg/L). The sulfate concentration chosen for

illustration purposes in this chapter (35000 mg/L) is even higher than that in the saltstone. Thus the extent of damage observed here is high even in the case of sulfate resistant cement. But the damage will be less for a structure in a moderate to high sulfate environment than that predicted in the example here.

4.3 Conclusions

Sensitivity analyses are performed using the numerical model developed in this dissertation to evaluate the effects of various factors on the mineralogical features and the progression of damage. It is found that the effect of the relative rates of sulfate ingress and calcium leaching on damage is most significant. The relation between some external/internal factors and the damage progression rate is observed to be mostly nonlinear. The results of the sensitivity analysis provide quantitative information on the mineralogical features and damage state of the structure. After validating the model across a broader range of materials and experiments, the results of the sensitivity analysis can be used for design and life cycle management decision making.

CHAPTER V

UNCERTAINTY QUANTIFICATION OF A GEOCHEMICAL SPECIATION MODEL FOR CEMENTITIOUS MATERIALS

5.1 Introduction

The numerical model developed in this research comprises of three essential components of degradation of cementitious materials under external sulfate attack – (1) diffusion of ions, (2) chemical reactions, and (3) structural damage accumulation. There are several input and model parameters in each component of the model (e.g. porosity, tortuosity, equilibrium constants, Young's modulus etc.) that have certain amounts of uncertainty associated with them leading to uncertainty in the model prediction. Additionally, there are various assumptions and approximations in each component of the model that add to the overall uncertainty. Thus it is important to quantify uncertainty in different parts of the model so that the total uncertainty in the model prediction can be quantified. The focus of this chapter is to quantify uncertainty in the model parameters (i.e. the equilibrium constants) of the chemical equilibrium module (i.e. ORCHESTRA) using experimental results on the leaching behavior of cementitious materials as obtained from the LeachXS database [104]. It is important to note that the general methodology can also be applied for uncertainty quantification of the other two components provided that the experimental results of (1) the diffusion of nonreactive ions (to isolate it from the other components) and (2) the structural damage accumulation (cannot be isolated) are available for a particular material.

Simulation of the chemical equilibrium requires (1) thermodynamic information of

the potential chemical reactions that are generally obtained from the literature, which vary considerably across the available databases [105-109]; and (2) total availability of the species that can be obtained from the experiments. The thermodynamic constants are generally determined in the laboratory under controlled conditions. But the mineralogical behavior of the cementitious materials under field conditions can be considerably different from that observed in the laboratory environment and experimental results have inherent uncertainty. Additionally, the material characteristics have inherent variability that contribute to the overall uncertainty in the numerical simulation. Also, there are several assumptions and approximations in the model (e.g. local equilibrium assumption and ignoring the kinetic component of the reactions) that increase the uncertainty in the model predictions. Therefore it is important to quantify uncertainty in the model parameters of the chemical equilibrium module. This is performed in this chapter by calibrating the model parameters (i.e. the equilibrium constants of the checmical reactions) using experimental results incorporating various sources of uncertainty in the input parameters and experimental errors. The application of the framework is demonstrated using experimental data on the leaching behavior of a cement mortar sample and a concrete sample.

5.2 Numerical Simulation Framework

A numerical model essentially represents a set of mathematical equations that need to be solved to determine the response of a system under certain conditions. The set of equations may contain several unknown coefficients that are referred to as model parameters. Figure 5.1 shows the numerical model expressed as $G(\theta, s)$ where θ is an

array of model parameters and s is an array of inputs, and an array or a matrix of output variables, y. For example, the solution of a set of coupled diffusion equations provides concentrations (y) of one or more species in space and time. Here, the model parameters are the diffusion coefficients of the species (θ) and input parameters (s) are the concentrations of the species at the boundaries and/or at time $t = 0$. y is a one dimensional array if the solution comprises of concentrations of one species at the end of the simulation in space only; it is a two dimensional array if the solution comprises of the concentrations of one species over space and time; and it is a multidimensional array if the solution gives the concentrations of more than one species over space and time. If experimental observations are available (d), the model can be calibrated to obtain information about the unobservable model parameters, θ.

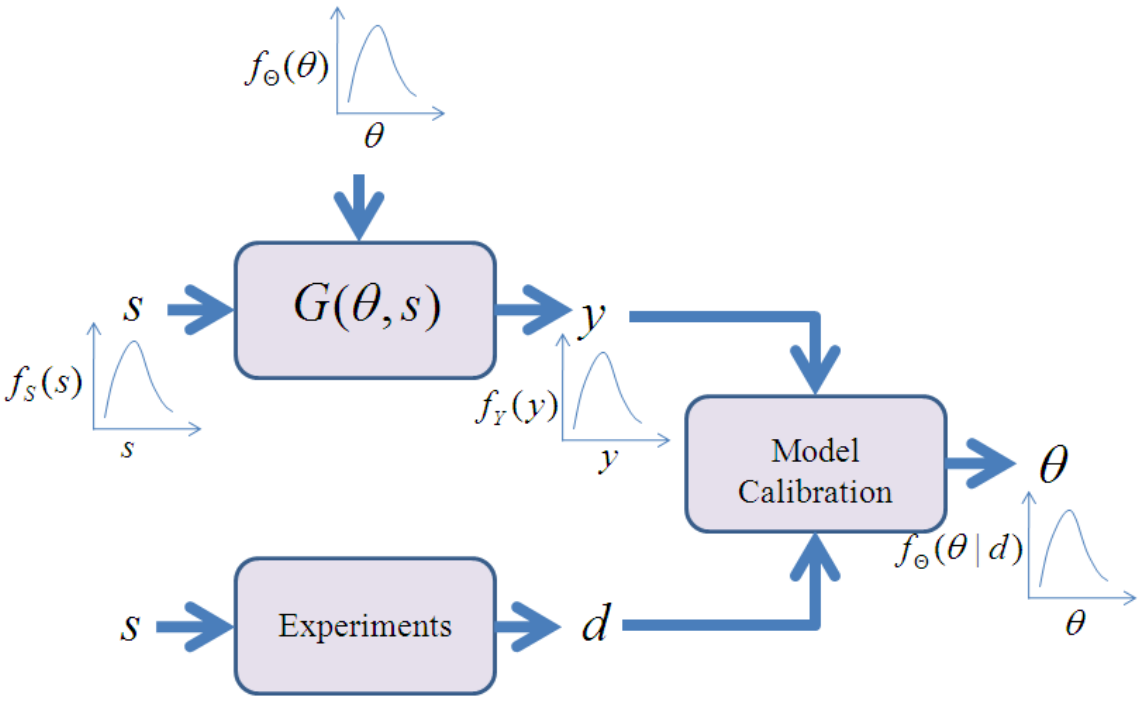

Figure 5.1 : Model calibration framework.

There are mainly three ways of calibrating a model – (1) a least squares method where the sum of the squared errors is minimized assuming that the input parameters are deterministic or the errors associated with the inputs are negligible, (2) maximum likelihood estimation where the probability of observing the model parameters is maximized assuming that the input parameters are deterministic and the associated errors are negligible, and (3) Bayesian method where the input parameters can be treated as random variables and the errors associated with the observations can also be treated as random variables. The Bayesian model calibration method is adopted in this research due to its simplicity, flexibility and ease of use.

The Bayesian calibration method is based on Bayes' theorem [110] expressed as

$$f(\theta|d) = \frac{f(\theta)f(d|\theta)}{\int f(\theta)f(d|\theta)d\theta} \tag{49}$$

where θ and d are the calibration parameters and the experimental observations respectively where θ and d can be scalars or vectors, $f(\theta|d)$ is the probability of observing θ given d (also known as posterior distribution of θ), $f(\theta)$ is the prior knowledge of θ which may be extremely poor (also known as prior distribution of θ) and $f(d|\theta)$ is the probability of observing d given θ (also termed as the Likelihood function of θ i.e. $L(\theta)$). The relation between the experimental observations and the model response is expressed as

$$d = G(\theta, s) + \varepsilon \tag{50}$$

where ε is the overall error due to both error in experimental observations and various assumptions and approximations made during the modeling process. ε is generally

assumed to have a normal distribution with zero mean and a variance σ^2 where the variance could be assumed or given. The likelihood function, $L(\theta)$, is expressed as

$$L(\theta) = f(d|\theta) = \frac{1}{\sqrt{2\pi}\sigma} \exp\left[-\frac{(d - G(\theta, s))^2}{2\sigma^2}\right] \tag{51}$$

For a multivariate model output, Eq. (50) transforms into

$$d_i = G(\theta, s) + \varepsilon_i \tag{52}$$

where d_i is a multi-element array of observations of i^{th} observable parameter and ε_i is the corresponding error array. The likelihood function is then given by

$$L(\theta) = \prod_{i=1}^{n} f(d_i|\theta) \tag{53}$$

The process of evaluating the posterior distribution from Eq. (49), $f(\theta|d)$, becomes challenging if the model is a computer code where no analytical form is available for $f(\theta|d)$. This has been one of the biggest challenges in implementing Bayesian method in parameter updating [111]. In such cases, the Markov Chain Monte Carlo sampling method is used to generate the posterior distributions of the parameters. It is important to note that the denominator on the right hand side of Eq. (49) is a constant and therefore the expression reduces to

$$f(\theta|d) \propto f(\theta) f(d|\theta) \tag{54}$$

The method of generating samples from a complex and often unknown distribution as given in Eq. (54) by Markov Chain Monte Carlo method is described in the next section.

5.3 Markov Chain Monte Carlo Simulation

The focus of this section is to describe a method for constructing an arbitrary distribution $\pi(X)$, by drawing samples from it e.g. Eq. (54) (i.e. $\pi(X) = f(\theta) f(d|\theta)$). In

this respect, the Markov Chain Monte Carlo method provides an easy way of solving this problem. In any time dependent process, the state of the system at time t is dependent on the previous states up to time $t-1$. The basic characteristic of a Markov process is that the state of a system at the current time is only dependent on the previous time step. There are several algorithms available for generating samples from an unknown distribution using the concept of a Markov process e.g. Metropolis algorithm [112], Metropolis-Hastings algorithm [113], Gibbs sampling [114], adaptive Metropolis algorithm [115], delayed rejection method [116] etc. In this research, the adaptive Metropolis algorithm combined with delayed rejection method is used for calibrating the model parameters.

In the original Metropolis algorithm [112], samples are generated from a symmetric proposal distribution, $q(X)$ such as uniform, normal, symmetric triangular etc. If $q(X)$ is a multivariate distribution, the components of X can be generated sequentially (this is known as the *single component* Metropolis algorithm) or all of them together (this is known as the *random walk* Metropolis algorithm) [117]. The general framework of the Metropolis algorithm which can be assumed to be a special case of the more general Metropolis-Hastings algorithm [113] is shown in Figure 5.2.

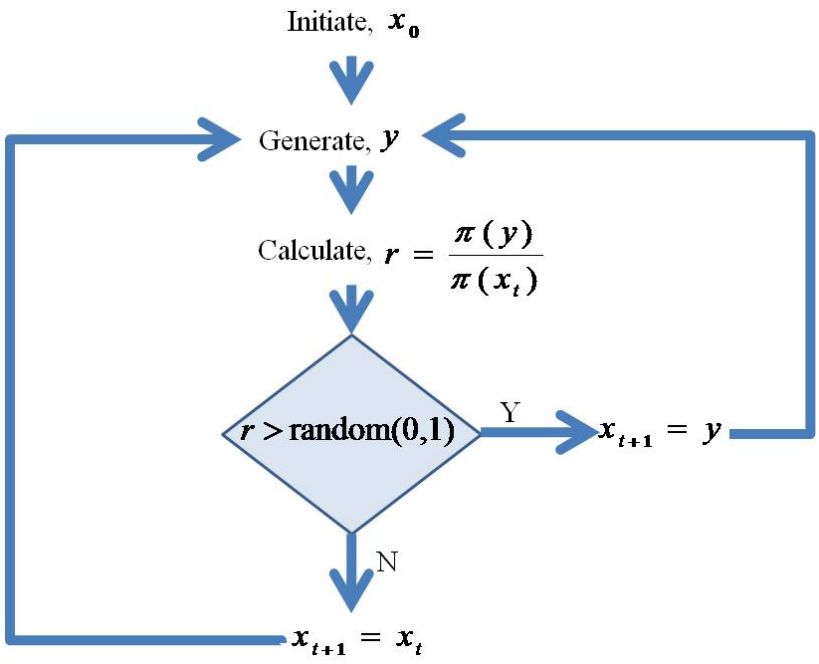

Figure 5.2 : General framework of Metropolis algorithm.

The algorithm is initialized with a sample, x_t at $t = 0$. Then, the next sample, y, is generated from a symmetric proposal distribution, $q(y|x_t)$, centered at the current state. The following expression is evaluated for the candidate sample

$$r(x_t, y) = \frac{\pi(y)q(y|x_t)}{\pi(x_t)q(x_t|y)} \tag{55}$$

with the condition that the proposal distribution be symmetric, i.e. $q(y|x_t) = q(x_t|y)$. The sample, y, is accepted if the ratio, $r(x_t, y) > 1$. If $r(x_t, y) < 1$, the sample is accepted with probability $r(x_t, y)$. The method for imposing this condition is to generate a random sample,α, from a uniform distribution between 0 and 1 and if $r(x_t, y) > \alpha$, then the sample is accepted and if $r(x_t, y) < \alpha$, the sample is rejected and the process is repeated till sufficient number of samples are obtained.

The most common ways of checking the efficiency of the algorithm are by visually inspecting the trace plot of the samples i.e. generated samples plotted against the number of iterations and the plot of statistical parameters against the number of iterations. The distribution constructed from the generated samples is said to have converged to the target distribution if the samples manifest stationary behavior, i.e. have a constant mean and a constant standard deviation.

The two most important aspects of efficiently executing the algorithm are a good initial value and a good proposal distribution. The most commonly used proposal distribution for Metropolis algorithm is a normal distribution with mean at the current sample point and an assumed variance. Rigorous manual tuning is often needed for finding an optimum variance [117] so that the algorithm performs efficiently. There are several methods proposed in the literature that offer efficient sampling techniques to optimize the performance of the algorithm, e.g. adaptive direction sampling [118], adaptive Metropolis algorithm [115], adaptive Random Walk method [119], delayed rejection method [120]. The adaptive Metropolis algorithm combined with the delayed rejection method [121] is used in this research to circumvent the problem of manual tuning of the proposal distribution. The general methodology for generating samples from an unknown target distribution is the same as shown in Figure 5.2 with the modifications being applied for generating the candidate samples using the algorithms. The methods are described in the following subsections.

5.3.1 Adaptive Metropolis algorithm

In the adaptive Metropolis algorithm the proposal distribution adapts itself automatically using the samples generated during the sampling process. Sample generation and acceptance/rejection are first performed as in the original Metropolis algorithm for a certain number of iterations (t_0) decided by the analyst. Then, the samples are generated from a k dimensional Gaussian proposal distribution, $N(x_t, C_t)$ with mean x_t and covariance C_t calculated as

$$C_t = \begin{cases} C_0 & t \leq t_0 \\ s_d cov(x_0, x_1, \ldots., x_{t-1}) + s_d \epsilon I_k & t > t_0 \end{cases} \quad (56)$$

where C_0 is the initial covariance matrix, s_d is a scaling parameter which is taken to be $2.4^2/k$ [115, 122] as this value is shown to optimize the performance of Metropolis algorithm for Gaussian targets and Gaussian proposals, ϵ is a very small positive number that prevents the covariance from being zero (in case of rejection of all samples) and I_k is a k dimensional identity matrix. The steps for calculation of the acceptance ratio and the scheme following which the samples are accepted or rejected are the same as in the original Metropolis algorithm as shown in Figure 5.2. This scheme can be applied both in single component and in random walk (i.e. sequential and simultaneous sample generation for multi dimensional problems) methods of sample generation. The single component adaptive Metropolis scheme is used in Subsection 5.4.1 for calibration of the model parameters. It is shown in the subsection that the algorithm performed better than the basic Metropolis algorithm by inspecting the trace plot of the samples. But it takes considerable computational time for high dimensional problems (> 15) as considered in this research.

The random walk Metropolis algorithm is faster than the single component Metropolis algorithm. N number of samples (accepted + rejected) are generated in N steps in the random walk scheme whereas the same number of samples are generated in $N \times k$ steps in the single component scheme for k dimensional problems. As mentioned before, the performance of the algorithm, i.e. the acceptance rate, is dependent upon the optimum choice of the proposal distribution. The adaptive Metropolis algorithm as described in this subsection circumvents the problem of manual selection of proposal distribution by adapting automatically using a certain number of generated samples. But this method is useful only when at least some samples can be generated from the untuned proposal distribution. In this respect, choosing a multivariate proposal distribution is more challenging for the random walk scheme than the single component scheme. Thus the delayed rejection scheme is used in conjunction with the adaptive Metropolis method in Subsection 5.4.2 to further enhance the performance of the random walk scheme as well as gain computational speed. The delayed rejection method is described in the next subsection.

5.3.2 Delayed rejection method

The basic strategy of the delayed rejection method is that if the newly generated sample is rejected, instead of staying at the previous sample point, a second stage proposal distribution is used for generation of the next sample. This process can be repeated as many times as desired. Following is a description of a n stage delayed rejection method.

Let the first stage proposal distribution be $q_1(y_1|x_t)$ that is symmetric and centered at the previous sample x_t. The probability with which the sample is accepted is expressed as

$$r_1(x_t, y_1) = \min\left(1, \frac{\pi(y_1)q_1(y_1|x_t)}{\pi(x_t)q_1(x_t|y_1)}\right) \tag{57}$$

that is similar to Eq. (55). If the sample is rejected, another sample, y_2 is generated from a second stage proposal distribution, $q_2(y_2|x_t, y_1)$. The acceptance ratio is calculated as

$$r_2(x_t, y_1, y_2) = \min\left(1, \frac{\pi(y_2)q_1(y_2|y_1)q_2(y_2|y_1, x_t)[1 - r_1(y_2, y_1)]}{\pi(x_t)q_1(x_t|y_1)q_2(x_t|y_1, y_2)[1 - r_1(x_t, y_1)]}\right) \tag{58}$$

Similarly, the n-th stage acceptance ratio is calculated as

$$\begin{aligned} & r_n(x_t, y_1, y_2, \ldots., y_n) \\ = \min\Bigg(1, & \frac{\pi(y_n)q_1(y_n|y_{n-1})q_2(y_n|y_{n-1}, y_{n-2}) \ldots q_n(y_n|y_{n-1}, \ldots, x_t)}{\pi(x_t)q_1(x_t|y_1)q_2(x_t|y_1, y_2) \ldots q_n(x_t|y_1, y_2, \ldots, y_n)} \\ & \frac{[1 - r_1(y_n, y_{n-1})][1 - r_2(y_n, y_{n-1}, y_{n-2})] \ldots [1 - r_{n-1}(y_n, \ldots, y_1]}{[1 - r_1(x_t, y_1)][1 - r_2(x_t, y_1, y_2)] \ldots [1 - r_{n-1}(x_t, y_1, \ldots, y_{n-1})]}\Bigg) \end{aligned} \tag{59}$$

Following Haario *et al.* [121], the first stage proposal distribution can be assumed to be a multivariate normal distribution $N(x_t, C_t)$ where C_t is the covariance matrix as defined in Eq. (56) and the proposal distributions in the following stages can be assumed to be a multivariate normal distribution $N(x_t, C_t')$ where $C_t' = \gamma C_t$ and γ is any positive number less than 1. Haario *et al.* [121] assumed γ to be 0.01 for a two stage delayed rejection adaptive Metropolis method. The acceptance/rejection scheme of generated samples is the same as that in the basic Metropolis algorithm as shown in Figure 5.2.

The adaptive Metropolis and delayed rejection adaptive Metropolis schemes are implemented in MATLAB in conjunction with ORCHESTRA. The approximate computational time required for executing single component and a three stage delayed rejection adaptive Metropolis algorithm to generate 10000 samples of 18 parameters are

11 days and 1.5-3.5 days respectively in a 8 processor windows computer. The model parameters of the chemical equilibrium module are calibrated for a cement mortar and a concrete sample, and the results are shown in the next section. Also, the calibration results are validated by comparing the model predictions for a similar concrete sample using the calibrated parameters with the experimental results.

5.4 Numerical Simulation

For the purpose of demonstration, experimental data on the leaching behavior of the cement-based samples are obtained from the LeachXS database [67]. The experimental data comprises of the leached concentrations of the species (e.g. Ca^{+2}, Na^{+} etc.) for a particular sample at different pH values. The general description of the experiment is given in Subsection 2.3.2 in Chapter II. The inputs to the model are the initial total concentrations of the species and the pH of the solution in which the samples are immersed. The model calculates the solid-liquid equilibrium phases by assuming a set of minerals to be present in the system and predicts the total dissolved amounts of the species at different pH conditions. The equilibrium constants of the mineral phases are then calibrated using the methodology described in the previous section given the experimentally observed leached concentrations of the species. The simulation details and the results are given in the following subsections.

5.4.1 Cement mortar sample

The cement mortar sample used for the demonstration of the calibration framework is composed of CEM V/A 32.5 N cement mixed with 32% (by mass) granular blast furnace

slag and 20% (by mass) fly ash and 1:3 (by mass) cement to sand ratio with a water-cement ratio of 0.5 (by mass) subjected to pH dependence test [104]. The test data comprises of the concentrations of species leached in 24 h from a cementitious material with a liquid to solid ratio of 10 (liter/kg) at predetermined pH values [104]. The geochemical speciation code, ORCHESTRA [25] is used in this chapter to numerically model the leaching behavior of the material. The experimental data comprise of concentrations of 6 species (e.g. $Al, Ca, Fe\ Mg, Si$ and S) at 9 pH values (i.e. 3.50, 4.25, 6.70, 7.84, 9.28, 10.34, 11.37, 12.22 and 12.34). A set of 18 minerals are chosen after several preliminary trial runs that ensures a good initial guess for the calibration algorithm. The mineral set is given in Table 5.1. The equilibrium constants of the 18 minerals are the model parameters (θ) that are calibrated using the single component adaptive Metropolis algorithm as described before.

Table 5.1 : Mineral set chosen for calibration of equilibrium constants.

Mineral Phase	Expanded Formula	Common Name
$C_6A\bar{S}H_{32}$	$6CaO.Al_2O_3.32H_2O$	Ettringite
C_3AH_6	$3CaO.Al_2O_3.6H_2O$	Hydrogarnet
C_3FH_6	$3CaO.Fe_2O_3.6H_2O$	Fe-Hydrogarnet
C_2ASH_8	$2CaO.Al_2O_3.SiO_2.8H_2O$	Stratlingite
C_2FSH_8	$2CaO.Fe_2O_3.SiO_2.8H_2O$	Fe-Stratlingite
$C_{1.67}SH_{2.1}$	$1.67CaO.SiO_2.2.1H_2O$	Jennite
CH	$CaO.H_2O$	Portlandite
$C\bar{S}H_2$	$CaO.SO_3.2H_2O$	Gypsum
$Al(OH)_3$ (amorphous)	-	Gibbsite
$C_2S_{2.4}H_{3.2}$	$2CaO.2.4SiO_2.3.2H_2O$	Tobermorite-I
$Fe(OH)_3$ (microcrystalline)	-	Ferric Hydroxide
$C_6F\bar{S}H_{32}$	$6CaO.Fe_2O_3.32H_2O$	Fe-Ettringite
$Mg(OH)_2$	-	Brucite
$NaAlSi_3O_8$	-	Analbite
$CaO.CO_2$	-	Calcite
C_2FH_8	$2CaO.Fe_2O_3.8H_2O$	-
M_4ACH_8	$4MgO.Al_2O_3.CO_2.8H_2O$	CO_3-Hydrotalcite
MC	$MgO.CO_2$	Magnesite

The input parameters of the model are the specified pH values and the total leachable concentrations of the species obtained from the LeachXS database. It is assumed that the total leachable concentrations are normally distributed with specified mean value and 10% coefficient of variation. The process of adjusting pH values by adding acid/base is very sensitive and difficult to control, specifically at lower and higher pH ranges. Thus the error associated to pH is assumed to have variable error structure expressed as

$$\varepsilon = \begin{cases} 0.2 & \text{if pH} < 4.5 \\ 0.1 & \text{if } 4.5 < \text{pH} < 10.5 \\ 0.2 & \text{if } 10.5 < \text{pH} < 13 \\ 0.3 & \text{if pH} > 13 \end{cases} \tag{60}$$

In this chapter, the errors associated with the pH values and the concentrations of the leached species are combined and ε_is in Eq. (52) are expressed as error envelopes as shown in Figure 5.3. As the experimental points have uncertainty along both the axes, the

error between the model prediction and the experimental data is calculated as the orthogonal distance between the experimental point and the model prediction curve instead of the conventional vertical distance between the data and the model prediction. It is important to acknowledge that this method of error estimation is one of the many ways that the error can be represented. Any other error scheme can also be employed in this framework. Henceforth, the particular error measure adopted in this dissertation will be referred as *orthogonal error*. Figure 5.3 shows the model response and experimental results for aluminum. It also shows the error envelopes associated with the experimental data and the orthogonal error between the experimental point and the model prediction curve. The prior distributions of the model parameters are assumed to be independent and normally distributed with the mean values obtained from the literature and 50% coefficient of variation. A large coefficient of variation is chosen so that the prior is not completely non-informative, it covers a large range of values, and puts more emphasis on the value obtained from the literature. The joint prior distribution of the independent model parameters can be expressed as the product of the prior distributions. Thus Eq. (54) transforms into

$$f(\theta|d) \propto \prod_{j=1}^{m} f(\theta_j) \prod_{i=1}^{n} f(d_i|\theta) \tag{61}$$

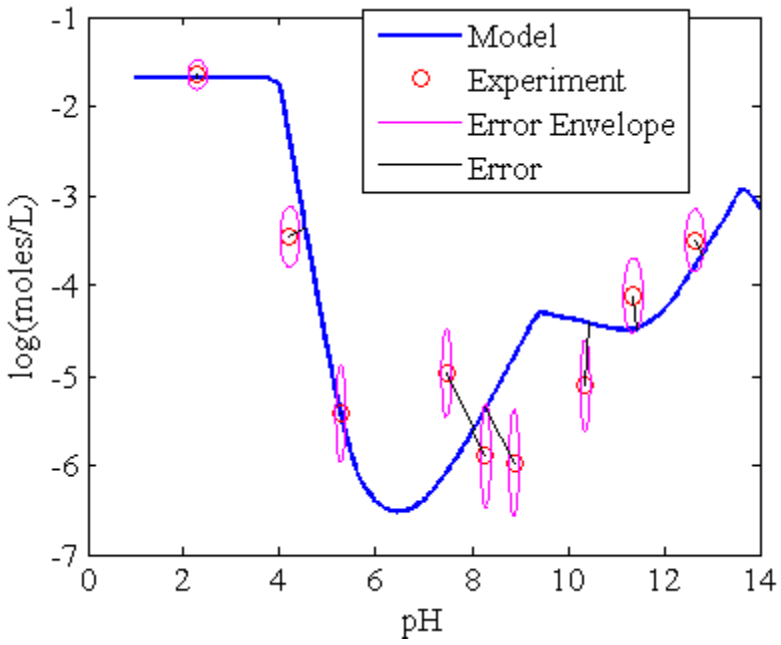

Figure 5.3 : Error envelope associated with the experimental data.

The applicability of the adaptive Metropolis algorithm is tested with a reduced problem where only 5 mineral phases are chosen from the 18 phases given in Table 5.1. Figures 5.4 and 5.5 show the trace plots of the samples generated using the basic single component Metropolis algorithm and the single component adaptive Metropolis algorithm respectively. It is evident from the plots that the single component adaptive Metropolis algorithm shows better mixing of samples and a satisfactory acceptance rate. Gelman *et al.* [122] showed that the acceptance rate asymptotically approaches 23% for basic Metropolis algorithm as the number of dimensions approaches infinity if the proposal distribution size is approximately similar to the target distribution.

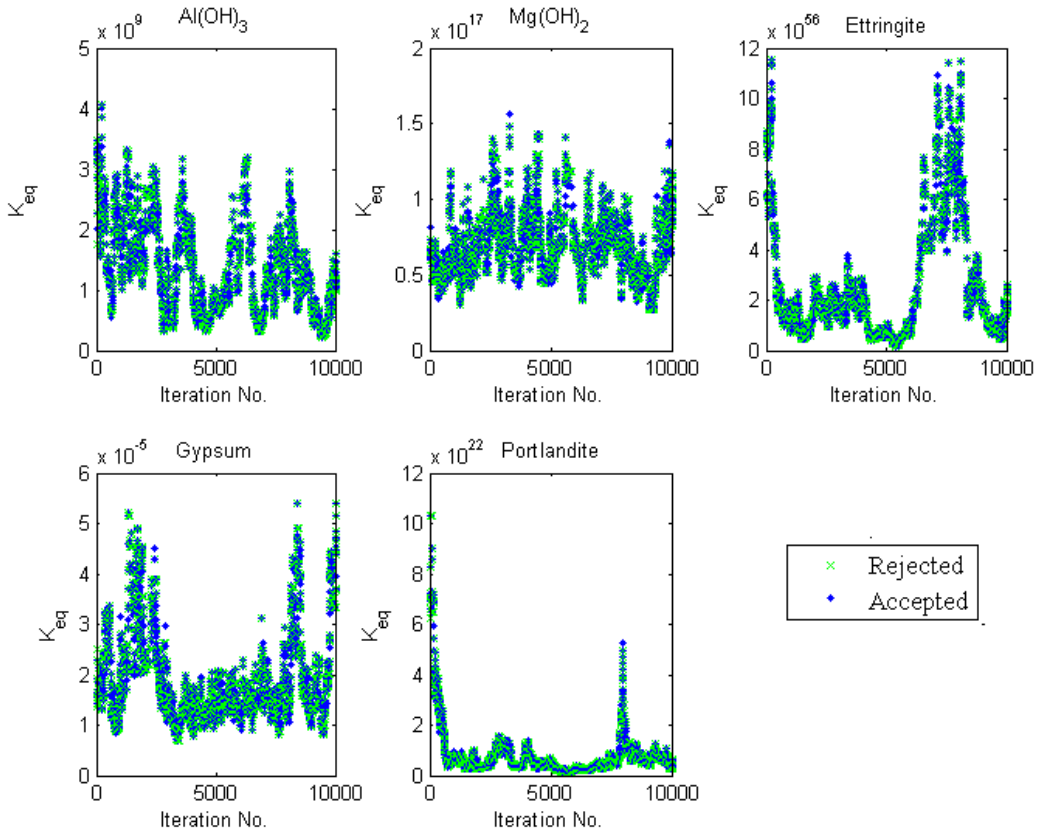

Figure 5.4 : Trace plot of samples using basic Metropolis algorithm – example of slow mixing.

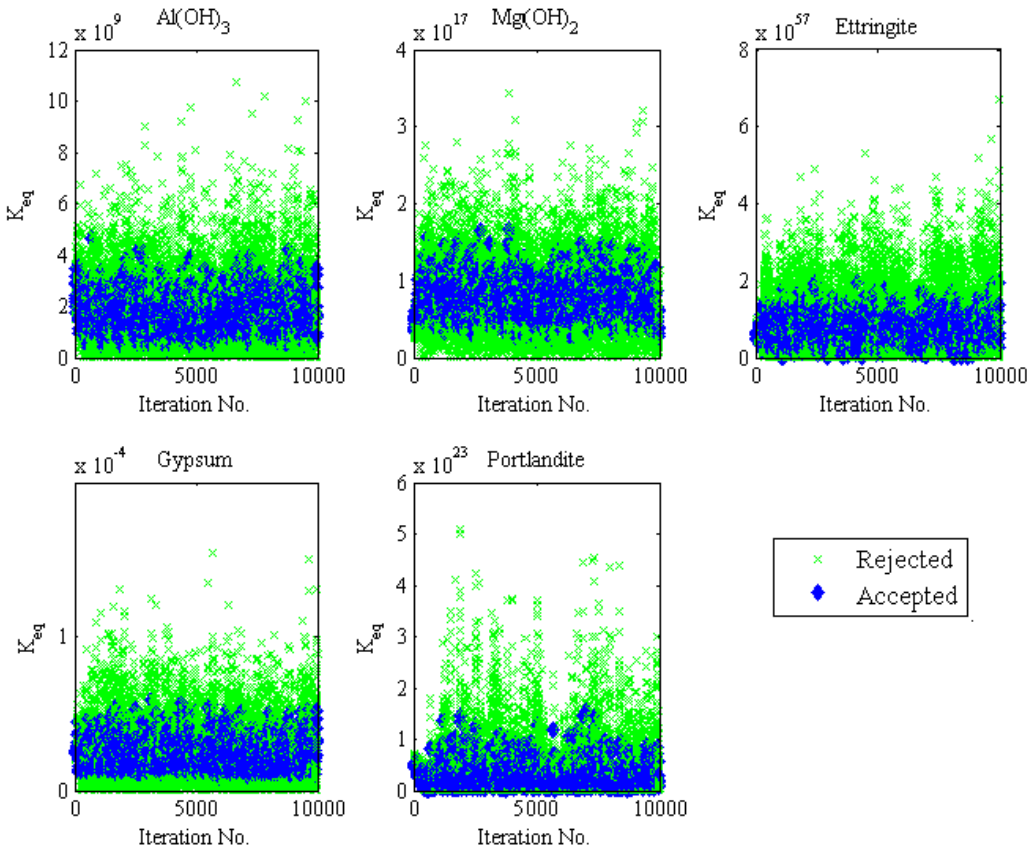

Figure 5.5 : Trace plot of samples using adaptive Metropolis algorithm – example of good mixing.

The full model calibration is performed with the single component adaptive Metropolis algorithm described in the previous section. Figure 5.6 shows the prior and the posterior distributions of the model parameters. 5000 Monte Carlo simulations are then performed using the posterior distributions of the model parameters with positivity constraints (as equilibrium constants are always positive) to obtain the best fit model response. The other input parameters are kept constant so that the best set of equilibrium constants can be obtained without the influence of the other uncertainties, and the results can be compared with the model responses using the prior mean values of the model parameters. Therefore, the error between the model prediction and the experimental data

is estimated as the vertical distance between the data and the model prediction curve. Figure 5.6 also shows the shift in the best fit model parameters from the values obtained from the literature i.e. the mean values of the prior distributions. Table 5.2 gives the prior mean values, the calibrated best fit values and the percentage shift in the parameters. The comparisons between the model predictions using the model parameters obtained from the literature, model predictions using the calibrated best fit model parameters, and the experimental data are shown in Figure 5.7.

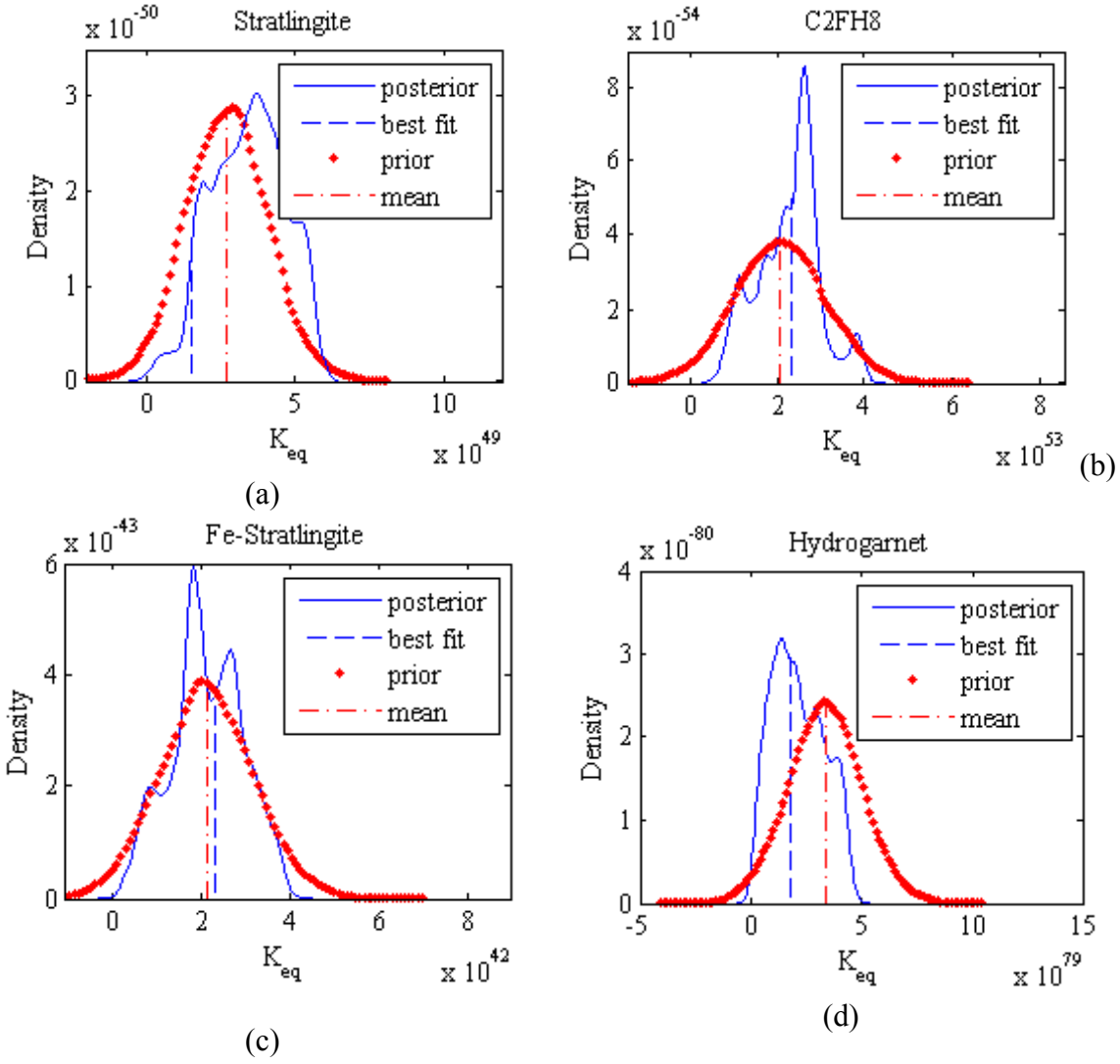

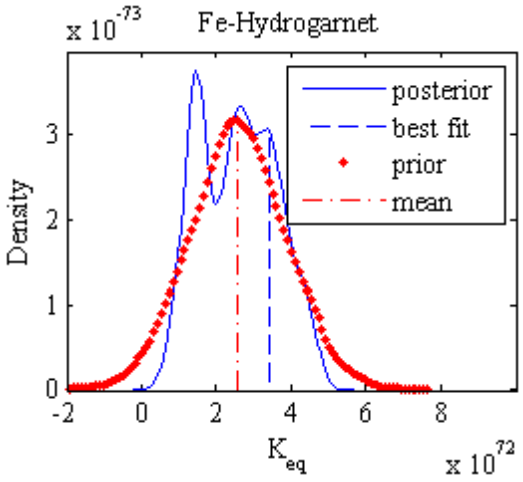

(e)

▪ EMBED PBrush

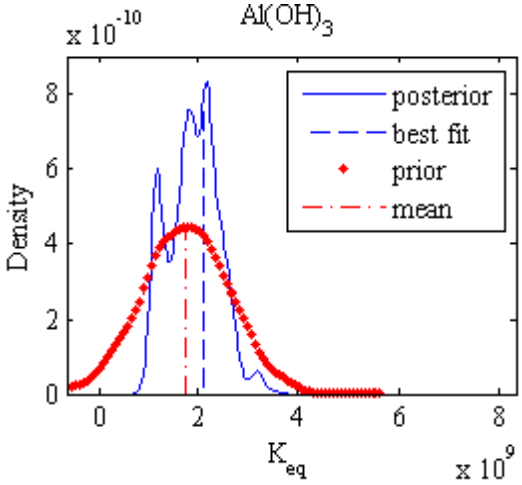

(f)

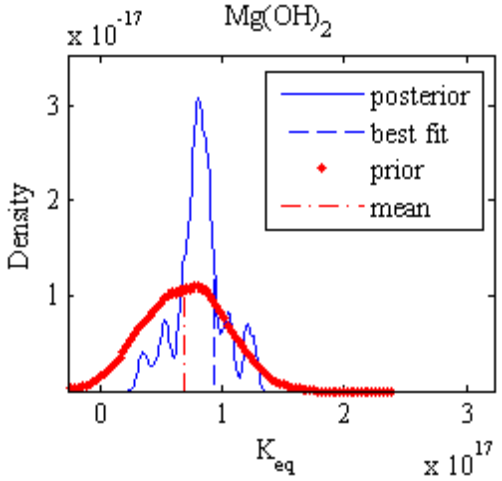

(g)

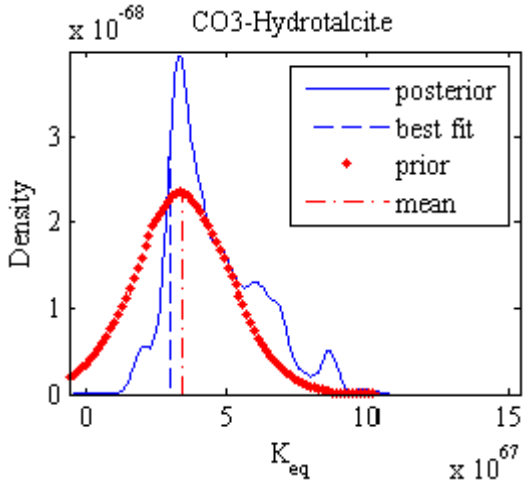

(h)

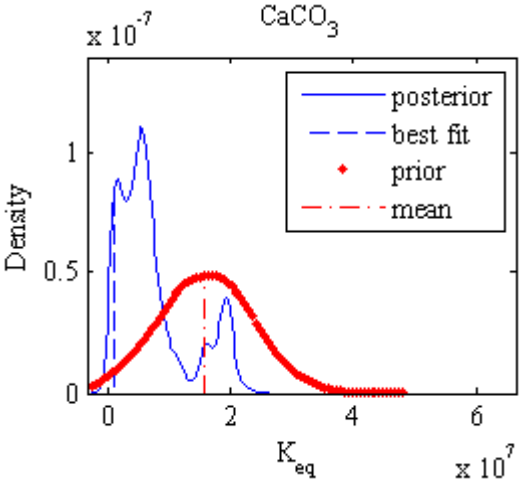

(i)

{ EMBED PBrush

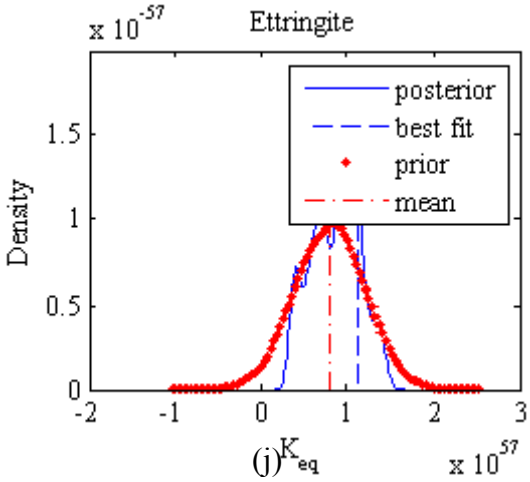

(j)

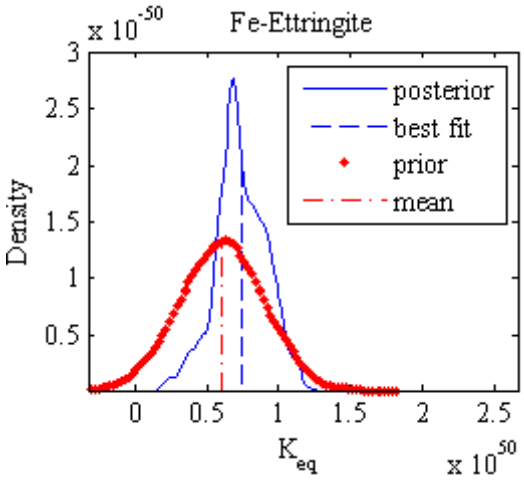
Fe-Ettringite
x 10^-50
Density
K_eq
x 10^50
posterior
best fit
prior
mean

(k)

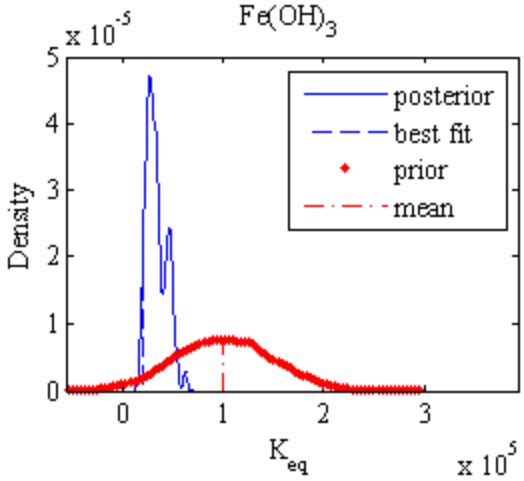
Fe(OH)3
x 10^-5
Density
K_eq
x 10^5
posterior
best fit
prior
mean

(l)

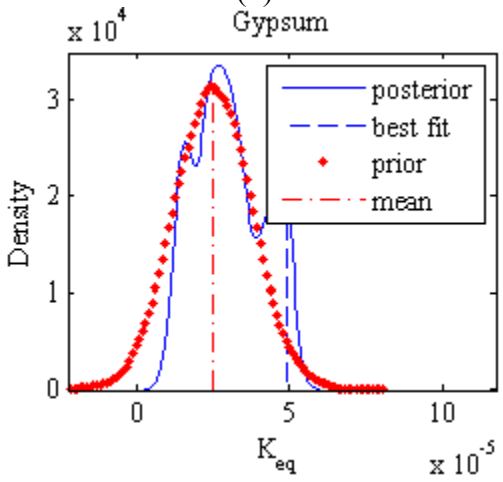
Gypsum
x 10^4
Density
K_eq
x 10^-5
posterior
best fit
prior
mean

(m)

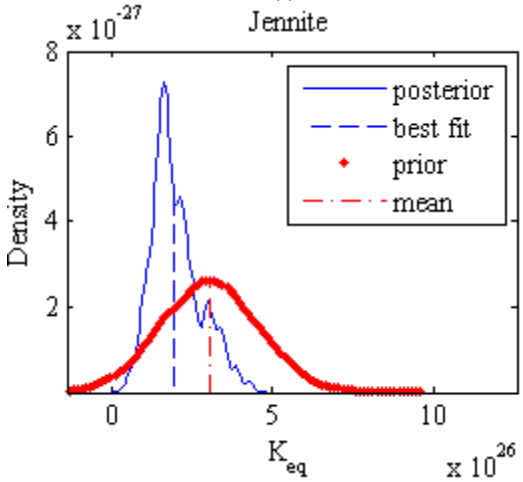
Jennite
x 10^-27
Density
K_eq
x 10^26
posterior
best fit
prior
mean

(n)

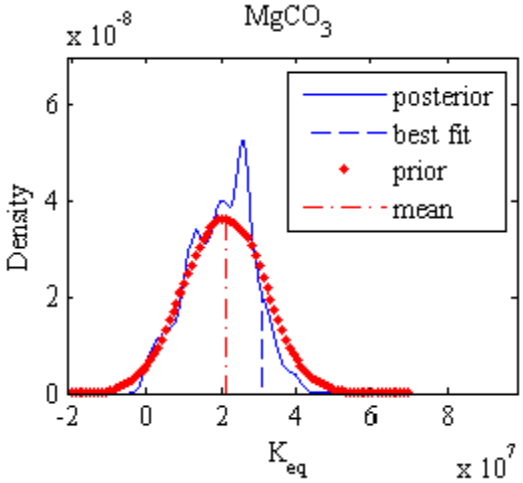
MgCO3
x 10^-8
Density
K_eq
x 10^7
posterior
best fit
prior
mean

(o)

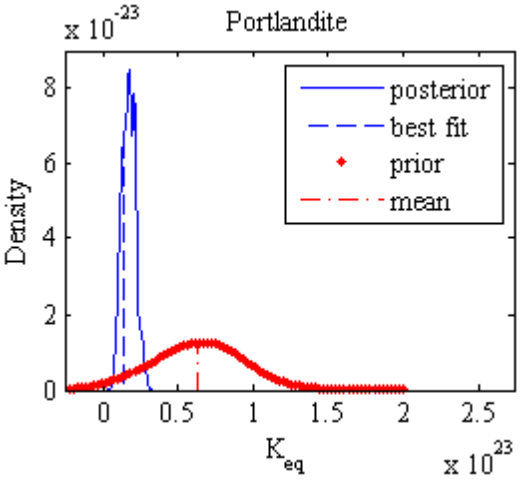
Portlandite
x 10^-23
Density
K_eq
x 10^23
posterior
best fit
prior
mean

(p)

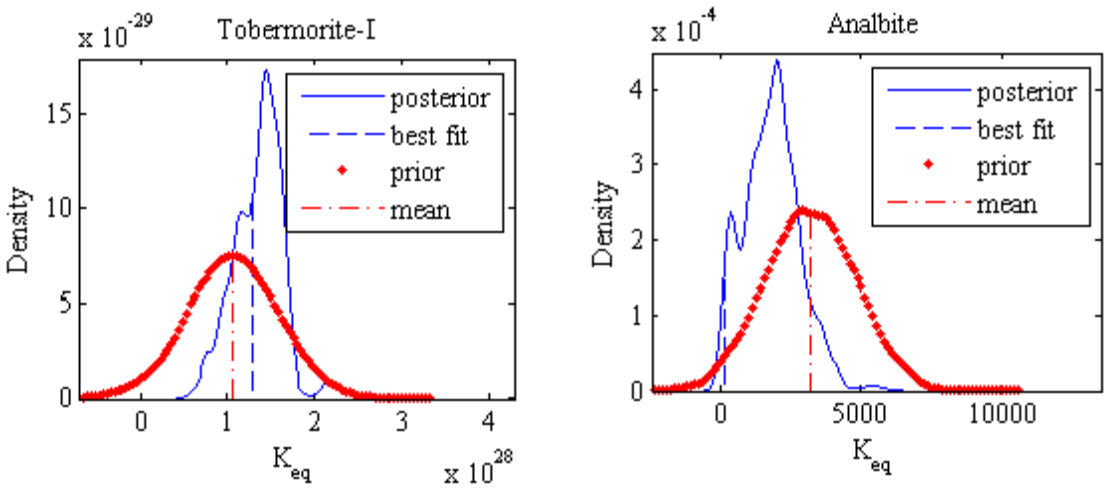

(q) (r)

Figure 5.6 : Prior and posterior distributions of the model parameters.

Table 5.2 : Model parameter values – prior mean vs. calibrated best fit.

Solid Phase	Prior Mean	Calibrated Best Fit	% Shift
Startlingite	2.74×10^{49}	2.56×10^{49}	6.45
C_2FH_8	2.07×10^{53}	4.51×10^{52}	78.19
Fe-Stratlingite	2.13×10^{42}	9.09×10^{41}	57.29
Hydrogarnet	3.40×10^{79}	7.75×10^{78}	77.24
Fe-Hydrogarnet	2.58×10^{72}	1.24×10^{72}	51.81
Gibbsite	1.75×10^{9}	1.48×10^{9}	15.37
Brucite	6.92×10^{16}	9.77×10^{16}	-41.22
CO_3-Hydrotalcite	3.41×10^{67}	2.68×10^{67}	21.60
Calcite	1.58×10^{7}	8.03×10^{6}	49.35
Ettringite	7.98×10^{56}	1.04×10^{57}	-30.53
Fe-Ettringite	6.05×10^{49}	5.48×10^{49}	9.53
Iron Hydroxide	1.00×10^{5}	7.89×10^{4}	21.10
Gypsum	2.51×10^{-5}	1.53×10^{-5}	39.25
Jennite	3.04×10^{26}	3.8×10^{25}	87.50
Magnesite	2.10×10^{7}	1.16×10^{6}	94.49
Portlandite	6.27×10^{22}	1.18×10^{22}	81.14
Tobermorite-I	1.07×10^{28}	1.46×10^{28}	-36.47
Analbite	3.21×10^{3}	4.22×10^{2}	86.84

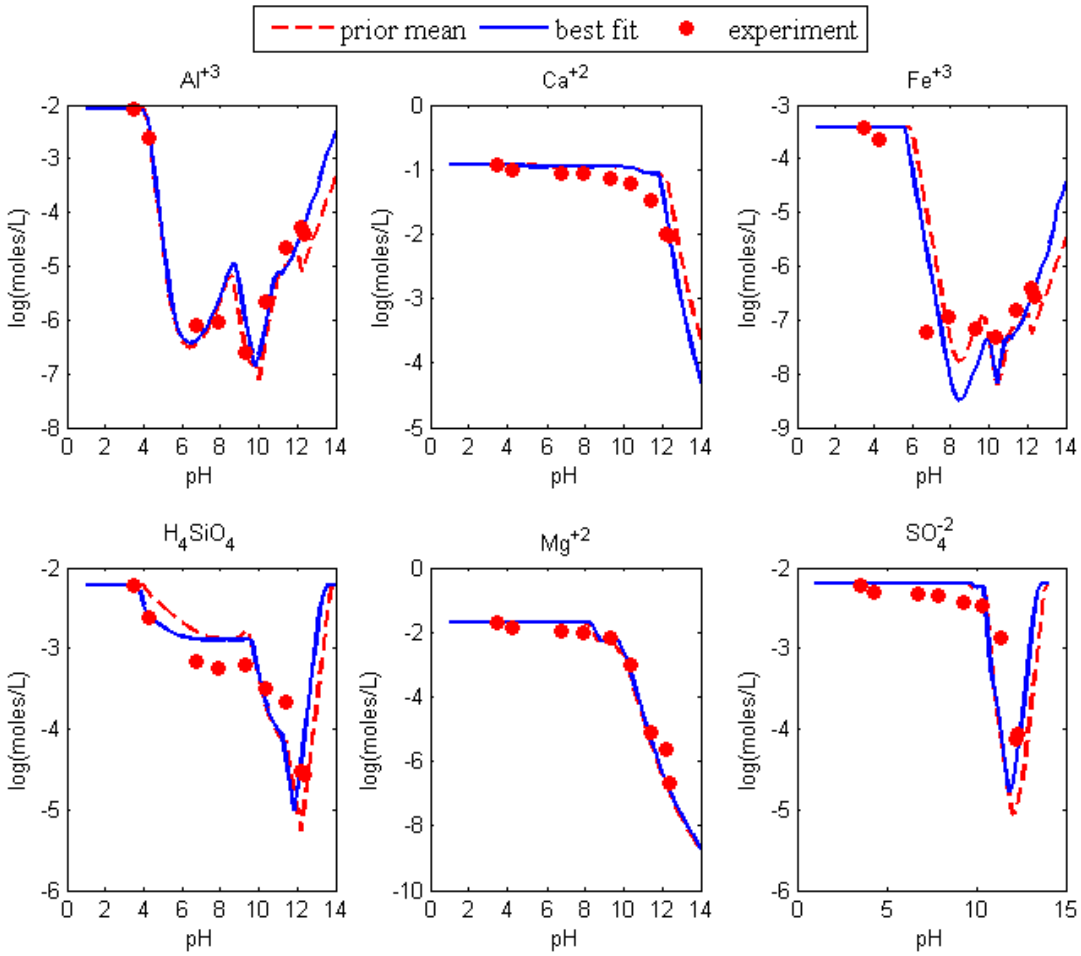

Figure 5.7 : Comparison of model responses using the best fit and the prior mean model parameters with the experimental results.

The errors for each species using the prior mean values and the calibrated best fit values are shown in Figure 5.8. It is evident from the figure that the errors after calibration in all the species are less than the errors obtained using the prior mean values for the model parameters.

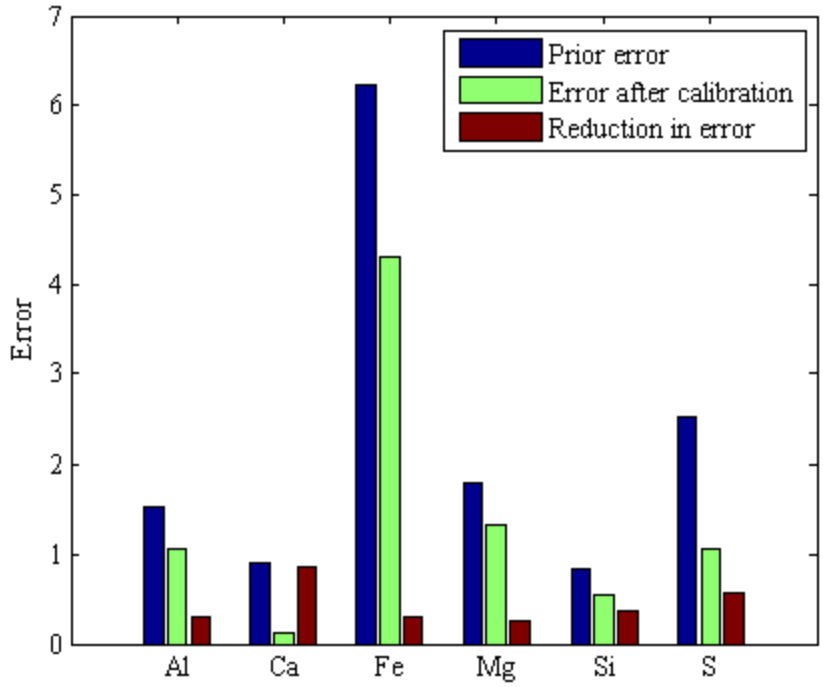

Figure 5.8 : Errors in model responses using prior mean and calibrated best fit model parameters.

The shifts in the best fit model parameters from the prior mean values are essentially due to the shifts in the precipitation domains of the minerals. Figure 5.9 shows the changes in the mineral precipitation domains using the prior mean values and the calibrated best fit values. The most noticeable features in the plots are:

(i) Figures 5.9a and b – Stratlingite, Hydrogarnet and Ettringite have changed their domains of precipitation.

(ii) Figures 5.9c and d – Gypsum precipitation domain has increased.

(iii) Figures 5.9e and f – Fe-Ettringite, Fe-Hydrogarnet and Fe-Stratlingite have changed their domains of precipitation.

(iv) Figures 5.9g and h – Magnesite has precipitated in the simulation with the best fit calibrated values.

(v) Figures 5.9i and j – Stratlingite, Jennite and Tobermorite-I have changed their domains of precipitation.

(vi) Figures 5.9k and l – All the minerals have changed their domains of precipitation, but the most prominent of all is gypsum precipitation in the simulation using best fit calibrated values.

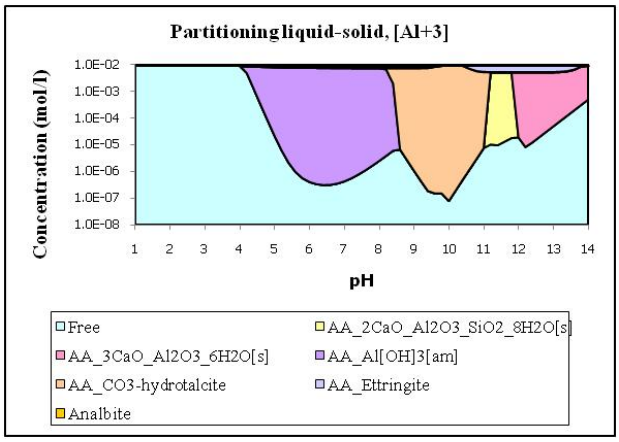

(a)

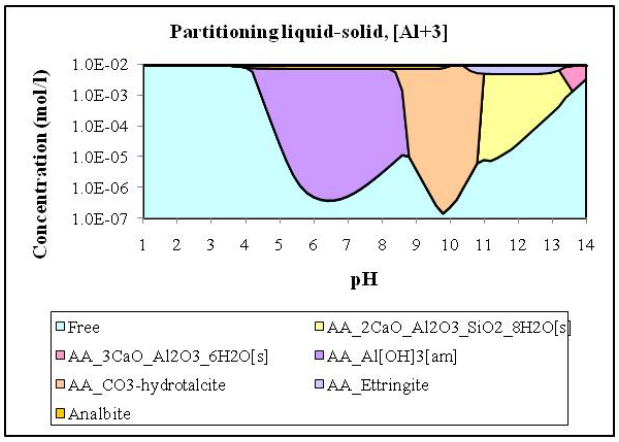

(b)

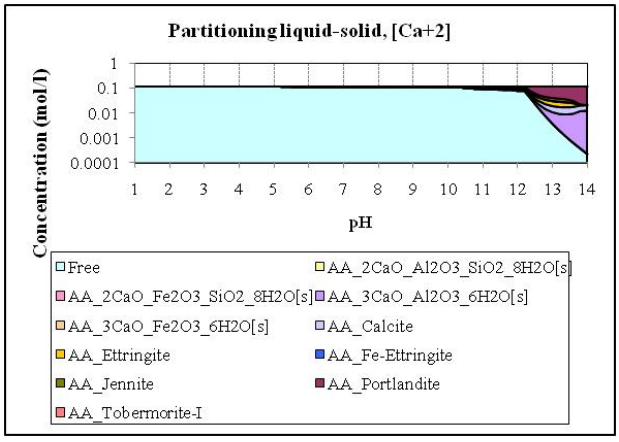

(c)

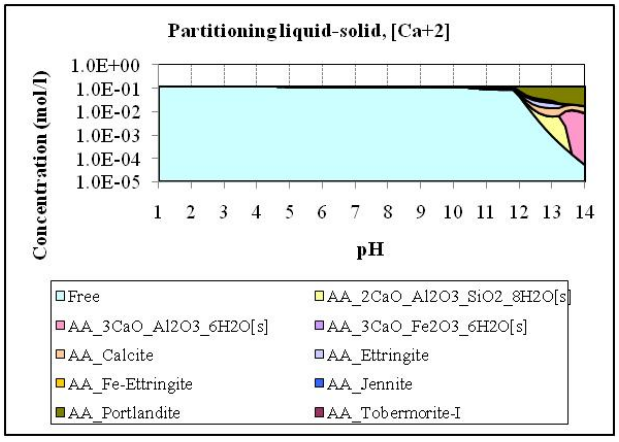

(d)

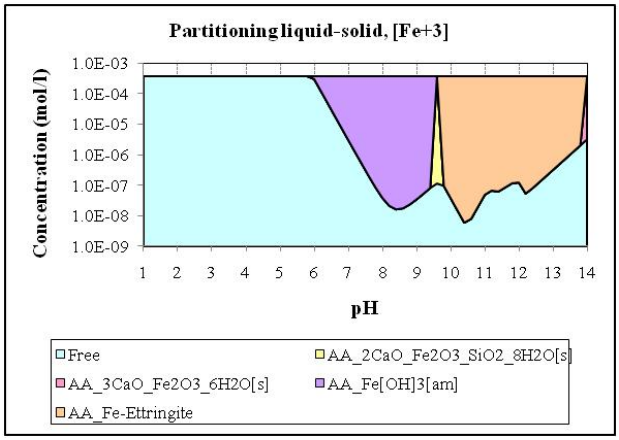
Partitioning liquid-solid, [Fe+3]
Concentration (mol/l)
1.0E-03
1.0E-04
1.0E-05
1.0E-06
1.0E-07
1.0E-08
1.0E-09
1 2 3 4 5 6 7 8 9 10 11 12 13 14
pH
Free
AA_2CaO_Fe2O3_SiO2_8H2O[s]
AA_3CaO_Fe2O3_6H2O[s]
AA_Fe[OH]3[am]
AA_Fe-Ettringite

(e)

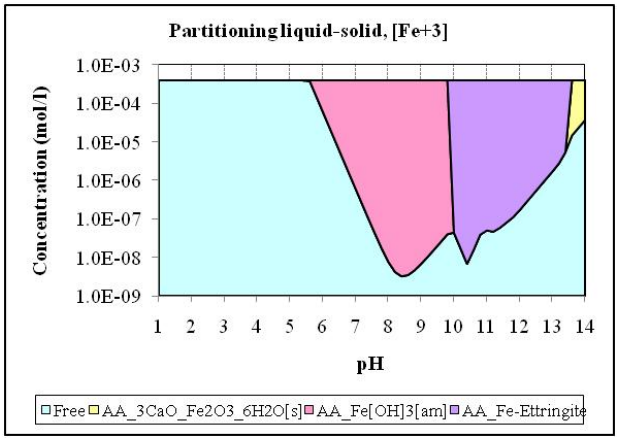
Partitioning liquid-solid, [Fe+3]
Concentration (mol/l)
1.0E-03
1.0E-04
1.0E-05
1.0E-06
1.0E-07
1.0E-08
1.0E-09
1 2 3 4 5 6 7 8 9 10 11 12 13 14
pH
Free
AA_3CaO_Fe2O3_6H2O[s]
AA_Fe[OH]3[am]
AA_Fe-Ettringite

(f)

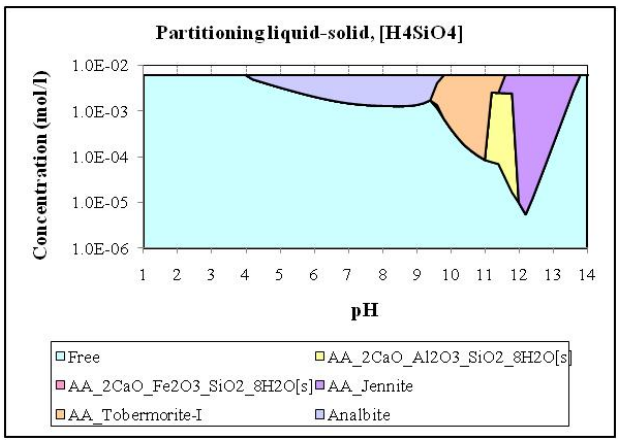
Partitioning liquid-solid, [H4SiO4]
Concentration (mol/l)
1.0E-02
1.0E-03
1.0E-04
1.0E-05
1.0E-06
1 2 3 4 5 6 7 8 9 10 11 12 13 14
pH
Free
AA_2CaO_Al2O3_SiO2_8H2O[s]
AA_2CaO_Fe2O3_SiO2_8H2O[s]
AA_Jennite
AA_Tobermorite-I
Analbite

(g)

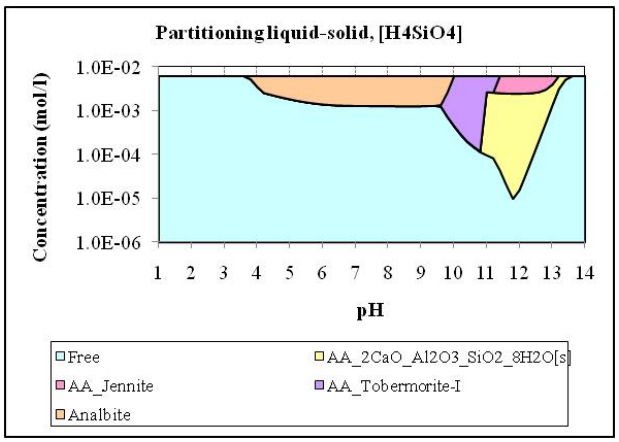
Partitioning liquid-solid, [H4SiO4]
Concentration (mol/l)
1.0E-02
1.0E-03
1.0E-04
1.0E-05
1.0E-06
1 2 3 4 5 6 7 8 9 10 11 12 13 14
pH
Free
AA_2CaO_Al2O3_SiO2_8H2O[s]
AA_Jennite
AA_Tobermorite-I
Analbite

(h)

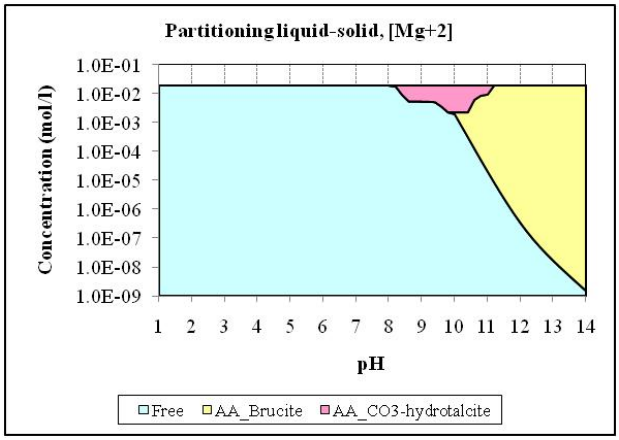
Partitioning liquid-solid, [Mg+2]
Concentration (mol/l)
1.0E-01
1.0E-02
1.0E-03
1.0E-04
1.0E-05
1.0E-06
1.0E-07
1.0E-08
1.0E-09
1 2 3 4 5 6 7 8 9 10 11 12 13 14
pH
Free
AA_Brucite
AA_CO3-hydrotalcite

(i)

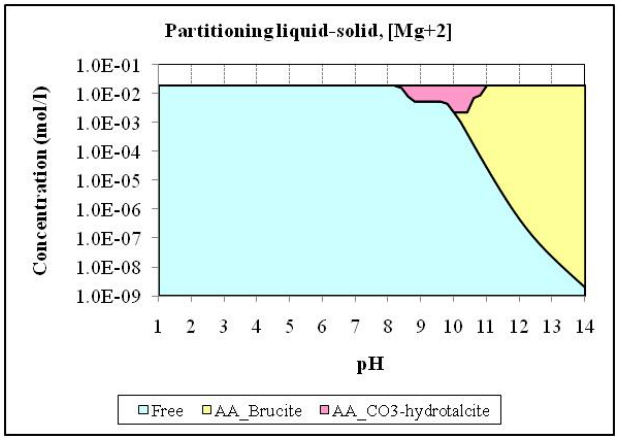
Partitioning liquid-solid, [Mg+2]
Concentration (mol/l)
1.0E-01
1.0E-02
1.0E-03
1.0E-04
1.0E-05
1.0E-06
1.0E-07
1.0E-08
1.0E-09
1 2 3 4 5 6 7 8 9 10 11 12 13 14
pH
Free
AA_Brucite
AA_CO3-hydrotalcite

(j)

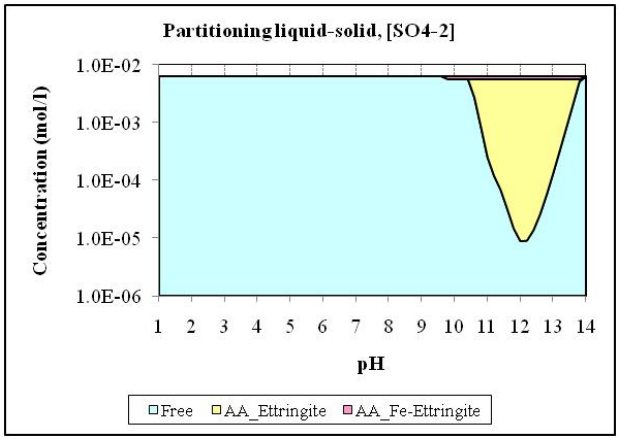

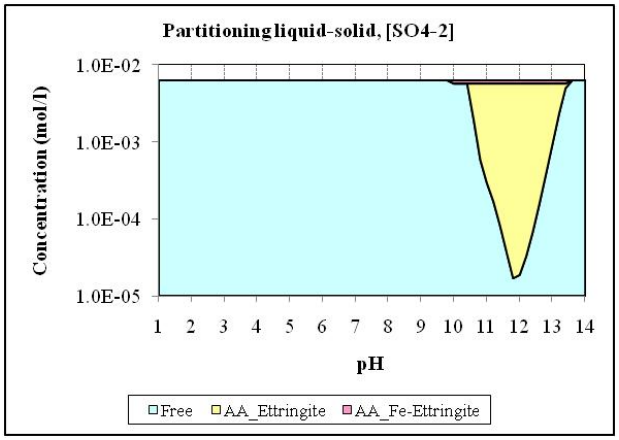

(k) (l)

Figure 5.9 : (a), (c), (e), (g), (i), (k) - Mineral precipitation domains using prior mean values; (b), (d), (f), (h), (j), (l) – Mineral precipitation domains using calibrated best fit values.

5.4.2 Concrete Sample

The delayed rejection adaptive Metropolis algorithm is used in this subsection to calibrate the model parameters of the chemical equilibrium module for a concrete sample [123, 124]. The sample is composed of Type V cement (ASTM C 150) mixed with grade 100 blast furnace slag (ASTM C 989), Type F fly ash (ASTM C618) and silica fume. The mass ratio of cement, slag, fly ash and silica fume is 1:1.34:0.79:0.22. The mass ratio of binder, sand and gravel is 1:1.35:2.74 and the water-binder mass ratio is 0.38. The sample is subjected to pH dependence test [104] as in the last subsection and the experimental observations comprise of concentrations of six species (e.g. $Al, Ca, Fe\ Mg, Si$ and S) at specific pH values. A set of 17 minerals are chosen after several preliminary trial runs and the mineral set is given in Table 5.3.

Table 5.3 : Mineral set chosen for calibration of equilibrium constants.

Mineral Phase	Expanded Formula	Common Name
$C_{1.67}SH_{2.1}$	$1.67CaO.SiO_2.2.1H_2O$	Jennite
$C_{0.83}SH_{1.3}$	$2CaO.2.4SiO_2.3.2H_2O$	Tobermorite-II
C_2ASH_8	$2CaO.Al_2O_3.SiO_2.8H_2O$	Stratlingite
C_2FSH_8	$2CaO.Fe_2O_3.SiO_2.8H_2O$	Fe-Stratlingite
C_3AH_6	$3CaO.Al_2O_3.6H_2O$	Hydrogarnet
C_3FH_6	$3CaO.Fe_2O_3.6H_2O$	Fe-Hydrogarnet
$Al(OH)_3$ (amorphous)	-	Gibbsite
$Mg(OH)_2$	-	Brucite
M_4ACH_8	$4MgO.Al_2O_3.CO_2.8H_2O$	CO_3-Hydrotalcite
$CaO.CO_2$	-	Calcite
$C_6A\bar{S}H_{32}$	$6CaO.Al_2O_3.32H_2O$	Ettringite
$C_6F\bar{S}H_{32}$	$6CaO.Fe_2O_3.32H_2O$	Fe-Ettringite
$Fe(OH)_3$ (microcrystalline)	-	Ferric Hydroxide
$C\bar{S}H_2$	$CaO.SO_3.2H_2O$	Gypsum
CH	$CaO.H_2O$	Portlandite
S	SiO_2	Silica
$NaAlSi_3O_8$	-	Albite

The equilibrium constants of the 17 minerals are calibrated using a three stage delayed rejection random walk adaptive Metropolis algorithm as described before. The scaling factors (γ) for the proposal covariance matrix in the three stages of the delayed rejection scheme are 0.04, 2.5×10^{-3} and 6.25×10^{-4}. The error envelope approach in conjunction with the orthogonal error is also used in this subsection. The total initial concentrations of the species are assumed to be normal with the mean values obtained from the LeachXS database and 10% COV. The prior distributions of the model parameters are assumed to be Gaussian with mean values obtained from the literature and 50% COV, as before. Figure 5.10 shows the trace plot of one of the model parameters using the basic Metropolis algorithm, the adaptive Metropolis algorithm and the delayed rejection adaptive Metropolis algorithm. It is evident from the figure that the acceptance rate is much greater for the case of the delayed rejection adaptive Metropolis than the

other two schemes. Figure 5.10c also shows that the sample generation approximately converged to a particular mean with a constant standard deviation.

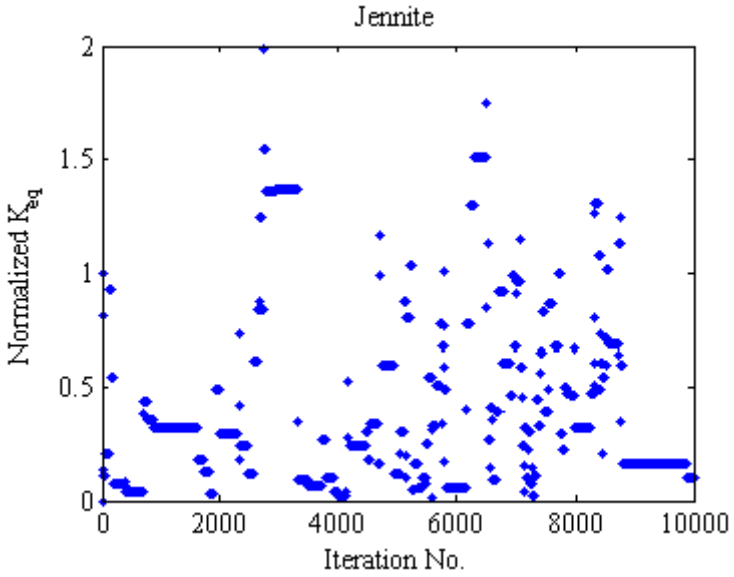

(a)

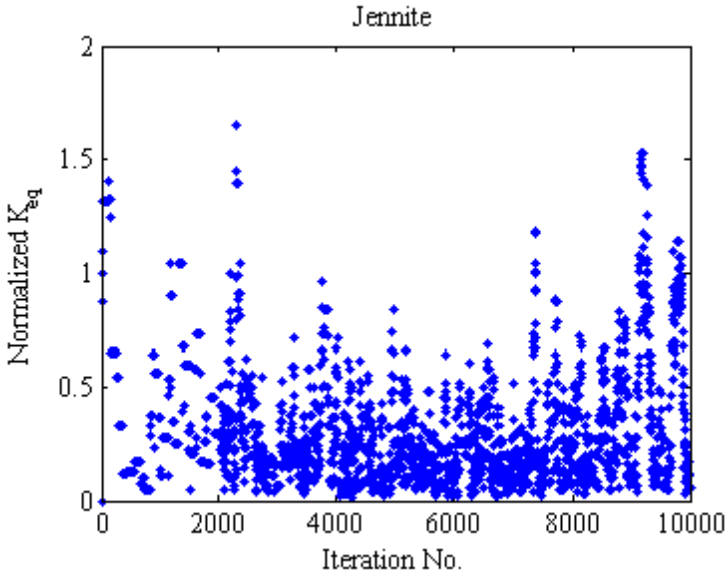

(b)

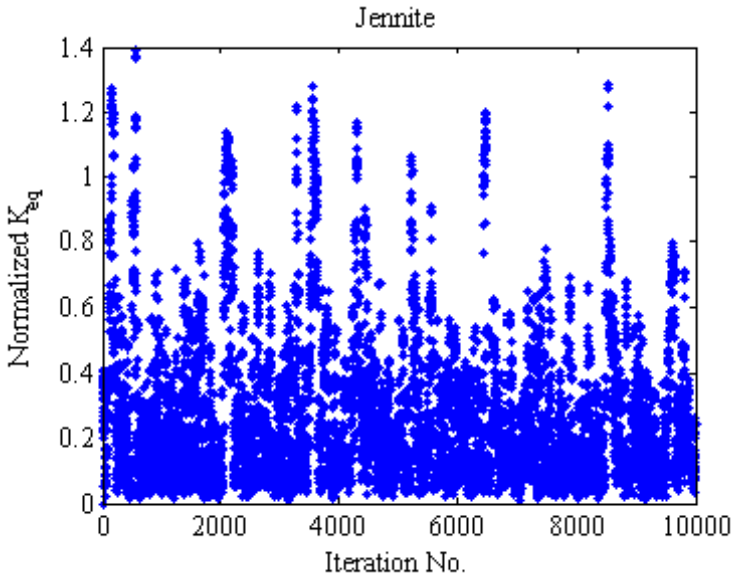

(c)

Figure 5.10 : (a) – Trace plot with basic Metropolis algorithm; (b) - Trace plot with adaptive Metropolis algorithm; (c) - Trace plot with delayed rejection adaptive Metropolis algorithm.

The prior and the posterior distributions are given in Figure 5.11. 3000 Monte Carlo simulations are performed to obtain the values of the model parameters that minimize the difference between the model predictions and the experimental observations while keeping the other input parameters constant. Figure 5.11 also shows the prior mean values and the calibrated best fit values. The prior mean values and the calibrated best fit values are given in Table 5.4 along with the % shift of the best fit values from the prior mean values. Figure 5.12 shows the comparison between the model predictions using the prior mean values and the calibrated best fit values. Finally, Figure 5.13 shows the comparison between the errors in model predictions using the prior mean values and the calibrated best fit values along with the reduction in the errors.

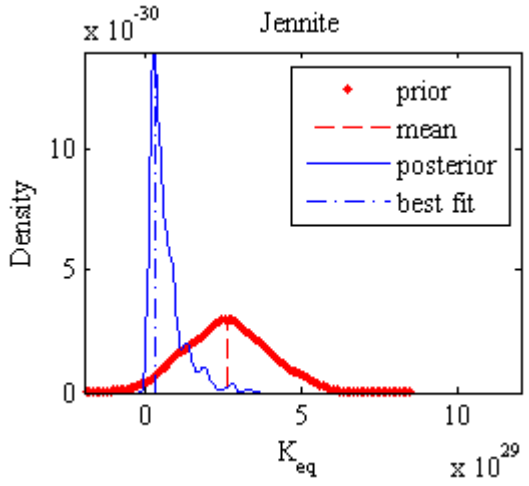
Jennite
x 10^-30
prior
mean
posterior
best fit
Density
K_eq
x 10^29

(a)

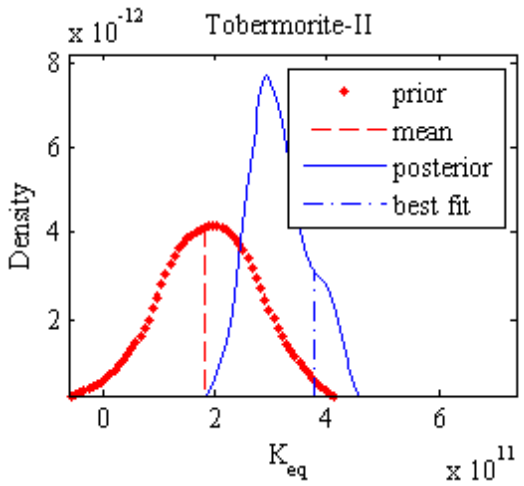
Tobermorite-II
x 10^-12
prior
mean
posterior
best fit
Density
K_eq
x 10^11

(b)

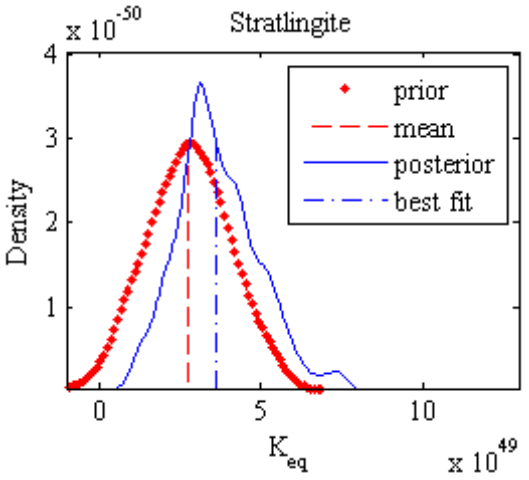
Stratlingite
x 10^-50
prior
mean
posterior
best fit
Density
K_eq
x 10^49

(c)

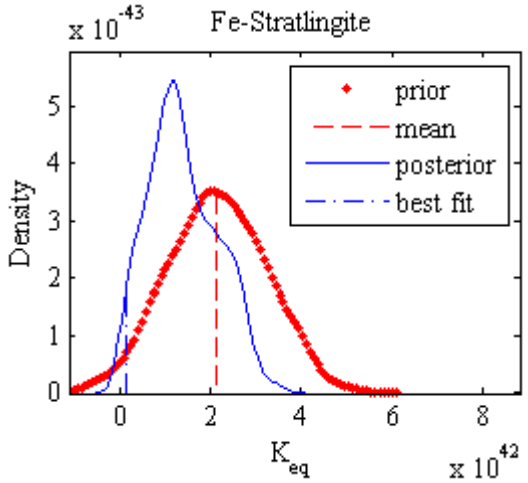
Fe-Stratlingite
x 10^-43
prior
mean
posterior
best fit
Density
K_eq
x 10^42

(d)

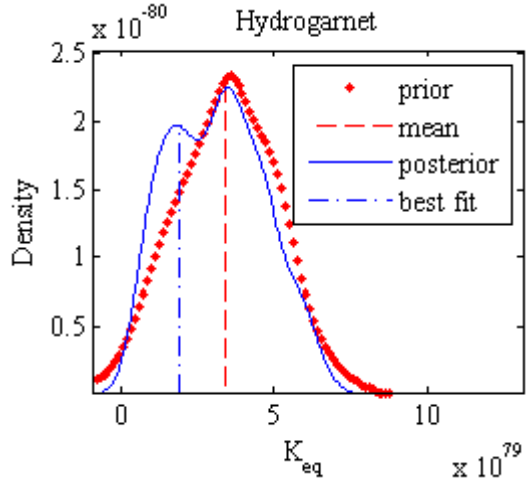
Hydrogarnet
x 10^-80
prior
mean
posterior
best fit
Density
K_eq
x 10^79

(e)

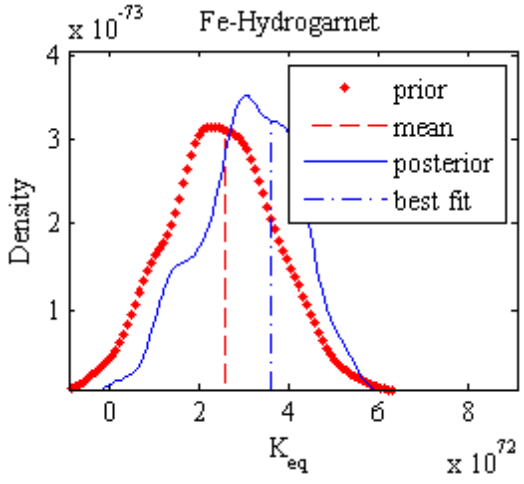
Fe-Hydrogarnet
x 10^-73
prior
mean
posterior
best fit
Density
K_eq
x 10^72

(f)

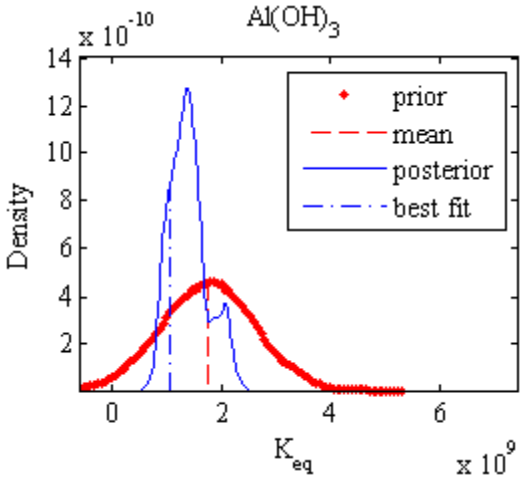
Al(OH)3
x 10-10
prior
mean
posterior
best fit
Density
Keq
x 10^9

(g)

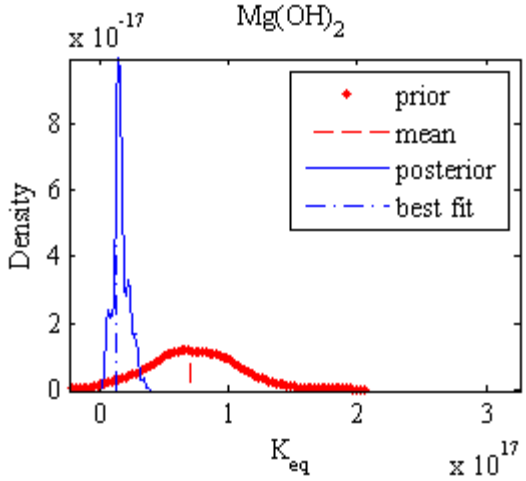
Mg(OH)2
x 10-17
prior
mean
posterior
best fit
Density
Keq
x 10^17

(h)

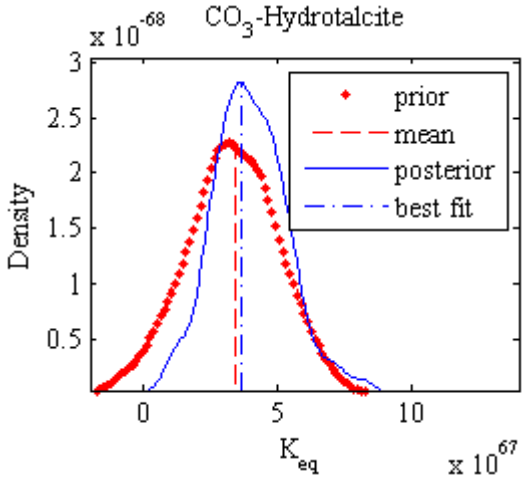
CO3-Hydrotalcite
x 10-68
prior
mean
posterior
best fit
Density
Keq
x 10^67

(i)

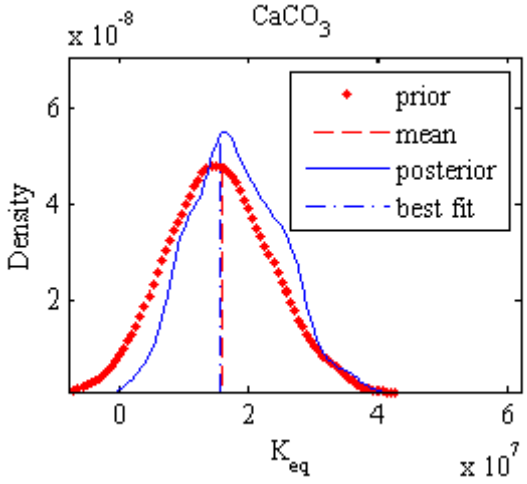
CaCO3
x 10-8
prior
mean
posterior
best fit
Density
Keq
x 10^7

(j)

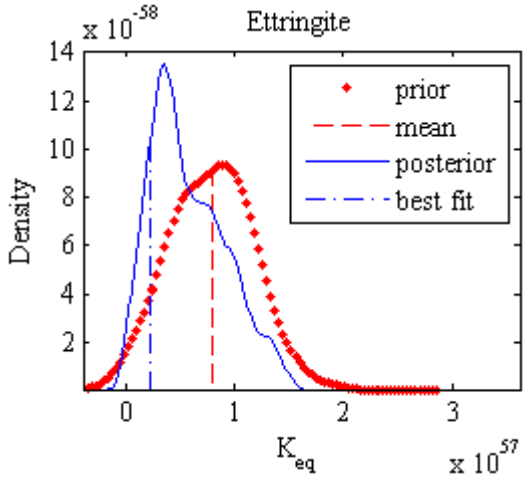
Ettringite
x 10-58
prior
mean
posterior
best fit
Density
Keq
x 10^57

(k)

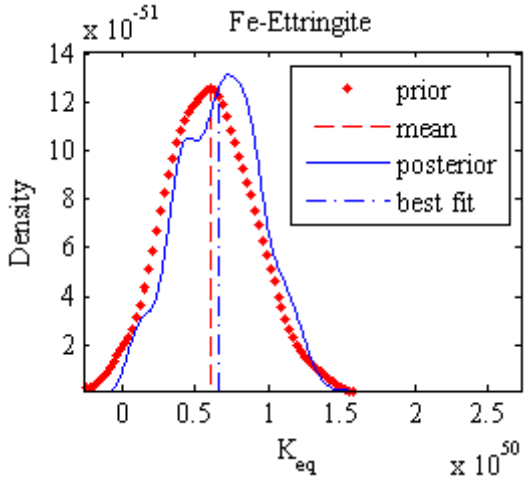
Fe-Ettringite
x 10-51
prior
mean
posterior
best fit
Density
Keq
x 10^50

(l)

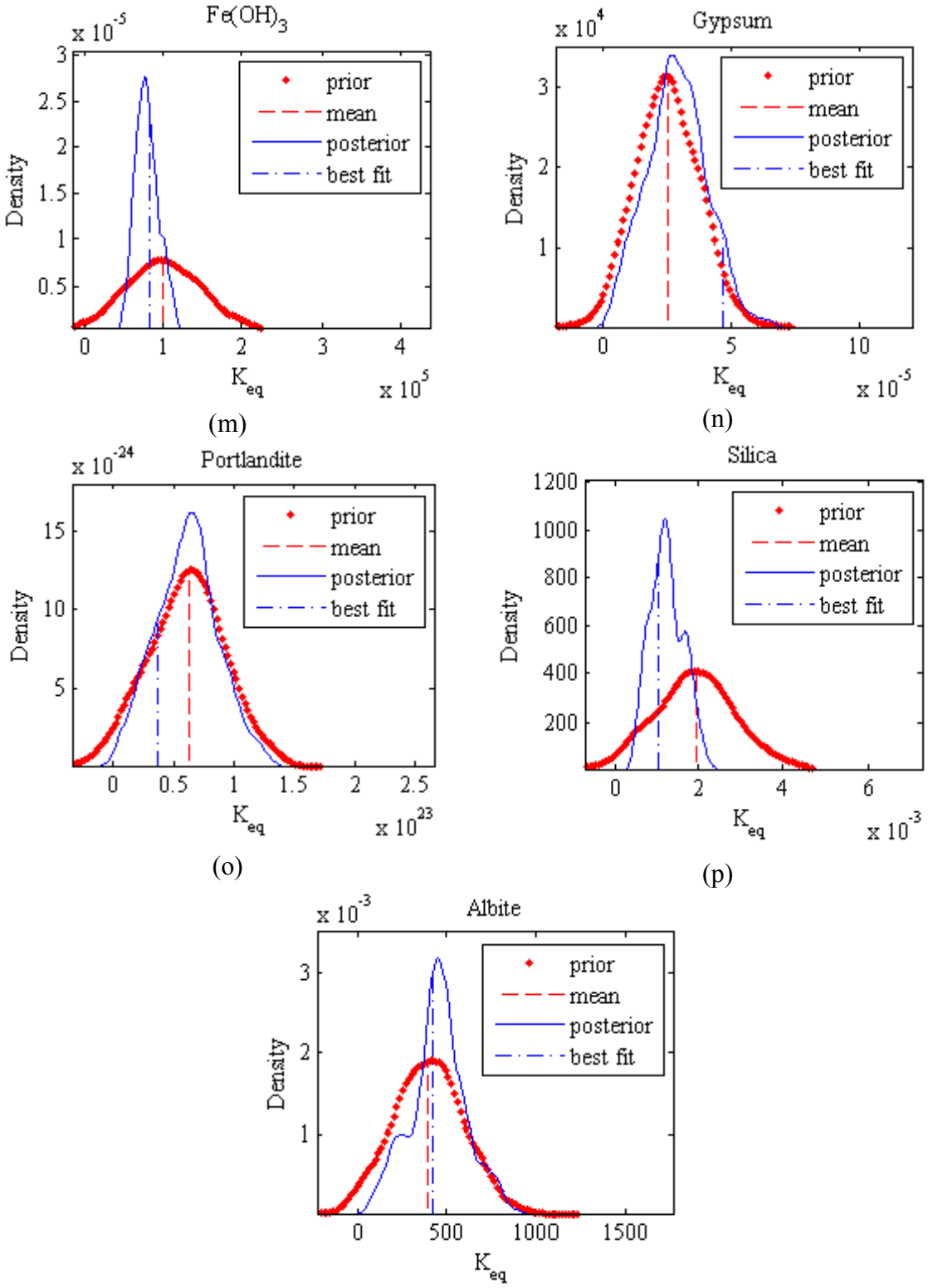

Figure 5.11 : Prior and posterior distributions of the model parameters.

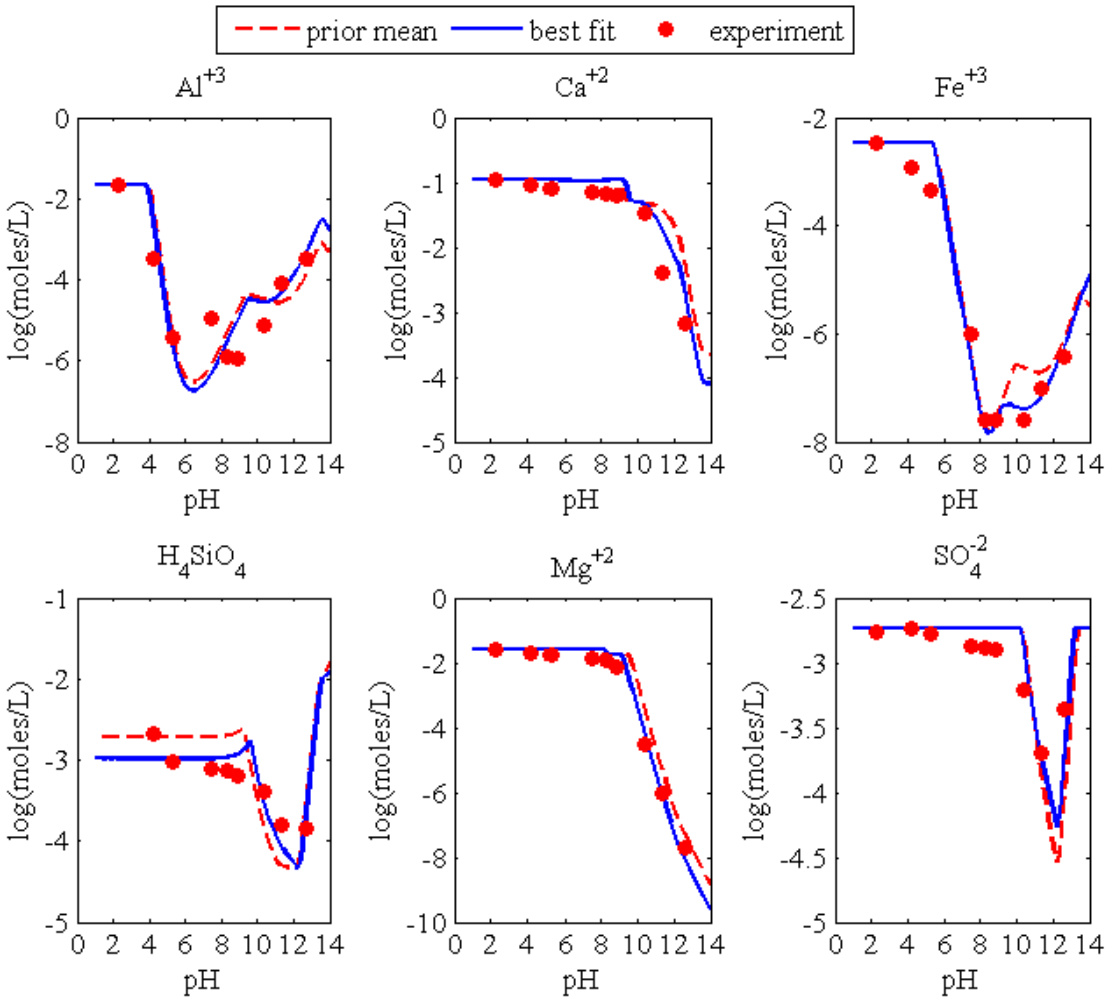

Figure 5.12 : Comparison of model responses using prior mean and calibrated best fit model parameters with the experimental results.

Table 5.4 : Model parameter values – prior mean vs. calibrated best fit.

Solid Phase	Prior Mean	Calibrated Best Fit	% Shift
Jennite	2.64×10^{29}	3.17×10^{28}	87.99
Tobermorite-II	1.83×10^{11}	3.76×10^{11}	-105.61
Stratlingite	2.74×10^{49}	3.63×10^{49}	-32.36
Fe-Stratlingite	2.13×10^{42}	1.19×10^{41}	94.41
Hydrogarnet	3.40×10^{79}	1.89×10^{79}	44.54
Fe-Hydrogarnet	2.58×10^{72}	3.61×10^{72}	-39.66
Gibbsite	1.75×10^{9}	1.05×10^{9}	39.68
Brucite	6.92×10^{16}	1.17×10^{16}	83.16
CO_3-Hydrotalcite	3.41×10^{67}	3.67×10^{67}	-7.46
Calcite	1.58×10^{7}	1.56×10^{7}	1.57
Ettringite	7.98×10^{56}	2.20×10^{56}	72.39
Fe-Ettringite	6.05×10^{49}	6.62×10^{49}	-9.42
Ferric Hydroxide	1.00×10^{5}	8.34×10^{4}	16.63
Gypsum	2.51×10^{-5}	4.71×10^{-5}	-87.63
Portlandite	6.27×10^{22}	3.71×10^{22}	40.83
Silica	1.94×10^{-3}	1.04×10^{-3}	46.06
Albite	3.91×10^{3}	4.22×10^{2}	-8.03

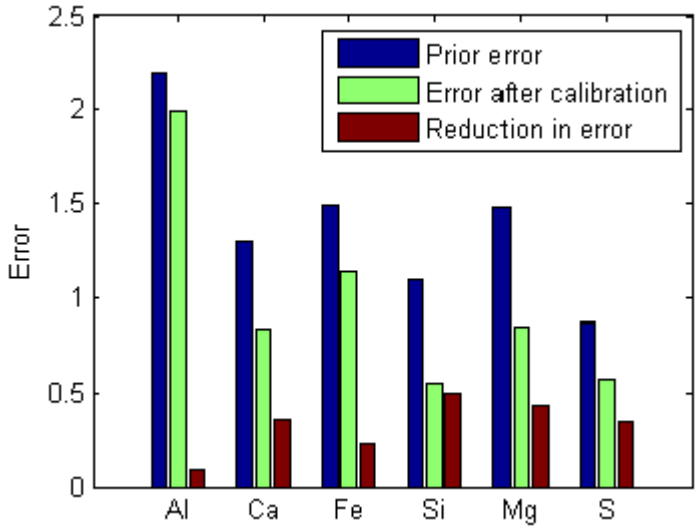

Figure 5.13 : Errors in model responses using prior mean and best fit calibrated model parameters.

5.4.3 Comparison with a similar concrete sample

The calibration results from Subsection 5.4.2 are used in this subsection on a similar concrete sample and the model predictions are compared with the experimental results.

The pH dependence test results for the concrete sample are obtained from the LeachXS database. The sample has cement and blast furnace slag mass ratio of 1:0.66, cement, sand and gravel mass ratio of 1:1.63:2.59 and water-binder mass ratio 0.38. The leaching test data provides concentrations of six species (e.g. $Al, Ca, Fe\ Mg, Si$ and S) at specific pH values. The posterior distributions of the same set of minerals as given in Table 5.3 are used to perform 5000 Monte Carlo simulations assuming that the total concentrations of the species have normal distributions with specified mean and 10% COV. Figure 5.14 shows the comparison of the mean model predictions and the 95% prediction intervals with the experimental results. The prediction intervals are calculated as [125]

$$\langle \mu \rangle_{1-\alpha} = \bar{x} \pm t_{\frac{\alpha}{2},n-1} \bar{s} \sqrt{1 + \frac{1}{n}} \tag{62}$$

where μ is the true mean of the population, $\bar{x}$ is the mean estimated from the model predictions, α is the prediction interval (= 95% in this case), n is the number of samples (= 5000 in this case), $t_{\frac{\alpha}{2},n-1}$ is the value obtained from student's t distribution at probability level of $\alpha/2$ and for $n-1$ degrees of freedom, and $\bar{s}$ is the standard deviation estimated from the model predictions. It is important to note that there are uncertainties associated with the pH measurements. Thus it can be said from the plots that the trends in the model predictions are approximately matching with the experimental results with the exception of Si concentrations in the pH range below 6. The difference between the model predictions and the experimental observations in that pH domain is mainly due to the fact that the kinetic aspect of the chemical reactions is neglected in the chemical equilibrium calculations. But the model predictions for Si match well in the pH range above 6 that is the more relevant pH range for cementitious materials. Overall, it can be

concluded that the model prediction intervals provide information on the overall uncertainty in the model predictions due to the uncertainties in the input and the model parameters, experimental errors and model errors arising from various assumptions and approximations in the model.

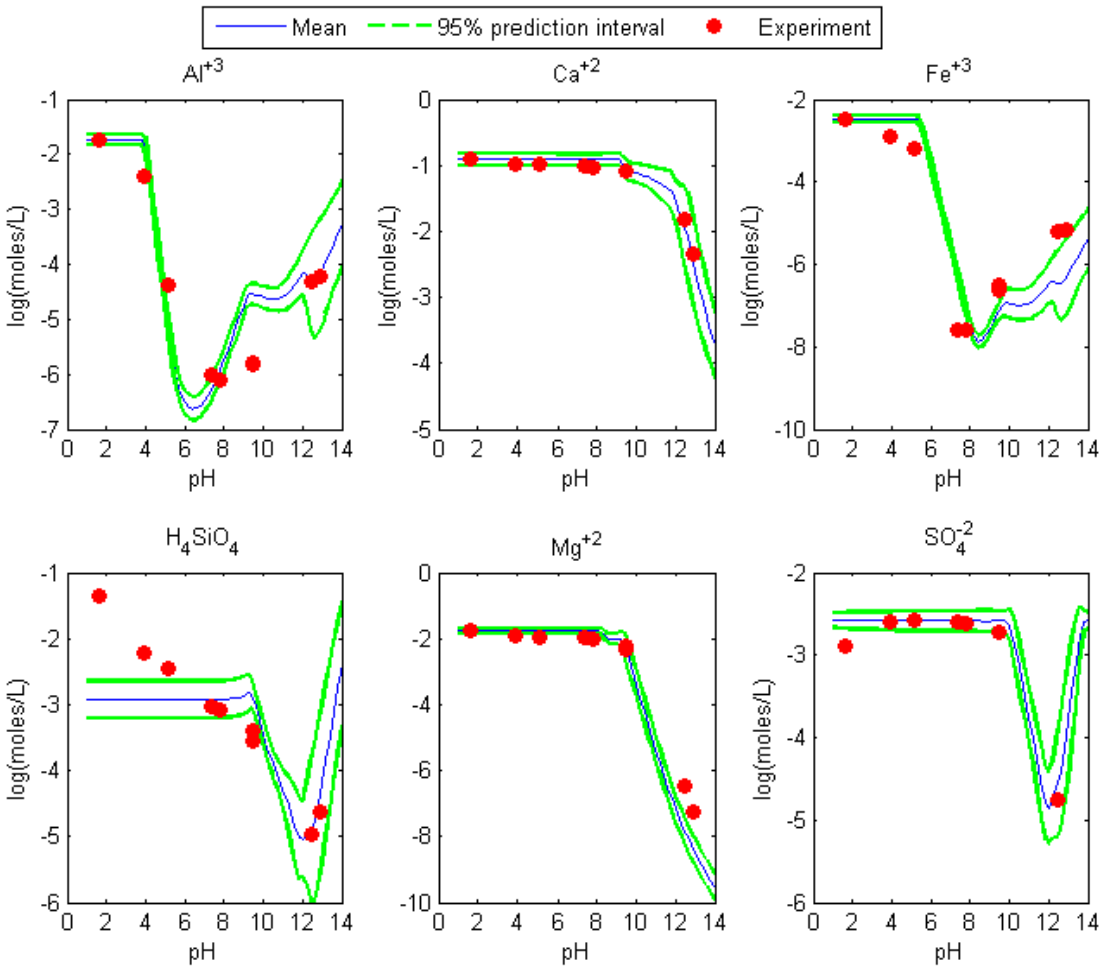

Figure 5.14 : Comparison between the model predictions and the experimental results.

5.5 Conclusion

A method is developed in this chapter for uncertainty quantification of model parameters of a chemical equilibrium model for cement-based materials. The chemical

equilibrium constants for the potential mineral phases are calibrated using a Bayesian approach. In the implementation it is shown that the delayed rejection adaptive Metropolis algorithm performs better with respect to speed and acceptance rate than the original Metropolis algorithm. The applicability of the method is demonstrated using the experimental results on the leaching behavior of a cement mortar sample and a concrete sample. The calibration results for the concrete sample are then used to compare the model predictions with the experimental results for a similar concrete sample. The calibrated model is shown to produce good agreement in the most relevant pH domain for the cementitious structures.

CHAPTER VI

PROBABILISTIC DURABILITY ANALYSIS OF CEMENTITIOUS MATERIALS UNDER EXTERNAL SULFATE ATTACK

6.1 Introduction

The numerical model developed in the previous chapters for assessing damage progression through a cementitious structure under external sulfate attack requires several input and model parameters for performing simulations. These parameters can be obtained from the experiments or from the literature. In either case, the values of the parameters will have some uncertainty associated with them, leading to uncertainty in the model response. Various methods are available in the literature for quantifying the uncertainty in the parameters and propagating it through the model, leading to the quantification of uncertainty in the model prediction. A numerical framework is developed in this chapter to incorporate the various sources of uncertainty in assessing the probability of reaching a particular degradation measure as a function of time. The approaches for quantifying and propagating uncertainty using a numerical model are described in the following sections. Later, the application of the framework is demonstrated for the concrete wall of a low activity nuclear waste containment structure exposed to sulfate containing pore solution of the waste material (i.e. saltstone). Water saturation is assumed as a conservative simplifying assumption for all cases in this dissertation. Actual field conditions typically are unsaturated which result in slower diffusion and degradation processes than predicted for saturated conditions.

6.2 Uncertainty Quantification

There are mainly three sources of uncertainty – (i) physical variability due to the inherent randomness of the variables, (ii) data uncertainty due to sparse or imprecise data, and (iii) model uncertainty and errors due to assumptions and approximations used during the modeling process. The approaches for quantification of different sources of uncertainty are described in this section.

6.2.1 Physical variability

In probabilistic analysis, the physical variations in the parameters are incorporated by defining them as random variables with probability density functions (PDFs). For a homogeneous structure modeled at the resolution of macro-scale, initial material and geometrical properties can be modeled as random variables. For example, bulk density of the material, mortar-water ratio, total open porosity, external sulfate concentration etc. are modeled as normal random variables by Rigo *et al.*, 2005 [37]. But some parameters may vary not only from sample to sample (as is the case for random variables), but also in space and/or time within the same sample. In these cases, they can be modeled as *random fields or processes* [126, 127]. Some of the well known methods for simulating random fields/processes are spectral representation (SR) [128], Karhunen-Loeve expansion (KLE) [129-131], polynomial chaos expansion (PCE) [127, 130-132] etc. Some boundary conditions generally exhibit a recurring pattern over shorter periods and also a trend over longer periods. These can be numerically represented by a seasonal model [133] using an autoregressive integrated moving average method generally used for linear processes (i.e. current observation is dependent on past observations) and

nonstationary processes (if the probability structure of the process varies with arbitrary translation of indexing parameter [134]). For example, this method can be used to simulate temperature patterns over the years which will affect the diffusivity and chemical activity coefficients. Rainfall can also be simulated using this method. The degree of soil saturation depends on the amount of rainfall. Diffusion of ions in and out of the underground concrete vaults containing nuclear wastes will depend on the soil saturation levels. Thus this method can be applied to simulate the time dependent environmental conditions which will affect the durability of the structure.

6.2.2 Data uncertainty

In a numerical simulation, data uncertainty comes from complete or partial lack of knowledge of some input parameters. For example, data for the threshold strain (ε^{th}) and the calibration parameters (k and m) in Eq. (28) may not be available in sufficient quantity to justify the assumption of a particular type of distribution.

If the available data set is small, an *empirical distribution function* can be constructed by ranking the observations and assigning a probability value to each observation. An alternative approach in this regard is to use *a flexible family of distributions* such as the Johnson family to fit a data set [135]. In either case, the parameters of the chosen distribution will have uncertainty due to sparseness of the data, which will lead to uncertainty in the model prediction. One approach to represent the uncertainty in the distribution parameters is through probability distributions of the distribution parameters themselves. Several approaches are available in the literature for constructing statistical distributions of the distribution parameters [110, 136, 137]. One approach for

constructing distributions of distribution parameters having an underlying normal population is as follows: let X be a sample set of size n that is assumed to have an underlying normal distribution with true but unknown mean and variance μ and σ^2 respectively. The sample mean and variance calculated from X are $\bar{x}$ and $\bar{s}^2$ respectively. Then, $\frac{\bar{x}-\mu}{\bar{s}/\sqrt{n}}$ and $\frac{(n-1)\bar{s}^2}{\sigma^2}$ are observed to have the *student's t* distribution and *chi-square* distribution with $n-1$ degrees of freedom respectively [110]. This approach is used in Section 6.5 for constructing distributions of distribution parameters to incorporate uncertainty due to small sample size.

The available data set may be composed of interval values. For example, upper and lower bounds of the Young's modulus of the concrete sample may be obtained from several experts or from the literature. In such cases, statistical distributions can again be constructed using the Johnson family of distributions [135, 138] resulting in distributions with uncertain parameters. This will result in a family of CDFs from which upper and lower bounds of the CDFs can be obtained. The statistical distributions constructed in this manner can be propagated through a numerical model by using a nested or a single loop MCS that will result in an ensemble of durability curves. The specific approaches for uncertainty propagation will be described in Section 6.3. Finally, the bounds on the probability of reaching a particular degradation measure as a function of time can be estimated from the ensemble of the durability curves.

6.2.3 Model uncertainty

Model uncertainty can come from various approximations and assumptions made during the modeling process such as incomplete knowledge of the physics of the

phenomenon, and analysis approximations. Verification, validation, calibration, and error quantification are different steps to address model uncertainty. The sulfate attack model described in this dissertation is also based on several assumptions. For example, the uncertainty in the chemical equilibrium model is the combined effect of (1) the uncertainty in the model parameters, and (2) model error due to the assumptions and approximations inherent in the underlying conceptual model and mathematical representation thereof, e.g., local equilibrium assumption in the chemical reaction module and ignoring the kinetic component of the chemical reactions. Thus it is essential to quantify the model uncertainty and incorporate that into the uncertainty analysis when assessing the durability of the structure. Therefore, the uncertainty in the model parameters of the chemical equilibrium module is quantified by performing calibration using the Bayesian calibration method in Chapter V.

One of the approaches used in the literature for assessing validity of a model is to calculate a validation metric to accept or reject the particular model. The statistical parameters of the model predictions and experimental observations can be compared using classical hypothesis testing. Alternatively, *Bayesian hypothesis testing* is also used by some researchers [127, 139, 140] to assess model validity, and used to quantify confidence in the model prediction.

One approach for quantifying the model error is by comparing the difference between the model prediction and the experimental observation, and incorporating various sources of errors through their variances [141]. Recently, a method was developed to quantify model error by combining errors due to model form, numerical discretization, uncertainty analysis method and input and output measurements [127].

The numerical model developed in this research uses a finite difference method for the solution of the diffusion equations. Thus it is essential to evaluate the numerical discretization error in the simulations. This error is generally evaluated by using *a priori* error norms e.g. L_2 norm and energy norm or *a posteriori* error measures such as the Richardson extrapolation technique [142, 143]. The Richardson extrapolation technique is simple and the method is described in this section. The discretization error is expressed as [144]

$$DE_k = f_k - f_{\text{exact}} \tag{63}$$

where DE_k is the discretization error for k^{th} mesh, f_k is the numerical solution for mesh k and f_{exact} is the exact or true solution. Assuming that the discretization error can be expressed as a Taylor series expansion, the numerical solution for mesh size k can be written as

$$f_k = f_{\text{exact}} + g_p h_k^p + \mathcal{O}(h_k^{p+1}) \tag{64}$$

where g_p is the p^{th} order error term coefficient, h_k is the element size for mesh k, p is the order of convergence and $\mathcal{O}(.)$ represents the higher order error terms that can be neglected. The value of p can be easily calculated for well known differential equations of which the exact analytical solutions are available. Alternatively, it can be calculated if the value is not known for complex and coupled problems such as the one considered here. In such cases, three numerical solutions with different mesh sizes are used that are expressed as

$$f_1 = f_{\text{exact}} + g_p h_1^p \tag{65}$$

$$f_2 = f_{\text{exact}} + g_p h_2^p \tag{66}$$

$$f_3 = f_{\text{exact}} + g_p h_3^p \tag{67}$$

where $h_1 < h_2 < h_3$. The three unknowns f_{eaxct}, g_p and p are solved by rearranging the Eqs. (65)-(67) as

$$\frac{r_{12}^p - 1}{r_{12}^p r_{23}^p - 1} = \frac{\varepsilon_{21}}{\varepsilon_{21} + \varepsilon_{32}} \tag{68}$$

$$g_p = \frac{\varepsilon_{32}}{r_{23}^p - 1} \frac{1}{h_2^p} \tag{69}$$

$$f_{\text{exact}} = f_3 - \frac{\varepsilon_{32}}{r_{23}^p - 1} r_{23}^p \tag{70}$$

where $r_{12} = h_2/h_1$, $r_{23} = h_3/h_2$, $\varepsilon_{21} = f_2 - f_1$ and $\varepsilon_{32} = f_3 - f_2$. The error associated with the coarse mesh solution can be approximated as

$$DE_3 = f_3 - f_{\text{exact}} = \frac{\varepsilon_{32}}{r_{23}^p - 1} r_{23}^p \tag{71}$$

Application of this method is contingent upon fulfillment of some conditions such as [142, 143, 145, 146]: (1) the exact solution must be smooth so that the Taylor series expansion is justified for expanding the discretization error as done in Eq. (64), (2) the mesh size must be sufficiently small so that the numerical solution is in the asymptotic monotone grid convergence range, and (3) the local error order is the same as the global error order. If these conditions are not satisfied, application of the Richardson extrapolation method may result in divergence in model prediction [142, 143, 146]. Thus the Richardson extrapolation technique should not be applied without consideration of the basic assumptions. Also, the grid refinement does not necessarily mean improvement in solution; refining grids may sometimes lead to accumulation of machine rounding error and incomplete iteration error [145, 147].

In this section, different approaches for quantifying three main sources of uncertainty – physical variability, data uncertainty and model uncertainty, are discussed. The input

and the model parameters of a numerical model can be simulated using the above mentioned approaches. The numerical model developed in the previous chapters is composed of three essential components – diffusion of ions, chemical reactions and damage accumulation. Various physical and chemical parameters in these components are simulated in Section 6.5 using the approaches discussed in this section. Several methods are available in the literature for propagating these uncertainties through the numerical model so that the uncertainty in the model response can be quantified. The uncertainty propagation methods are described in the next section.

6.3 Uncertainty Propagation

The ultimate goal of this dissertation is durability assessment including uncertainty evaluation of cementitious materials under external sulfate attack as a function of time. A numerical model is developed for this purpose as described in the previous chapters. Uncertainty in various parts of the model arising from different sources affects the model prediction. These uncertainties can be quantified using the methods described in the previous section. Then, the problem of durability assessment can be formulated as a time-dependent reliability analysis to assess the evolution of the probability of reaching a specified level of degradation with time [47, 48, 50, 148-150] by Monte Carlo Simulation (MCS) [110], First Order Reliability Method [110], etc. MCS is the most commonly used method in the literature which can be time consuming. Various efficient sampling techniques can be used to minimize the computer time or storage requirement, e.g., Latin hypercube sampling, importance sampling, etc.

The statistical descriptions of the input and model parameters are essentially of two types – (1) PDFs (probability density functions) having constant parameters, e.g. parameters having physical variability and model parameters calibrated using experimental results, and (2) PDF's having parameters that are themselves expressed as PDFs with constant parameters, e.g. parameters having data uncertainty. Two approaches are explored in this section for uncertainty quantification in the durability assessment incorporating the abovementioned two types of statistical descriptions of the parameters. The first method incorporates a nested Monte Carlo simulation where the outer loop generates samples of the distribution parameters of the variables having data uncertainty and the inner loop generates samples of all the parameters. As shown in Figure 6.1, N_2 samples of distribution parameters of variables having data uncertainty are generated. For each of N_2 samples, N_1 samples of the variables having physical variability and data uncertainty are generated, and the simulations are performed. The model errors (if available) can be added to the simulation results at this stage. Thus a total of $N_1 \times N_2$ simulations are performed. A single durability curve can be constructed using all of the N_1 model responses from the inner loop Monte Carlo simulations by comparing the model responses with a particular performance requirement, e.g., the maximum allowable stress or strain in the structure. Thus, N_2 durability curves are obtained from the nested Monte Carlo simulations, leading to probability bound calculation using the generated durability curves and the number of samples. An example of the nested MCS is shown in Figure 6.3. This method is computationally expensive for a large finite element multiphysics time dependent problem. A surrogate model, e.g., Gaussian process model [151], can be used in such cases to reduce the computational time. The Gaussian process

model is essentially a nonparametric way of representing the relation between the inputs and the outputs of the model. This method is flexible and easy to use as it does not require any functional relation between the inputs and the outputs [152].

The second method incorporates the aforementioned uncertainties in the input and the model parameters in a single loop Monte Carlo simulation by consolidating the nested simulations into one loop. In this case, N samples are generated for variables having physical variability and data uncertainty as shown in Figure 6.2. Simulations are performed for each set of samples generated and probability of reaching a particular degradation measure as a function of time is calculated. Thus a single durability curve is obtained as a result of the simulations in this case. An example of the durability curve generated using the single loop MCS is shown in Figure 6.4. The main difference between the single loop and the nested loop MCS is that the former produces unconditional durability curves whereas the later produces durability curves conditioned on the values of distribution parameters of the parameters having data uncertainty. Alternatively, the single loop MCS can be viewed as the integrated durability curve of the ensemble of the curves generated using the nested loop MCS.

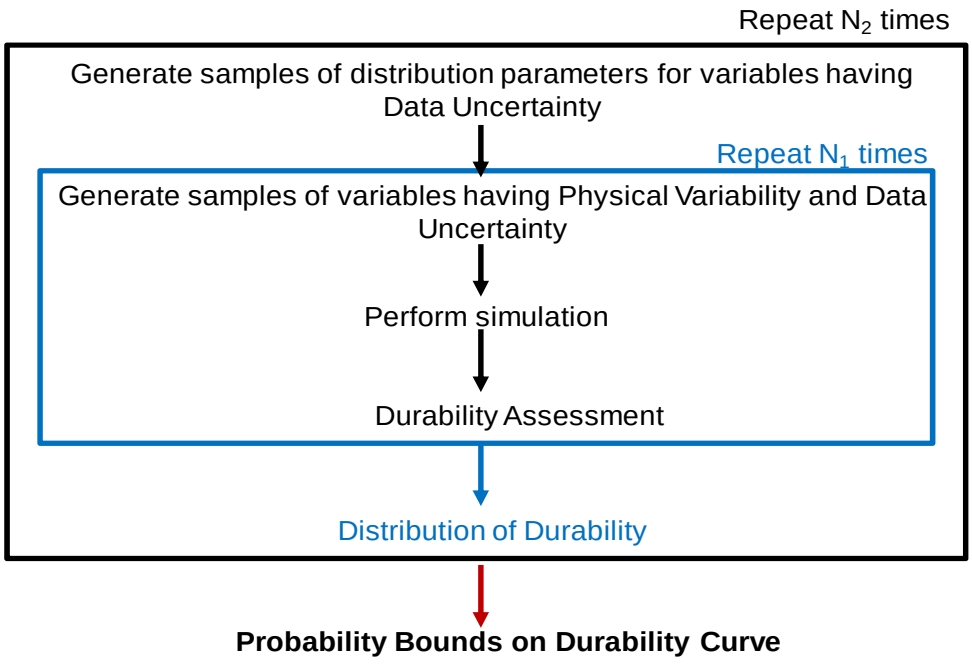

Figure 6.1: Probabilistic durability assessment using nested Monte Carlo simulation.

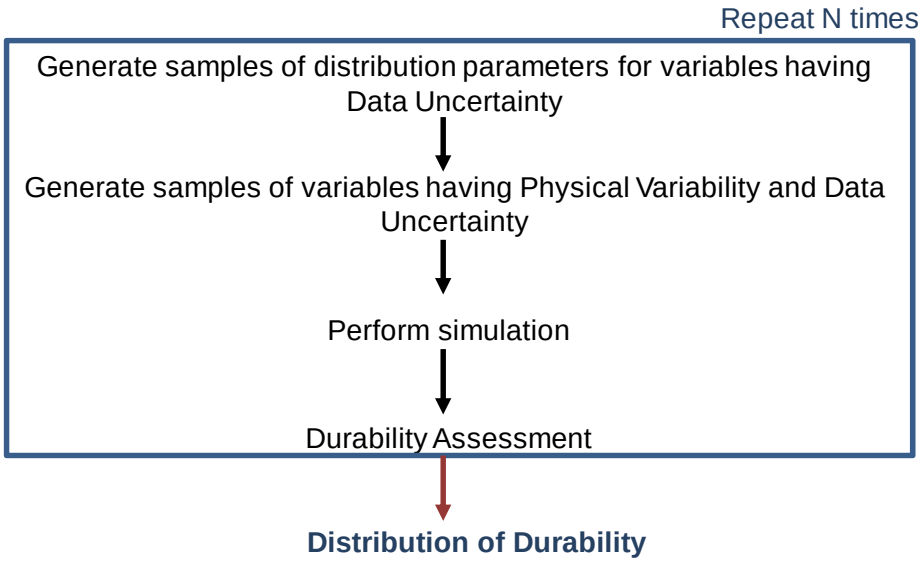

Figure 6.2 : Probabilistic durability assessment using single loop Monte Carlo simulation.

6.4 Application of Nested and Single Loop Monte Carlo Simulation

The application of the nested and single loop Monte Carlo simulation for the durability assessment of the structure is demonstrated in this section. A U.S. Type I cement mortar sample of size $25\text{ mm} \times 25\text{ mm} \times 285\text{ mm}$ immersed in a tank of Na_2SO_4 solution is considered for illustration purposes. The liquid volume to solid volume ratio is 10. The cement, water and sand mass ratio is $1{:}\,0.5{:}\,3$. A one-dimensional idealization of the three dimensional structure is simulated using the method described in Chapter II. The simulations are performed for 2 years for each set of random variables generated for the Monte Carlo simulation. The statistical descriptions of the parameters are given in Table 6.1. $N(\mu, \sigma)$ represents a normal distribution with mean μ and standard deviation σ. $U(LB, UB)$ represents a uniform distribution with LB as the lower bound and UB as the upper bound. The model error is not considered in this example due to the lack of experimental results.

Table 6.1 : Statistical descriptions of the parameters.

Input Type	Distribution
Physical variability	
Initial porosity	$N(0.3, 0.03)$
Initial tortuosity	$N(36, 3.6)$
pH of the external solution	$N(7, 1.4)$
Solution concentration (moles/L)	$N(0.35, 0.07)$
Renewal rate of solution (day)	$U(5, 15)$
Data uncertainty	
Fraction of porosity available ($\boldsymbol{b}$)	$U(LB, UB)$ $LB \sim U(0.05, 0.15)$ $UB \sim U(U(0.25, 0.35)$
Peak stress (MPa)	$N(f_t, 0.5)$ $f_t \sim N(3, 0.3)$
Initial Young's modulus (GPa)	$N(E_0, 5)$ $E_0 \sim N(20, 2)$

The structure is assumed to have failed if 50% of the thickness of the structure reaches the maximum damage level. An element in the structure reaches the maximum damage level when the damage parameter associated with that element reaches the maximum value (assumed to be 0.9 as mentioned in Chapter II). The durability analysis is performed using the nested and the single loop MCS methods as explained in the previous section. A Gaussian process surrogate model is built trained on 50 numerical simulations of the full multiphysics model to reduce the computational time. Then 500 samples in the outer and the inner loops are generated for parameters having data uncertainty and physical variability and the nested Monte Carlo simulation is performed. It is important to acknowledge the fact that additional uncertainty is introduced in the simulation due to the use of the surrogate model which is not included in this demonstration case. Figure 6.3 shows the ensemble of durability curves from the nested loop MCS. Also, the 50 numerical simulations of the full multiphysics model are used in a single loop Monte Carlo simulation to generate a single durability curve as shown in Figure 6.4.

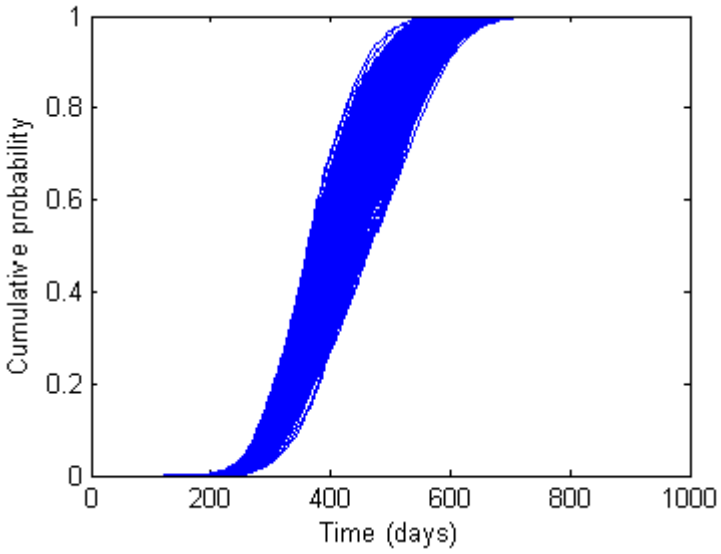

Figure 6.3: Cumulative probability of time to failure curves using nested Monte Carlo simulation.

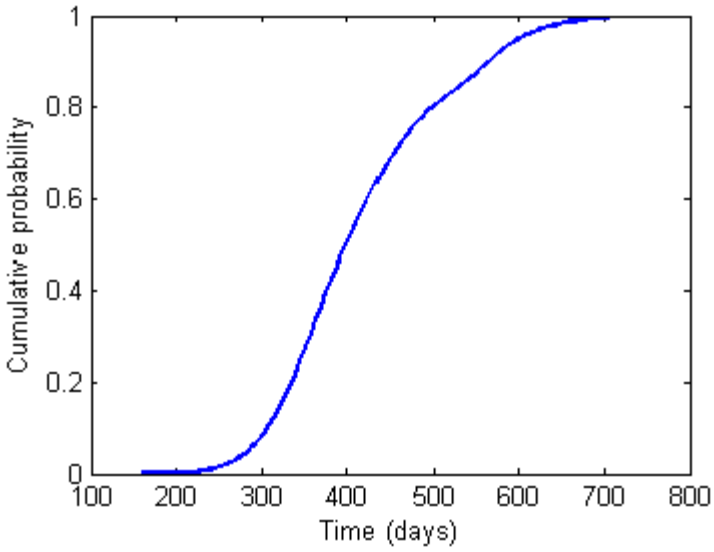

Figure 6.4: Cumulative probability of time to failure curve using single loop Monte Carlo simulation.

As mentioned before, the durability curve in Figure 6.4 is the unconditional cumulative distribution function, whereas the curve in Figure 6.3 is conditioned on the values of the distribution parameters. Figure 6.3 explicitly shows the contribution of data uncertainty,

whereas Figure 6.4 integrates all the sources of uncertainty into a single cumulative distribution function curve.

6.5 Probabilistic Durability Assessment

6.5.1 Overview of the problem

The effects of uncertainty from different parts of the model on the durability assessment of the structure are demonstrated in this section. A concrete wall of a low activity nuclear waste (i.e. saltstone) containment structure is considered for demonstration purposes. The wall is exposed to 24000 mg/L of sulfate solution as is present in the saltstone pore solution as mentioned in Chapters I and IV [2]. Water saturation is assumed as a conservative simplifying assumption for all cases. Actual field conditions typically are unsaturated which result in slower diffusion and degradation processes than predicted for saturated conditions.

The material characteristics of the concrete mix are given in Table 6.2.

Table 6.2 : Characteristics of the concrete sample [123, 124].

Properties	Quantities
Cement type	V
Water-cement ratio	0.38
Cement (kg/m^3)	121
Granular blast furnace slag (kg/m^3)	162
Fly Ash (kg/m^3)	95
Silica Fume (kg/m^3)	27
Fine aggregate (kg/m^3)	548
Coarse aggregate (kg/m^3)	1111
Porosity	10
Tortuosity	430
Compressive strength (MPa)	70

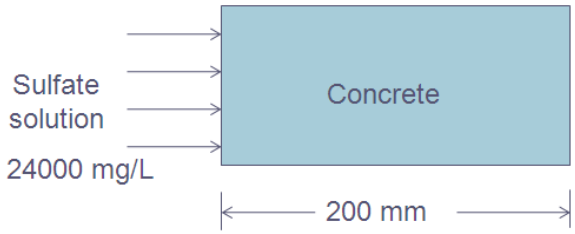

Figure 6.5 : Concrete wall exposed to sulfate solution.

The total leachable concentrations of the species are obtained from the LeachXS database and used in the numerical simulations. The thickness of the concrete wall is 200 mm as shown in Figure 6.5. The structure is divided into 100 nodes with no flux boundary condition at $x = 200$ mm and exposed to 24000 mg/L of sulfate solution at $x = 0$. The sulfate solution is refreshed every 3 months so that the concentration of sulfate at $x = 0$ remains approximately at 24000 mg/L. The simulations are performed for 100 years. The mineral set chosen for the simulations is the same as the one calibrated in Chapter V. The fraction of porosity that needs to be filled before strain can develop (b in Eq. (20)) is assumed to be 0.3 due to the lack of experimental data.

The evaluation of structural damage due to cracking using the method as described in Chapter II requires several material parameters that need to be extracted from the experimental stress-strain diagram. In the absence of a stress-strain diagram for the reference material, empirical formulas are applied to obtain the parameters that are required to generate the stress-strain diagram for the material. Five parameters are needed to reproduce the stress-strain diagram as shown in Figure 2.6 of Chapter II – initial Young's modulus (E_0), ultimate tensile strength (f_t), threshold strain (ε_{th}) and two model parameters (i.e. k and m). The two model parameters are assumed to be 0.16 and 2.3

from the literature [10]. Calculations for the remaining three parameters are described below.

The initial Young's modulus is related to the compressive cube strength of concrete (as obtained from Table 6.2) according to the British Code of Practice (CP110, Part 1) and can be expressed as [51]

$$E_0 = 9.1(f_c')^{1/3}\text{GPa} \tag{72}$$

with a standard deviation of 4 GPa (reported as $\pm$ 4 GPa variability in [51]) for concretes having a density of $2300\ \text{kg/m}^3$ and f_c' is the compressive strength of concrete in MPa. According to the European Concrete Committee, the axial tensile strength can be calculated as [51]

$$f_t = 0.3(f_c')^{2/3} \tag{73}$$

with COV of 30% (reported as variability of $\pm$ 30% in [51]). Finally, the threshold strain is assumed to be at the 40% of the peak stress [153]. It can also be assumed to be up to 50 or 60% of the peak stress [154, 155].

6.5.2 Various sources of uncertainty

The numerical framework for degradation modeling of cementitious materials under external sulfate attack consists of three components – (1) diffusion of ions, (2) chemical reactions, and (3) structural damage due to cracking. Various sources of uncertainty and errors in these three components of the model that contribute to the overall uncertainty in the model prediction are described below.

1. Diffusion of ions
    a. Physical variability comes from the inherent randomness in the input

parameters that are observable/measureable quantities, e.g. porosity and tortuosity, inherent randomness in the boundary condition, e.g. sulfate concentration at the boundary.

b. Data uncertainty comes from sparse or interval data, i.e. due to small number of samples used for porosity and tortuosity determination.

c. Model uncertainty arises due to the various assumptions and approximations in the model, e.g. neglecting electrical potential in the diffusion equation, and uncertainty associated with the empirical relations used in the model, e.g. Eq. (19) for changing diffusivity due to change in porosity. Also, conservative assumptions of saturated conditions and constant sulfate concentartion at the boundary as opposed to the actual field condition add to the model uncertainty. These asusmptions result in estimates of diffusion and cracking rates that are faster (i.e. conservative) than actual field conditions. Model error also comes from the discretization error in time and space in the finite difference method that is used to solve the equations.

d. Experimental error is present in any measurement of any parameter of the model.

2. Chemical reactions

a. Physical variability in this component of the model comes from the inherent randomness in the input parameters that are observable/measureable quantities, e.g. total concentrations of the species available for reaction.

b. Data uncertainty arises from sparse or interval data, e.g. small number of samples used for measurement of the total concentrations of the ions.

c. Uncertainty in the model parameters that are not directly observable/measureable contribute to the model uncertainty, e.g. equilibrium constants of the chemical reactions. Additionally, uncertainty due to various assumptions and approximations affect the model response, e.g. the assumption of local equilibrium and not incorporating kinetic aspect of the chemical reactions. Also, uncertainty due to the incomplete knowledge of the physics of the problem increases the model uncertainty, e.g. omitting potential solid phases in the chemical reactions. Numerical error due to incomplete iteration also affect the simulation results.

d. Experimental measurement error affect any experimentally determined parameter.

3. Structural damage due to cracking

   a. Inherent randomness in the input parameters that are observable/measureable quantities, e.g. Young's modulus and peak strength of the structure.

   b. Incomplete knowledge on some of the parameters contribute to data uncertainty, e.g. complete lack of knowledge on the fraction of porosity that needs to be filled before strain can develop due to the lack of experiments.

   c. Uncertainty associated with the empirical relations contribute to model uncertainty, e.g. Young's modulus and peak stress as in Eqs. (72) and (73), effect of cracking on diffusivity and Young's modulus. Various assumptions and approximation in the damage model, i.e. the realtion between the strain and the crack state of the structure, also add to the uncertainty in the model prediction.

d. Experimental measurement errors also add to the overall uncertainty of the model.

Some simplifying assumptions are made in the numerical simulation to keep the problem tractable. The statistical descriptions of the parameters are given in Table 6.3. The Young's modulus and the peak stress of the material are simulated as random variables having normal distributions with the mean as obtained from Eqs. (72) and (73), and standard deviation and COV specified as the variability (absolute value for the Young's modulus and % for the peak stress) in the values obtained from these equations. The porosity and tortuosity are expressed as normal distributions with mean and standard deviations obtained from the experiments given in the literature for a similar material. The initial concentrations of species are also expressed as normally distributed random variables with mean values obtained from the LeachXS database and an assumed 10% COV. The porosity, tortuosity and the total concentration of species are estimated from limited number of samples (assumed to be 5 in this section). Thus, the parameters of the distribution will have some uncertainty associated with them. Therefore, the mean and the variance of the distributions are assumed to have the student's t and the chi-square distributions respectively as described in Subsection 6.2.2 assuming that the underlying distributions for these parameters are normal. The external sulfate concentration is expressed as random variable having normal distribution with mean value as obtained from the literature and an assumed 10% COV. The fraction of porosity that needs to be filled for strain development is generally calibrated using experimental data. It is assumed to have normal distribution with 0.3 mean and 10% COV due to the lack of experimental observations. The uncertainty in the chemical equilibrium model parameters

as calibrated in Chapter V represents uncertainty in the model parameters as well as the model form error in the chemical equilibrium module. A preliminary stability analysis of the model using 100, 200 and 300 nodes showed that the most stable solution is obtained using 100 nodes. The instability in the solutions using 200 and 300 nodes may be the result of accumulation of machine error, incomplete iteration and discontinuity in the solution due to formation of cracks. Further investigation is needed to evaluate the cause of the instability. Therefore, the following simulations are performed using 100 nodes.

6.5.3 Design of numerical experiment

The statistical descriptions of the model and the input parameters are given in Table 6.3. The parameters are divided into two broad categories in order to isolate the effect of uncertainty in the chemical equilibrium model parameters from the uncertainty in the other input and model parameters of the model. The categories are – (T1) input parameters to the various parts of the model except the chemical equilibrium model parameters (i.e. the physical parameter uncertainty), and (T2) the model parameters in the chemical equilibrium module (i.e. the chemical parameter uncertainty). Effects of uncertainty in these two categories on the durability assessment of the cementitious structure are evaluated by considering three cases – (1) T1 probabilistic and T2 deterministic, (2) T1 deterministic and T2 probabilistic, and (3) both T1 and T2 probabilistic. 50 simulations are performed for each of the three cases using the single loop MCS as described in Section 6.3 and the damage progression rates as a function of time are obtained for each simulation. The damage progression rates are then

extrapolated to estimate the time required for the structure to crack completely under the exposure of sulfate solution as shown in Figure 6.6.

Table 6.3 : Statistical descriptions of the model and input parameters.

Parameter	Statistical Description
Porosity of concrete wall	$N(\mu_1, \sigma_1)$ $\frac{0.1-\mu_1}{(5\times10^{-3})/\sqrt{5}}$ ~Student's t with 4 degrees of freedom $\frac{4*(5\times10^{-3})^2}{\sigma_1^2}$ ~Chi-square with 4 degrees of freedom
Tortuosity of concrete wall	$N(\mu_2, \sigma_2)$ $\frac{430-\mu_2}{(64.5)/\sqrt{5}}$ ~Student's t with 4 degrees of freedom $\frac{4*(64.5)^2}{\sigma_2^2}$ ~Chi-square with 4 degrees of freedom
Initial Young's Modulus (MPa)	$N(37.5\times3, 4\times10^3)$
Ultimate Tensile Strength (MPa)	$N(5.1, 0.3*5.1)$
Fraction of available porosity	$N(0.3, 0.1*0.3)$
External sulfate concentration (moles/L)	$N(0.25, 0.1*0.25)$
Total concentrations of species (moles/kg)	$N(\mu_i, \sigma_i)$ $\frac{\bar{x}_i-\mu_i}{s_i/\sqrt{5}}$ ~Student's t with 4 degrees of freedom $\frac{4*(s_i)^2}{\sigma_i^2}$ ~Chi-square with 4 degrees of freedom $\bar{x}_i$: LeachXS database s_i : 0.1*$\bar{x}_i$
Equilibrium constants	As calibrated in Chapter V

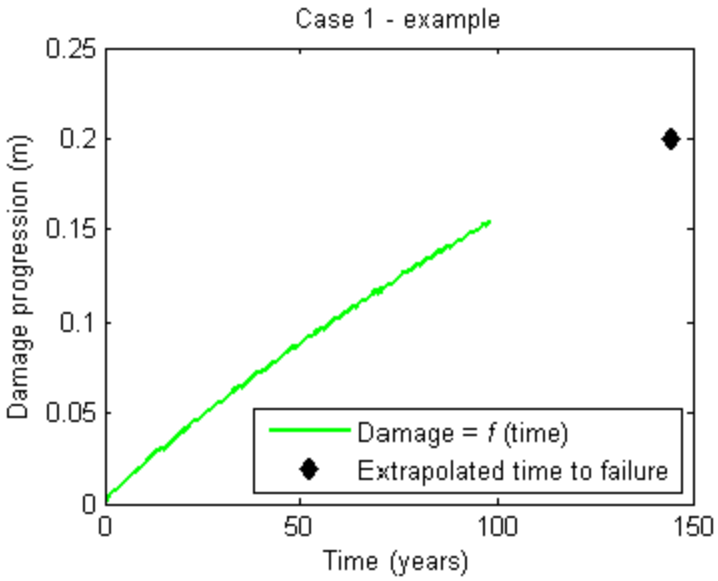

Figure 6.6 : Example of progression of damage.

The times required for complete cracking/damage are calculated from each of the 50 simulations for the three cases and are shown as diamond signs in Figure 6.7. Then, the probability densities and cumulative probabilities of complete cracking are estimated for the three cases as shown in Figures 6.8 and 6.9. The times to complete damage at selected percentile values for the three cases are given in Table 6.4. Cases 1 and 2 provide information on the effect of variability of input parameters and data uncertainty, and the effect of uncertainty in the model parameters of the chemical equilibrium model on the damage progression rate respectively. The probability of time to complete damage as evaluated from case 3 provides the complete information on the effect of both types of uncertainties on the damage progression of the structure. It is interesting to note that the total effect of cases 1 and 2 is not a linear combination of the individual effects and it reflects complex relationships among the various input and the model parameters. It is also important to note that the probability distribution of time to complete damage

becomes wider due to chemical parameter uncertainty in addition to physical parameter uncertainty. The service life assessment models [47-50] for the cementitious structure under chemical attack available in the literature mainly consider physical parameter uncertainty as mentioned in Chapter I. But it is evident from Figure 6.8 that the contribution of the chemical parameter uncertainty on the durability assessment is critically important and hence needs to be considered. However, it is also important to acknowledge that the numerical simulations performed in this section are for a saturated structure under constant boundary condition. This condition is more aggressive than that experienced in the field i.e. unsaturated structure under fluctuating boundary condition. Also, the results are based on only 50 Monte Carlo simulations for each case which do not represent an exhaustive set. Therefore the results obtained here should be considered as a conservative estimate.

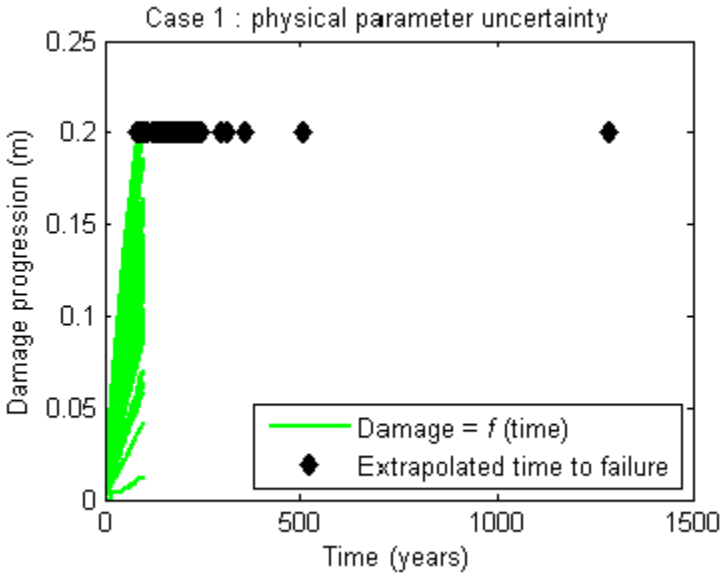

(a)

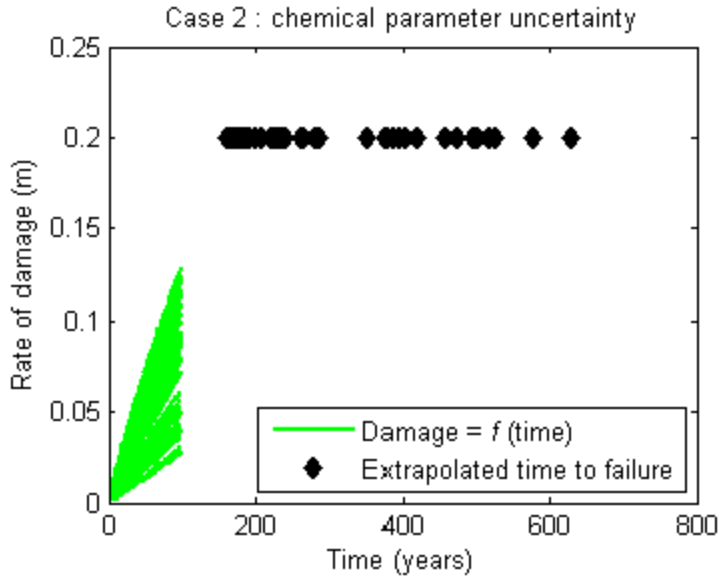

(b)

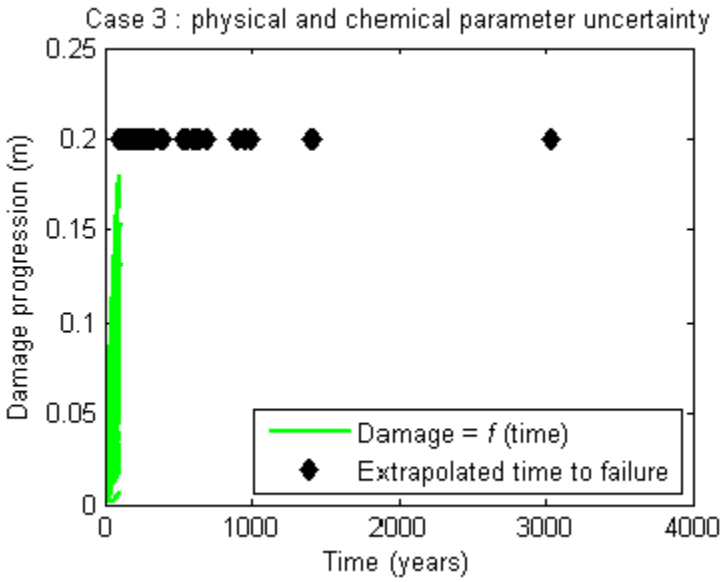

(c)

Figure 6.7 : Progression of damage and projected time to complete damage for the three cases.

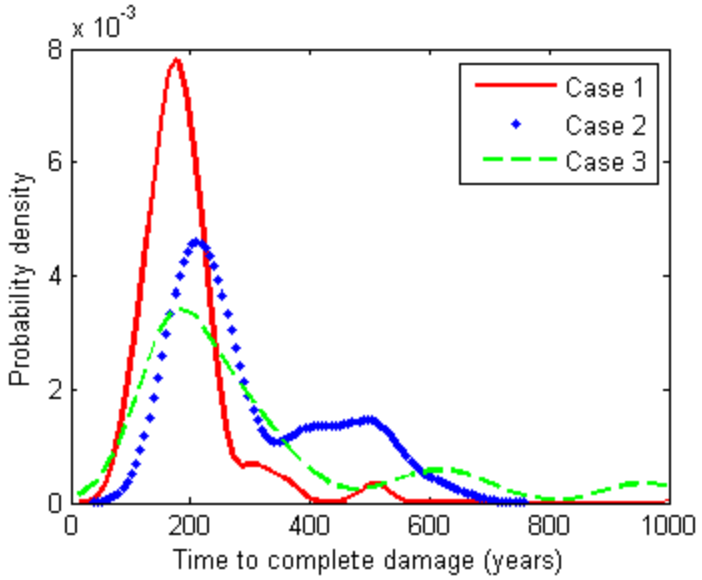

Figure 6.8 : Probability density of time to complete damage.

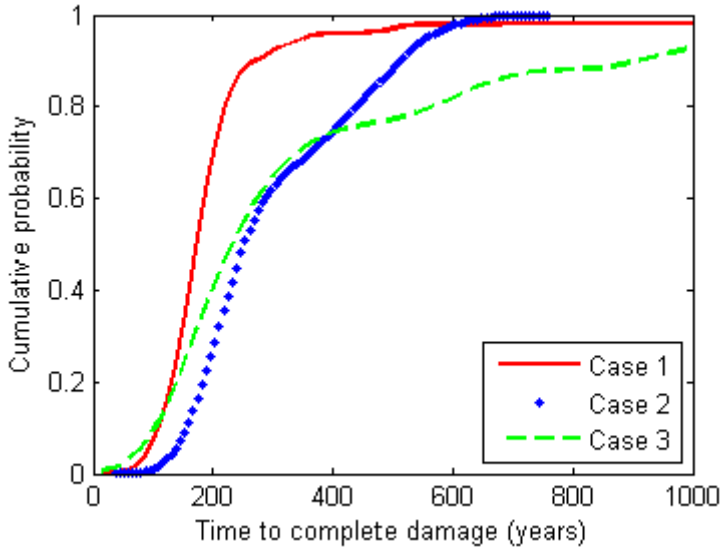

Figure 6.9 : Cumulative probability of time to complete damage.

Table 6.4 : Time (years) to complete damage at selected percentiles.

Cases / Percentiles	Case 1 Physical parameter uncertainty	Case 2 Chemical parameter uncertainty	Case 3 physical and chemical parameter uncertainty
5th	91	135	77
10th	108	156	103
25th	139	195	154
50th	173	254	233
75th	211	404	420
90th	272	511	913
95th	356	555	1364

6.6 Conclusion

A methodology is developed in this chapter for the durability assessment of the cementitious structure under external sulfate attack, by incorporating various sources of uncertainty. Different approaches are discussed for the quantification of uncertainty in the numerical model for – (1) inherent randomness in the parameters, (2) incomplete knowledge of the data, and (3) assumptions and approximations in the model. Different approaches for uncertainty propagation through a numerical model for uncertainty quantification in the model response using nested and single loop Monte Carlo simulation are discussed. The methodology for evaluating degradation of cementitious structures due to physical variability and data uncertainty in the input parameters is demonstrated.

Various sources of uncertainty in the numerical model developed in this dissertation are identified. The input and the model parameters are broadly classified into (1) input and model parameters in the various parts of the model except the chemical equilibrium module (i.e. the physical parameter uncertainty), and (2) the model parameters in the chemical equilibrium module (i.e. the chemical parameter uncertainty). The effects of

uncertainty in these two types of categories on the degradation of a concrete vault wall exposed to sulfate containing waste material (i.e. saltstone) are demonstrated by isolating and then combining these sources using Monte Carlo simulation. It is observed that the simulation results reflect nonlinear relationships among uncertain parameters. It is also evident from the simulation results that the contributions of both the physical and chemical parameter uncertainties are significant and need to be considered in the durability assessment of cementitious structures under chemical attack.

CHAPTER VII

SUMMARY AND FUTURE WORK

7.1 Summary

Cementitious materials in contact with sulfate containing water degrade with time due to the formation of expansive mineral phases leading to cracking and spalling of the structure. This has been identified as a potentially important degradation mechanism for underground containment structures containing solidified low activity nuclear waste material (e.g., saltstone). A numerical framework is developed in this dissertation for the durability assessment of such structures under exposure to sulfate rich environments.

The four essential components of the degradation mechanism incorporated in the numerical model in Chapters II and III are – (1) diffusion of ions in and out of the structure, (2) chemical reactions of the diffused species with the cement hydration products, (3) cracking due to expansive product formation, and (4) changes in the mechanical properties of the structure due to mineralogical changes as a result of chemical reactions. Diffusion of ions is assumed to occur under concentration as well as under chemical activity gradients. The diffused species react with the solid phases present in the cement matrix altering the mineralogical and pore structure features of the structure. The equilibrium solid phases are calculated using a geochemical speciation model assuming that the chemical reactions occur under local equilibrium. The expansive solid products formed as a result of chemical reactions deposit in the pores that may lead to cracking. A continuum damage mechanics approach is used in this research to evaluate

the crack state of the structure. The diffusion and mechanical properties are modified due to the presence of cracks and the changes in the parameters are incorporated in the framework using empirical relations. Finally, the effect of the mineralogical changes on the mechanical properties is estimated using a continuum micromechanics approach. The numerical model is calibrated and validated using experimental results available in the literature. Thus this improved mechanistic model can potentially be used to evaluate damage of the structure over time under external sulfate attack.

The numerical simulation of the degradation behavior of the structure varies with fluctuations in the external and internal factors. The changes in some of these factors affect the model response more than the others. A sensitivity analysis is performed in Chapter IV in order to identify the parameters that have significant influence on the model response. Additionally, the results of the sensitivity analysis can also be used for designing or maintenance scheduling of the structure.

An important aspect of numerical simulation of external sulfate attack is simulating chemical reactions and calculating the equilibrium solid phases that can potentially be present or form in the cementitious structure. Numerical simulation of chemical equilibrium requires thermodynamic information that is generally obtained from the literature. This information may not accurately represent the true behavior of the system due to imprecision in the experimental data, variability in the data across the literature, incomplete knowledge of the real system etc. A method is developed in Chapter V to quantify model parameter uncertainty in the chemical equilibrium module that did not receive significant attention in the literature. This methodology incorporates the

aforementioned uncertainties in the input parameters of the model and the experimental data obtained from a database/expert decision support system.

In Chapter VI, uncertainty quantification methods for incorporating – (1) physical variability, (2) data uncertainty, and (3) model uncertainty are discussed. Different approaches for propagating the uncertainties through a numerical model are also described. Application of the methods is demonstrated using nested and single loop Monte Carlo simulation techniques incorporating physical variability and data uncertainty. The input and model parameters for the particular model developed in this dissertation are broadly classified into two groups – (1) input and model parameters in the various parts of the model except the model parameters in the chemical equilibrium module (i.e. the physical parameter uncertainty), and (2) the model parameters in the chemical equilibrium module (i.e. the chemical parameter uncertainty). The effects of uncertainty in these two types of parameters on the progression of damage are evaluated separately and then collectively using single loop Monte Carlo simulation. It is observed that the contribution of the chemical parameter uncertainty on the durability of the structure is significant and should therefore be included along with physical parameter uncertainty for durability assessment of the structure.

In summary, a generalized approach for performance assessment of cementitious materials under aggressive chemical attack is developed and demonstrated in this dissertation. The numerical methodology includes coupled reactive transport, continuum damage mechanics and continuum micromechanics models for damage assessment of structures under external sulfate attack. This improved mechanistic model can be used to realistically simulate degradation of the structure exposed to aggressive sulfate rich

environment over time. Whenever long term simulation of structural response is of interest, it is important to incorporate various sources of uncertainty that can potentially affect the response of the structure. The probabilistic framework developed in this dissertation incorporates these sources of uncertainty and thus it can be used to assess long term durability of cementitious structures under chemical attack. It can also be applied to evaluate various designs for life extension of existing and future containment structure.

7.2 Future Work

The numerical methodology developed in this dissertation can be improved in many ways. Various aspects of the degradation of cementitious materials exposed to aggressive environment need to be investigated in detail. Some of these aspects are discussed in this subsection.

(1) Model scalability – In the current approach three dimensional problems are idealized as one dimensional. The model can be improved to include two and three dimensional problems so that corner effects (inability of a one dimensional model to evaluate singular regions such as corners) can be reduced, and different boundary conditions can be accommodated such as the concrete vault walls exposed to surrounding soils on five faces and the waste material on one face. Additionally, a three dimensional (or at least a two dimensional) model will be capable of manifesting the effects of porosity, tortuosity and cracking in different directions as is observed in a real structure. Also, concrete is heterogeneous material with nonreactive aggregates dispersed in a reactive cement

matrix. This aspect of the problem can also be realistically simulated as a three dimensional structure.

(2) Chemical equilibrium modeling – The chemical equilibrium model in its present form calculates the composition of the equilibrium solid phases based on the local equilibrium assumption whereas the kinetic effects of chemical reactions may prove to be significant if long term durability of the structure is desired. Therefore secondary effects such as kinetic aspects of chemical reactions need to be incorporated to improve the model prediction capability.

(3) Damage modeling – As mentioned in Chapter I, the mechanism of sulfate attack is not unanimously agreed upon. There are mainly two schools of thought – (1) paste expansion hypothesis and (2) crystal growth pressure hypothesis. The numerical model presented in this dissertation is mainly based on a simplified paste expansion hypothesis. Thus the smeared cracking approach on the macro structure was applied to assess cracking state of the structure. On the other hand, application of crystal growth pressure requires knowledge of shape, size and location of the deposited mineral. Thus a detailed two or three dimensional diffusion and chemical reaction simulation coupled with fracture mechanics based approach is needed to simulate cracking of the structure using the hypothesis. Comparison between the simulation and the experimental results may provide significant insight on the actual sulfate attack mechanism.

(4) Different sulfate salts – The behavior of the structure changes considerably depending on the cations associated with the sulfate ions (e.g., Na^{+}, Mg^{+2}, Ca^{+2} etc.)[156]. The main focus of researchers in this respect has been on sodium sulfate attack. Magnesium sulfate is generally considered to be the most detrimental among all sulfates [157-159].

But numerical simulation of magnesium sulfate attack is not investigated in the literature as the nature of the attack is complex and is not well understood [160]. A numerical simulation methodology needs to be developed for assessing the degradation of the structure under $MgSO_4$ attack, by including issues such as formation of "double layer" of brucite and gypsum [158, 159], and formation of magnesium silicate hydrate gels that do not have any adhesive properties [161, 162].

(5) Multiple degradation processes – A real structure is generally exposed to multiple processes that degrade the structure over time. For example, bridge piers, building foundations, pavement subgrades and underground structures are exposed to groundwater and seawater compositions (i.e. mixture of salts of Cl^-, SO_4^{-2} and CO_3^{-2}). In addition to chemical attack, these structures are also exposed to physical processes e.g. temperature fluctuation, infiltration and mechanical loads. Several studies have explored durability assessment of structures under coupled chemical, mechanical and physical processes [94, 163, 164]. The simulation methods for chemical reactions in these models are simplified and limited to few potential reactions. The numerical methodology developed in this dissertation can be integrated with the coupling approaches available in the literature to evaluate durability under realistic environmental conditions. In addition, experiments need to be conducted for assessing individual and interactive effects of various degradation mechanisms e.g. chemical, physical and mechanical. These experiments can be used for validation of the numerical framework.

(6) Controlled experiments – In this research, various input parameters of the model are assumed or obtained from the literature. Experimental determination of these parameters based on a statistically significant sample size can increase the confidence in the

durability prediction. Thus controlled experimental studies are needed to determine the statistical distributions of the input parameters of the model.

REFERENCES

1. Phifer, M.A., *Saltstone disposal facility mechanically stabilized earth vault closure cap degradation base case: institutional control to pine forest scenario (U)*. 2003, Washington Savannah River Company LLC, Savannah River Site.

2. Langton, C.A., *Analysis of saltstone pore solutions - PSU progress report IV*. 1987, E. I. du Pont de Nemours and Company: Aiken, South Carolina.

3. Clifton, J.R. and J.M. Pommersheim, *Sulfate attack of cementitious materials: volumetric relations and expansions*. 1994, Building and Fire Research Laboratory, National Institute of Standards and Technology: Gaithersburg, MD.

4. Naik, N.N., et al., *Sulfate attack monitored by microCT and EDXRD: Influence of cement type, water-to-cement ratio, and aggregate.* Cement and Concrete Research, 2006. **36**(1): p. 144-159.

5. Al-Dulaijan, S.U., *Sulfate resistance of plain and blended cements exposed to magnesium sulfate solutions.* Construction and Building Materials, 2007. **21**(8): p. 1792-1802.

6. Shazali, M.A., M.H. Baluch, and A.H. Al-Gadhib, *Predicting residual strength in unsaturated concrete exposed to sulfate attack.* Journal of Materials in Civil Engineering, 2006. **18**(3): p. 343-354.

7. Planel, D., et al., *Long-term performance of cement paste during combined calcium leaching-sulfate attack: kinetics and size effect.* Cement and Concrete Research, 2006. **36**(1): p. 137-143.

8. Wang, J.G., *Sulfate attack on hardened cement paste.* Cement and Concrete Research, 1994. **24**(4): p. 735-742.

9. Samson, E. and J. Marchand, *Modeling the transport of ions in unsaturated cement-based materials.* Computers & Structures, 2007. **85**(23-24): p. 1740-1756.

10. Tixier, R. and B. Mobasher, *Modeling of damage in cement-based materials subjected to external sulfate attack. I: formulation.* Journal of Materials in Civil Engineering, 2003. **15**(4): p. 305-313.

11. Krajcinovic, D., et al., *Chemo-micromechanics of brittle solids.* Journal of the Mechanics and Physics of Solids, 1992. **40**(5): p. 965-990.

12. Carde, C. and R. François, *Modelling the loss of strength and porosity increase due to the leaching of cement pastes.* Cement and Concrete Composites, 1999. **21**(3): p. 181-188.

13. Le Bellego, C., B. Gerard, and G. Pijaudier-Cabot, *Chemo-mechanical effects in mortar beams subjected to water hydrolysis.* Journal of Engineering Mechanics, 2000. **126**(3): p. 266-272.

14. Ulm, F.-J., J.M. Torrenti, and F. Adenot, *Chemoporoplasticity of calcium leaching in concrete.* Journal of Engineering Mechanics, 1999. **125**(10): p. 1200-1211.

15. Kuhl, D., F. Bangert, and G. Meschke, *Coupled chemo-mechanical deterioration of cementitious materials. Part I: Modeling.* International Journal of Solids and Structures, 2004. **41**(1): p. 15-40.

16. Bary, B., *Simplified coupled chemo-mechanical modeling of cement pastes behavior subjected to combined leaching and external sulfate attack.* International Journal for Numerical and Analytical Methods in Geomechanics, 2008. **32**(14): p. 1791-1816.

17. Gospodinov, P.N., R.F. Kazandjiev, and M.K. Mironova, *The effect of sulfate ion diffusion on the structure of cement stone.* Cement and Concrete Composites, 1996. **18**(6): p. 401-407.

18. Saetta, A., R. Scotta, and R. Vitaliani, *Mechanical behavior of concrete under physical-chemical attacks.* Journal of Engineering Mechanics, 1998. **124**(10): p. 1100-1109.

19. Schmidt-Dohl, F. and F.S. Rostasy, *A model for the calculation of combined chemical reactions and transport processes and its application to the corrosion of mineral-building materials Part I. simulation model.* Cement and Concrete Research, 1999. **29**(7): p. 1039-1045.

20. ASTM, *Standard test method for length change of hydraulic-cement mortars exposed to a sulfate solution*. 2004, ASTM International: West Conshohocken, PA.

21. Atkinson, A. and J.A. Hearne, *Mechanistic model for the durability of concrete barriers exposed to sulfate bearing groundwaters.* Scientific Basis for Nuclear Waste Management, 1989. **13**: p. 149-156.

22. Basista, M. and W. Weglewski, *Micromechanical modeling of sulphate corrosion in concrete: influence of ettringite forming reaction.* Theoretical and Applied Mechanics, 2008. **35**(1-3): p. 29-52.

23. Snyder, K.A. and J.R. Clifton, *4SIGHT manual: a computer program for modelling degradation of underground low level waste concrete vaults*. 1995, Building and Research Laboratory, National Institute of Standards and Technology: Gaithersburg, MD.

24. Brown, P.W. and H.F.W. Taylor, *The role of ettringite in external sulfate attack*,

in *Materials Science of Concrete: Sulfate Attack Mechanisms*, J. Marchand and J.P. Skalny, Editors. 1999, American Ceramic Society: Westerbrook, Ohio.

25. Meeussen, J.C.L., *ORCHESTRA: An object-oriented framework for implementing chemical equilibrium models.* Environmental Science and Technology, 2003. **37**(6): p. 1175-1182.

26. Mathworks, T., *Matlab: On-line documentation*. 2009: Natick, Massachusetts.

27. Ouyang, C., A. Nanni, and W.F. Chang, *Internal and external sources of sulfate ions in Portland cement mortar: two types of chemical attack.* Cement and Concrete Research, 1988. **18**(5): p. 699-709.

28. Ferraris, C.F., et al., *Mechanisms of degradation of Portland cement-based systems by sulfate attack*, in *Mechanisms of Chemical Degradation of Cement-based Systems*, K.L. Scrivener and J.F. Young, Editors. 1997, E & FN Spon: London. p. 185-192.

29. Lagerblad, B., *Long term test of concrete resistance against sulphate attack*, in *Materials Sceince of Concrete: Sulfate Attack Mechanisms*, J. Marchand and J.P. Skalny, Editors. 1999, American Ceramic Society: Westerbrook, Ohio. p. 325-336.

30. Brown, P.W., *An evaluation of the sulfate resistance of cements in a controlled environment.* Cement and Concrete Research, 1981. **11**: p. 719-727.

31. Cao, H.T., et al., *The effect of cement composition and pH of environment on sulfate resistance of Portland cements and blended cements.* Cement and Concrete Composites, 1997. **19**(2): p. 161-171.

32. Al-Dulaijan, S.U., et al., *Sulfate resistance of plain and blended cements exposed to varying concentrations of sodium sulfate.* Cement and Concrete Composites, 2003. **25**(4-5): p. 429-437.

33. Tixier, R. and B. Mobasher, *Modeling of damage in cement-based materials subjected to external sulfate attack. II: comparison with experiments.* Journal of Materials in Civil Engineering, 2003. **15**(4): p. 314-322.

34. Cabaniss, S.E., *Propagation of Uncertainty in Aqueous Equilibrium Calculations: Non-Gaussian Output Distributions.* Analytical Chemistry, 1997. **69**(18): p. 3658-3664.

35. Schulz, K., B. Huwe, and S. Peiffer, *Parameter uncertainty in chemical equilibrium calculations using fuzzy set theory.* Journal of Hydrology, 1999. **217**(1-2): p. 119-134.

36. Basista, M. and W. Weglewski, *Chemically assisted damage of concrete: a model of expansion under sulfate attack.* International Journal of Damage Mechanics,

2008.

37. Rigo, E., et al., *Transreac: a model for the calculation of combined chemical reactions and transport processes and its extension to a probabilistic model.* Cement and Concrete Research, 2005. **35**(9): p. 1734-1740.

38. Gawin, D., F. Pesavento, and B.A. Schrefler, *Modeling of cementitious materials exposed to isothermal calcium leaching, considering process kinetics and advective water flow. Part 1: Theoretical model.* International Journal of Solids and Structures, 2008. **45**: p. 6221-6240.

39. Nakarai, K., T. Ishida, and K. Maekawa, *Modeling of calcium leaching from cement hydrates coupled with micro-pore formation.* Journal of Advanced Concrete Technology, 2006. **4**(3): p. 395-407.

40. Delagrave, A., B. Gerard, and J. Marchand, *Modelling the calcium leaching mechanisms in hydrated cement pastes*, in *Mechanisms of Chemical Degradation of Cement-Based Systems; Proceedings of the Material Research Society's Symposium on Mechanisms of Chemical Degradation*. 1995.

41. Lothenbach, B., et al., *Thermodynamic modelling of the effect of temperature on the hydration and porosity of Portland cement.* Cement and Concrete Research, 2008. **38**(1): p. 1-18.

42. Lothenbach, B. and F. Winnefeld, *Thermodynamic modelling of the hydration of Portland cement.* Cement and Concrete Research, 2006. **36**(2): p. 209-226.

43. Bentz, D.P., *A three-dimensional cement hydration and microstructure development modeling package. Version 3.0*, in *NISTIR 7232*. 2005, National Institute of standards and Technology.

44. Bernard, O., F.-J. Ulm, and E. Lemarchand, *A multiscale micromechanics-hydration model for the early-age elastic properties of cement-based materials.* Cement and Concrete Research, 2003. **33**(9): p. 1293-1309.

45. Haecker, C.J., et al., *Modeling the linear elastic properties of Portland cement paste.* Cement and Concrete Research, 2005. **35**(10): p. 1948-1960.

46. Wilhite, E.L., *Performance assessment position paper: time for compliance*. 2003, Westinghouse Savannah River Company, Savannah River Site.

47. Mori, Y. and B.R. Ellingwood, *Reliability-base service-life assessment of aging concrete structures.* Journal of Structural Engineering, 1993. **119**(5): p. 1600-1621.

48. Oswald, G.F. and G.I. Schueller, *Reliability of deteriorating structures.* Engineering Fracture Mechanics, 1984. **20**(3): p. 479-488.

49. Gulikers, J., *Considerations on the reliability of service life predictions using probabilistic approach.* Journal de Physique IV, 2006. **136**: p. 233-241.

50. Choe, D.-E., et al., *Probabilistic capacity models and seismic fragility estimates for RC columns subject to corrosion.* Reliability Engineering & System Safety, 2008. **93**(3): p. 383-393.

51. Mindess, S. and J.F. Young, *Concrete*. Civil Engineering and Engineering Mechanics Series, ed. N.M. Newmark and W.J. Hall. 1981, New Jersey: Prentice Hall, Inc.

52. Kurtis, K.E., et al., *Mechanism of concrete damage caused by sulfate attack examined through transmission X-ray microscopy*, in *ALS Compendium of User Abstracts and Technical Reports*. 1998.

53. Diamond, S., *Delayed ettringite formation -- processes and problems.* Cement and Concrete Composites, 1996. **18**(3): p. 205-215.

54. Taylor, H.F.W., C. Famy, and K.L. Scrivener, *Delayed ettringite formation.* Cement and Concrete Research, 2001. **31**(5): p. 683-693.

55. Samson, E., et al., *Modelling ion diffusion mechanisms in porous media.* International Journal for Numerical Methods in Engineering, 1999. **46**(12): p. 2043-2060.

56. Marchand, J., et al., *Ion transport mechanisms in unsaturated porous media: modeling*, in *Encyclopedia of Surface and Colloid Science*, A.T. Hubbard, Editor. 2002, Marcel Dekker.

57. Samson, E., et al., *Modeling ion and fluid transport in unsaturated cement systems in isothermal conditions.* Cement and Concrete Research, 2005. **35**(1): p. 141-153.

58. Ping, X. and J.J. Beaudoin, *Mechanism of sulphate expansion I. thermodynamic principle of crystallization pressure.* Cement and Concrete Research, 1992. **22**(4): p. 631-640.

59. Marchand, J., et al. *Influence of calcium hydroxide dissolution on the transport properties of hydrated cement systems*. in *Materials Science of Concrete special volume: calcium hydroxide in concrete*. 2001.

60. Ruthven, D.M., *Principles fo adsorption and adsorption processes*. 1984: Wiley, John & Sons, Incorporated.

61. Shen, L. and Z. Chen, *Critical review of the impact of tortuosity on diffusion.* Chemical Engineering Science, 2007. **62**(14): p. 3748-3755.

62. Samson, E., et al., *Modeling chemical activity effects in strong ionic solutions.*

Computational Materials Science, 1999. **15**: p. 285-294.

63. Goñi, S. and C. Andrade, *Synthetic concrete pore solution chemistry and rebar corrosion rate in the presence of chlorides.* Cement and Concrete Research, 1990. **20**(4): p. 525-539.

64. Marchand, J., et al., *Theoretical analysis of the effect of weak sodium sulfate solutions on the durability of concrete.* Cement and Concrete Composites, 2002. **24**(3-4): p. 317-329.

65. Garrabrants, A.C., F. Sanchez, and D.S. Kosson, *Changes in constituent equilibrium leaching and pore water characteristics of a Portland cement mortar as a result of carbonation.* Waste Management, 2004. **24**(1): p. 19-36.

66. Gospodinov, P.N., et al., *Diffusion of sulfate ions into cement stone regarding simultaneous chemical reactions and resulting effects.* Cement and Concrete Research, 1999. **29**(10): p. 1591-1596.

67. van der Sloot, H.A., et al., *Evaluation of environmental aspects of alternative materials using an integrated approach assisted by a database/expert system*, in *Advances in Waste Management and Recycling*. 2003: Dundee, Scotland.

68. Chesworth, W., *Encyclopedia of soil science*. Encyclopedia of Earth Sciences. 2008: Springer.

69. Scherer, G.W., *Crystallization in pores.* Cement and Concrete Research, 1999. **29**(8): p. 1347-1358.

70. Denham, M., *Thermodynamic and mass balance analysis of expansive phase precipitation in saltstone*. 2008, Savannah River National Laboratory: Aiken, SC.

71. Karihaloo, B.L., *Fracture mechanics and structural concrete*. 1995, Essex, England: Longman Scientific and Technical.

72. Mazars, J., *A description of micro and macroscale damage of concrete structures.* Engineering Fracture Mechanics, 1986. **25**(5/6): p. 729-737.

73. Tao, X. and D.V. Phillips, *A simplified isotropic damage model for concrete under bi-axial stress states.* Cement and Concrete Composites, 2005. **27**(6): p. 716-726.

74. Labadi, Y. and N.E. Hannachi, *Numerical simulation of brittle damage in concrete specimens.* Strength of Materials, 2005. **37**(3): p. 268-281.

75. M. di Prisco, J.M., *Crush-crack': a non-local damage model for concrete.* Mechanics of Cohesive-frictional Materials, 1996. **1**(4): p. 321-347.

76. Scotta, R., et al., *A scalar damage model with a shear retention factor for the*

analysis of reinforced concrete structures: theory and validation. Computers & Structures, 2001. **79**(7): p. 737-755.

77. Budiansky, B. and R. O'Connell, *Elastic moduli of a cracked solid.* International Journal of Solids and Structures, 1976. **12**: p. 81-97.

78. Nemat-Nasser, S. and M. Hori, *Micromechanics: overall properties of heterogeneous materials*. 1993, New york: North-Holland.

79. Krajcinovic, D., *Effective material properties in the limit of large defect concentration.* Engineering Fracture Mechanics, 1997. **57**(2-3): p. 227-240.

80. Stauffer, D. and A. Aharony, *Introduction to percolation theory*. Revised second edition ed. 2003, Philadelphia, PA: Taylor & Francis Ltd.

81. Charlaix, E., *Percolation threshold of a random array of discs: a numerical simulation.* Journal of Physics A: Mathematical and General, 1986. **19**(9): p. L533-L536.

82. Sornette, D., *Critical transport and failure in continuum crack percolation.* Journal de Physique, 1988. **49**: p. 1365-1377.

83. Marchand, J., *Modeling the behavior of unsaturated cement systems exposed to aggressive chemical environments.* Materials and Structures, 2001. **34**(4): p. 195-200.

84. Meeussen, J.C.L. *How to include a solid solution in ORCHESTRA calculations*. 2009; http://www.meeussen.nl/orchestra/examples/solidsolution/.

85. Gerard, B., C.L. Bellego, and O. Bernard, *Simplified modelling of calcium leaching of concrete in various environments.* Materials and Structures, 2002. **35**(10): p. 632-640.

86. Smilauer, V. and Z. Bittnar, *Microstructure-based micromechanical prediction of elastic properties in hydrating cement paste.* Cement and Concrete Research, 2006. **36**(9): p. 1708-1718.

87. Yang, C.C. and R. Huang, *Double inclusion model for approximate elastic moduli of concrete material.* Cement and Concrete Research, 1996. **26**(1): p. 83-91.

88. Guillon, E., M. Moranville, and S. Kamali, *Characterization of the mechanical damage of a chemically degraded cement paste.* Materials and Structures/Materiaux et Constructions, 2006. **39**(288): p. 401-409.

89. Constantinides, G. and F.-J. Ulm, *The effect of two types of C-S-H on the elasticity of cement-based materials: Results from nanoindentation and micromechanical modeling.* Cement and Concrete Research, 2004. **34**(1): p. 67-80.

90. Al-Ostaz, A., et al., *A molecular dynamics and microporomechanics study on the mechanical properties of major constituents of hydrated cement*. 2008: http://www.serri.org/publications/Documents/Technical%20Papers/Ole%20Miss%20Project%2063888%20Pub%2025%20-%20Journal%20Article%20(10-6-2008).pdf.

91. Zaoui, A., *Continuum micromechanics: Survey.* Journal of Engineering Mechanics-Asce, 2002. **128**(8): p. 808-816.

92. Benveniste, Y., *A new approach to the application of Mori-Tanaka's theory in composite materials.* Mechanics of Materials, 1987. **6**(2): p. 147-157.

93. Adachi, T. and S. Sakka, *Dependence of the elastic moduli of porous silica gel prepared by the sol-gel method on heat-treatment.* Journal of Materials Science, 1990. **25**: p. 4732-4737.

94. Saetta, A., R. Scotta, and V. Renato, *Coupled environmental-mechanical damage model of RC structures.* Journal of Engineering Mechanics, 1999. **125**(8): p. 930-940.

95. Gerard, B., G. Pijaudier-Cabot, and C. Laborderie, *Coupled diffusion-damage modelling and the implications on failure due to strain localisation.* International Journal of Solids and Structures, 1998. **35**(31-32): p. 4107-4120.

96. Ababneh, A., F. Benboudjema, and Y. Xi, *Chloride penetration in nonsaturated concrete.* Journal of Materials in Civil Engineering, 2003. **15**(2): p. 183-191.

97. Martín-Pérez, B., S.J. Pantazopoulou, and M.D.A. Thomas, *Numerical solution of mass transport equations in concrete structures.* Computers & Structures, 2001. **79**(13): p. 1251-1264.

98. Ferretti, D. and Z.P. Bazant, *Stability of ancient masonry towers: Moisture diffusion, carbonation and size effect.* Cement and Concrete Research, 2006. **36**(7): p. 1379-1388.

99. Steffens, A., D. Dinkier, and H. Ahrens, *Modeling carbonation for corrosion risk prediction of concrete structures.* Cement and Concrete Research, 2002. **32**(6): p. 935-941.

100. Chen, D. and S. Mahadevan, *Chloride-induced reinforcement corrosion and concrete cracking simulation.* Cement and Concrete Composites, 2008. **30**(3): p. 227-238.

101. Nguyen, V.H., et al., *Chemo-mechanical coupling behaviour of leached concrete: Part I: Experimental results.* Nuclear Engineering and Design, 2007. **237**(20-21): p. 2083-2089.

102. Carde, C. and R. Franois, *Effect of ITZ leaching on durability of cement-based*

materials. Cement and Concrete Research, 1997. **27**(7): p. 971-978.

103. Aköz, F., et al., *Effects of sodium sulfate concentration on the sulfate resistance of mortars with and without silica fume.* Cement and Concrete Research, 1995. **25**(6): p. 1360-1368.

104. van der Sloot, H.A., *Characterization of the leaching behaviour of concrete mortars and of cement-stabilized wastes with different waste loading for long term environmental assessment.* Waste Management, 2002. **22**(2): p. 181-186.

105. Westall, J.C., J.L. Zachara, and F.M.M. Morel, *MINEQL, a computer program for the calculation of the chemical equilibrium composition of aqueous systems*. 1972, Department of Civil Engineering, Massachusetts Institute of Technology.

106. Allison, J.D., D.S. Brown, and K.J. Novo-gradac, *MINTEQA2, geochemical assessment model for environmental systems, version 3.* 1992, U.S. Environmental Protection Agency: Washington, DC.

107. Parkhurst, D.L. and C.A.J. Appelo, *User's guide to PHREEQC (version 2), a computer program for speciation, batch-reaction, one-dimensional transport, and inverse geochemical calculations*. 2002, U.S. Geological Survey.

108. *The geochemist's workbench version 4.0*. www.rockware.com/.

109. Keizer, M.G. and W.H. Van Riemsdijk, *ECOSAT, a computer program for the calculation of chemical speciation and transport in soil-water systems*. 1995, Wageningen Agricultural University.

110. Haldar, A. and S. Mahadevan, *Probability, Reliability, and Statistical Methods in Engineering Design*. 2000: John Wiley and Sons.

111. Walsh, B. *Markov Chain Monte Carlo and Gibbs sampling*. 2002.

112. Metropolis, N., et al., *Equation of State Calculations by Fast Computing Machines.* The Journal of Chemical Physics, 1953. **21**(6): p. 1087-1092.

113. Hastings, W.K., *Monte Carlo Sampling Methods Using Markov Chains and Their Applications.* Biometrika, 1970. **57**(1): p. 97-109.

114. Geman, S. and D. Geman, *Stochastic relaxation, Gibbs distributions, and Bayesian restoration of images.* IEEE Transactions on Pattern Analysis and Machine Intelligence, 1984. **PAMI-6**(6): p. 721-41.

115. Haario, H., E. Saksman, and J. Tamminen, *An adaptive Metropolis algorithm.* Bernoulli, 2001. **7**(2): p. 223-242.

116. Mira, A., *On Metropolis-Hastings algorithms with delayed rejection.* Metron, 2001. **LIX**(3-4): p. 231-241.

117. Haario, H., E. Saksman, and J. Tamminen, *Adaptive proposal distribution for random walk Metropolis algorithm.* Computational Statistics, 1999. **14**(3): p. 375-395.

118. Gilks, W.R., G.O. Roberts, and E.I. George, *Adaptive Direction Sampling.* Journal of the Royal Statistical Society. Series D (The Statistician), 1994. **43**(1): p. 179-189.

119. Atchade, Y.F. and J.S. Rosenthal, *On adaptive Markov chain Monte Carlo algorithms.* Bernoulli, 2005. **11**(5): p. 815-828.

120. Tierney, L. and A. Mira, *Some adaptive Monte Carlo methods for Bayesian inference.* Statistics in Medicine, 1999. **18**: p. 2507-2515.

121. Haario, H., et al., *DRAM: Efficient adaptive MCMC.* Statistics and Computing, 2006. **16**(4): p. 339-354.

122. Gelman, A., G.O. Roberts, and W.R. Gilks, *Efficient Metropolis jumping rules.* Bayesian Statistics, 1996. **5**: p. 599-607.

123. SIMCO Technologies, I., *Evaluation of sulfate attack on saltstone vault concrete and saltstone*, C.A. Langton, Editor. 2008, Savannah River National Laboratory: Aiken.

124. Dixon, K., J. Harbour, and M.A. Phifer, *Hydraulic and physical properties of saltstone grouts and vault concretes*. 2008.

125. Geisser, S., *Predictive inference: an introduction*. Monographs on Statistics and Applied Probability 55. 1993, New York: Chapman & Hall.

126. Stewart, M.G. and J.A. Mullard, *Spatial time-dependent reliability analysis of corrosion damage and the timing of first repair for RC structures.* Engineering Structures, 2007. **29**(7): p. 1457-1464.

127. Rebba, R., S. Mahadevan, and S. Huang, *Validation and error estimation of computational models.* Reliability Engineering & System Safety, 2006. **91**(10-11): p. 1390-1397.

128. Gurley, K.R., *Modeling and simulation of non-Gaussian processes*. 1997, University of Notre Dame.

129. Ghanem, R.G. and P.D. Spanos, *Stochastic finite elements: a sepctral approach*. 2003: Dover Publications.

130. Huang, S.P., S. Mahadevan, and R. Rebba, *Collocation-based stochastic finite element analysis for random field problems.* Probabilistic Engineering Mechanics, 2007. **22**: p. 194-205.

131. Mathelin, L., M.Y. Hussaini, and T.A. Zang, *Stochastic approaches to uncertainty quantification in CFD simulations* Numerical Algorithms, 2005. **38**(1-3): p. 209-236.

132. Red-Horse, J.R. and A.S. Benjamin, *A probabilistic approach to uncertainty quantification with limited information.* Reliability Engineering & System Safety, 2004. **85**: p. 183-190.

133. Box, G.E.P., G.M. Jenkins, and G.C. Reinsel, *Time series analysis forecasting and control*. 3rd ed. 1994, Englewood Cliffs, New Jersey: Prentice Hall.

134. Nigam, N.C., *Introduction to random vibrations*. 1983: MIT Press.

135. Marhadi, K.S., S. Venkararaman, and S. Pai. *Quantifying uncertainty in statistical distribution of small sample data using Bayesian inference of unbounded Johnson distribution*. in *49th AIAA/ ASME/ ASCE/ AHS/ ASC Structures, Structural Dynamics and Material Conference*. 2008. Schaumburg, IL.

136. Wang, F.K., *Confidence interval for the mean of non-normal data.* Quality and Reliability Engineering International, 2001. **17**(4): p. 257-267.

137. Bonett, D.G., *Approximate confidence interval for standard deviation of nonnormal distributions.* Computational Statistics & Data Analysis, 2006. **50**(3): p. 775-782.

138. McDonald, M., K. Zaman, and S. Mahadevan. *Uncertainty quantification and propagation for multidisciplinary system analysis*. in *12th AIAA/ ISSMO Multidisciplinary Analysis and Optimization Conference*. 2008. Victoria, British Columbia, Canada.

139. Rebba, R. and S. Mahadevan, *Model predictive capability assessemtn under uncertainty.* AIAA Journal, 2006. **44**(10): p. 2376-2384.

140. Rebba, R. and S. Mahadevan, *Computational methods for model reliability assessment.* Reliability Engineering & System Safety, 2008. **93**: p. 1197-1207.

141. Coleman, H.W. and F. Stern, *Uncertainties and CFD code validation.* Journal of Fluid Engineering, 1997. **119**: p. 795-803.

142. Jr., M.V. and E.L. Gaertner, *Finite element simulation and error estimation of polymer melt flow.* Revista Materia, 2004. **9**(4): p. 453-464.

143. Jr., M.V. and E.L. Gaertner, *Finite element and finite volume simulation and error assessment of polymer melt flow in closed channels.* Communications in Numerical Methods in Engineering, 2006. **22**(11): p. 1077-1085.

144. Roy, C.J., *Grid convergence error analysis for mixed-order numerical schemes.* AIAA Journal, 2003. **41**(4): p. 595-604.

145. Roache, P.J., *Quantification of uncertainty in computational fluid dynamics.* Annual Review of Fluid Mechanics, 1997. **29**: p. 126-160.

146. Franke, J. and W. Frank, *Application of generalized Richardson extrapolation to the computation of the flow across an asymmetric street intersection.* Journal of Wind Engineering and Industrial Aerodynamics. **96**(10-11): p. 1616-1628.

147. Embree, M. *Lecture 24: Richardson extrapolation and Romberg integration*. CAAM 453 . Numerical Analysis I October, 2009.

148. Enright, M.P. and D.M. Frangopol, *Service-life prediction of deteriorating concrete bridges.* Journal of Structural Engineering, 1998. **124**(3): p. 309-317.

149. Kong, J.S., et al., *Reliability analysis of chloride penetration in saturated concrete.* Probabilistic Engineering Mechanics, 2002. **17**(3): p. 305-315.

150. Sudret, B., G. Defaux, and M. Pendola, *Time-variant finite element reliability analysis - application to the durability of cooling towers.* Structural Safety, 2005. **27**(2): p. 93-112.

151. McFarland, J., et al., *Calibration and uncertaintry analysis for computer simulations with multivariate output.* AIAA Journal, 2008. **46**(5): p. 1253-1265.

152. McFarland, J.M., *Uncertainty analysis for computer simulations through validation and calibration*, in *Mechanical Engineering*. 2008, Vanderbilt University: Nashville.

153. Tixier, R. *Sulfate2*. http://ciks.cbt.nist.gov/~bentz/phpct/cmml.html.

154. *Engineering and design, Seismic Design provisions for roller compacted concrete dams*, U.S.A.C.o.E. Department of the Army, Editor. 1995.

155. Raphael, J.M., *Tensile strength of concrete.* ACI Journal, 1984. **81**(2): p. 158-165.

156. Torii, K. and M. Kawamura, *Effects of fly ash and silica fume on the resistance of mortar to sulfuric acid and sulfate attack.* Cement and Concrete Research, 1994. **24**(2): p. 361-370.

157. Turker, F., et al., *Effects of magnesium sulfate concentration on the sulfate resistance of mortars with and without silica fume.* Cement and Concrete Research, 1997. **27**(2): p. 205-214.

158. Bonen, D. and M.D. Cohen, *Magnesium sulfate attack on portland cement paste-I. Microstructural analysis.* Cement and Concrete Research, 1992. **22**(1): p. 169-180.

159. Bonen, D., *A microstructural study of the effect produced by magnesium sulfate on plain and silica fume-bearing Portland cement mortars.* Cement and Concrete

Research, 1993. **23**(3): p. 541-553.

160. Lee, S.-T., *Performance deterioration of Portland cement matrix due to magnesium sulfate attack.* KSCE Journal of Civil Engineering, 2007. **11**(3): p. 157-163.

161. Collepardi, M., *A state-of-the-art review on delayed ettringite attack on concrete.* Cement and Concrete Composites, 2003. **25**(4-5): p. 401-407.

162. Amin, M.M., et al., *Effects of magnesium sulfate attack on ordinary Portland cement (OPC) mortars* Portugaliae Electrochimica Acta, 2008. **26**: p. 235-242.

163. Cervera, M., J. Oliver, and T. Prato, *Thermo-chemo-mechanical model for concrete. II: Damage and creep.* Journal of Engineering Mechanics, 1999. **125**(9): p. 1028-1039.

164. Chen, D., *Computational framework for durability assessment of reinforced concrete structures under coupled deterioration processes*, in *Civil Engineering*. 2006, Vanderbilt University: Nashville. p. 252.

APPENDIX

NUMERICAL SIMULATION PARAMETERS

Chapter II

Subsection 2.4.1

Input parameters	Geometry : 7 cm diameter, 20 mm thickness Porosity : 0.52 Sulfate concentration (mmol/L) : 50 Renewal rate (days) : 7 External solution pH : 10.3 Tank volume (L) : 30
Calibration parameters	b : 0.3 Tortuosity : 35

Subsection 2.4.2

Input parameters	Geometry : 25 mm x 25 mm x 285 mm Porosity : 0.3 Tortuosity : 36 b : 0.2 Sulfate concentration (mmol/L) : 350 Renewal rate (days) : 7 External solution pH : 7 Tank volume (L) : 1.78

Chapter III

Subsection 3.3.1

Input parameters	Geometry : 110 mm diameter, 220 mm height Ammonium nitrate concentration (mol/L) : 6 Boundary condition : fixed External solution pH : 8
Calibration parameters	Porosity : 0.15 Tortuosity : 120

Subsection 3.3.2

Input parameters	Geometry : 40 mm x 40 mm x 160 mm Sulfate concentrations (mg/L) : 2700, 18000, 72000 Renewal rate (days) : 14 External solution pH : 7 Tank volume (L) : 2.56
Calibration parameters	Porosity : 0.25 Tortuosity : 50 b : 0.55

Chapter IV

Subsection 4.2.1

Input parameters	Cement type : I Geometry : 50 mm x 50 mm x 50 mm Sulfate concentrations (mmol/L) : 350 Renewal rate (days) : 7 External solution pH : 3, 5, 7, 9, 12 Tank volume (L) : 30 Porosity : 0.25 Tortuosity : 100 b : 0.5

Subsection 4.2.2

Input parameters	Cement type : I Geometry : 50 mm x 50 mm x 50 mm Sulfate concentrations (mmol/L) : 150, 250, 350, 450, 550 Renewal rate (days) : 7 External solution pH : 7 Tank volume (L) : 30 Porosity : 0.25 Tortuosity : 100 b : 0.5

Subsection 4.2.3

Input parameters	Cement type : I Geometry : 50 mm x 50 mm x 50 mm Sulfate concentrations (mmol/L) : 350 Renewal rate (days) : 1, 7, 14, 30, 180, 720 External solution pH : 7 Tank volume (L) : 30 Porosity : 0.25 Tortuosity : 100 b : 0.5

Subsection 4.2.4

Input parameters	Cement type : I Geometry : 50 mm x 50 mm x 50 mm Sulfate concentrations (mmol/L) : 350 Renewal rate (days) : 7 External solution pH : 7 Tank volume (L) : 30 Porosity : 0.15, 0.2, 0.25, 0.3, 0.35 Tortuosity : 100 b : 0.5

Subsection 4.2.5

Input parameters	Cement type : I Geometry : 50 mm x 50 mm x 50 mm Sulfate concentrations (mmol/L) : 350 Renewal rate (days) : 7 External solution pH : 7 Tank volume (L) : 30 Porosity : 0.25 Tortuosity : 100 b : 0.3, 0.4, 0.5, 0.6, 0.7

Subsection 4.2.6

Input parameters	Cement type : I Geometry : 50 mm x 50 mm x 50 mm Sulfate concentrations (mmol/L) : 350 Renewal rate (days) : 7 External solution pH : 7 Tank volume (L) : 30 Porosity : 0.25 Tortuosity : 60, 80, 100, 120, 140 b : 0.5

Subsection 4.2.7

Input parameters	Cement type : I and V Geometry : 50 mm x 50 mm x 50 mm Sulfate concentrations (mmol/L) : 350 Renewal rate (days) : 7 External solution pH : 7 Tank volume (L) : 30 Porosity : 0.25 Tortuosity : 100 b : 0.5

Chapter V

Subsection 5.4.1

Input parameters	Cement type : CEM V/A 32.5 N
Calibration parameters	Equilibrium constants

Subsection 5.4.2

Input parameters	Cement type : V (ASTM C150)
Calibration parameters	Equilibrium constants

Chapter VI

Section 6.4

Input parameters	Cement type : I Geometry : 25 mm x 25 mm x 285 mm Distribution of parameters : see Table 6.1

Section 6.5

Input parameters	Cement type : V Geometry : 200 mm Distribution of parameters : see Table 6.3